

FORMATION OF TAYLOR VORTICES
IN SPHERICAL COUETTE FLOW

by

Laurette Stephanie Tuckerman
A.B. Princeton University (1976)

Submitted to the Department of Mathematics
in Partial Fulfillment of the
Requirements for the Degree of

DOCTOR OF PHILOSOPHY

at the

Massachusetts Institute of Technology

November 1983 Feb 84

© Laurette Tuckerman 1983

The author hereby grants to M.I.T. permission to reproduce and to
distribute copies of this thesis document in whole or in part.

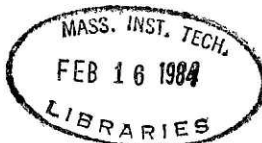
Signature of Author: Signature redacted
Department of Mathematics, November 23, 1983

Certified by: Signature redacted
Thesis Supervisor

Certified by: Signature redacted
Chairman, Applied Mathematics Committee

Accepted by: Signature redacted
Chairman, Department Committee

Archives



FORMATION OF TAYLOR VORTICES
IN SPHERICAL COUETTE FLOW

by

Laurette Stephanie Tuckerman

Submitted to the Department of Mathematics
on November 23, 1983 in partial fulfillment of the
requirements for the degree of
Doctor of Philosophy

ABSTRACT

Spherical Couette flow for the gap size $\sigma = 0.18$ is studied using a numerical axisymmetric initial value code. Transitions between states with zero, one, or two Taylor vortices per hemisphere are simulated numerically. It is found that transitions to the one-vortex state occur asymmetrically with respect to the equator, despite the symmetry of the initial and final states. We show that a small interval of the primary branch, consisting of zero- and two-vortex states, is linearly unstable to an antisymmetric perturbation. The instability initiates transition to the secondary branch containing the one-vortex states. Eigenvalues and eigenvectors of the perturbation are computed. Torques of steady states and critical Reynolds numbers for transition are compared with experiment.

Thesis Supervisor: Philip S. Marcus

Title: Associate Professor,
Department of Astronomy and Division of Applied Sciences,
Harvard University

ACKNOWLEDGEMENTS

I would like to thank my thesis advisor Philip Marcus, for acquainting me with Taylor-Couette flow and numerical methods, for suggesting this problem whose solution turned out to be so surprisingly (to me, anyway) beautiful, and finally for all of his time-consuming but valuable suggestions concerning the thesis itself.

I would also like to thank many friends and colleagues, but particularly Bruce Bayly, Marc Brachet, Richard Friesner, and Daniel Meiron for their contributions of all sorts.

I thank Profesor Steven Orszag for the use of the computational laboratory, where I have profited from both the computer facilities and the fellowship therein. I also thank Professor Alar Toomre for appreciating my efforts and results.

I thank Dr. Geza Schrauf and Dr. Manfred Wimmer for communicating their results to me.

I acknowledge the financial support of an National Science Foundation Graduate Fellowship and of Teaching Assistantships from the MIT Committee on Applied Mathematics. This work was supported in part by NSF Grants MEA-82-15695 and AST-82-10933. The numerical calculations were performed on the CRAY-1 at the National Center for Atmospheric Research (operated by the National Science Foundation).

Dedicated to the memory of

Stephen Pancitz

TABLE OF CONTENTS

PART I

1. Introduction.....7

- 1.1 Spherical Couette flow
- 1.2 Organization of the thesis

Figure

2. Historical Survey.....15

- 2.1 Discovery of Taylor vortices in spheres
- 2.2 Experimental results for $\sigma = 0.18$
- 2.3 Further stability analyses
- 2.4 Wide and narrow gap instability;
results for $\sigma = 0.11$
- 2.5 Numerical results for $\sigma = 0.17647$

3. Numerical Methods.....29

- 3.1 Equations of motion
- 3.2 Spatial approximation
- 3.3 Temporal approximation
- 3.4 Solution of elliptic equations
- 3.5 Eigenvectors and eigenvalues;
unstable equilibria

4. Tests.....45

- 4.1 Transitions and limits of stability
- 4.2 Torques
- 4.3 Sizes of vortices
- 4.4 Internal tests

Figures and Tables

PART II: DESCRIPTIVE RESULTS

5. Description of Flows.....58

- 5.1 Basic flow
- 5.2 Pinches
- 5.3 Taylor vortices

Figures

6. Transitions.....73

- 6.1 Zero- to one- vortex
- 6.2 Zero- to two- vortex
- 6.3 One- to zero- vortex
- 6.4 Two- to one- vortex

Figures

PART III: ANALYSIS OF RESULTS

7. Steady States.....93

- 7.1 Bifurcation diagram for spheres
- 7.2 Branches and turning points
- 7.3 Relation to cylinders

Figures

8. Linear Instability.....104

- 8.1 Growth rates and the window
- 8.2 Relation to previous numerical work
- 8.3 Eigenvectors

Figures

9. Energy Transfer.....121

- 9.1 Symmetric and antisymmetric energy
- 9.2 Energy transfer from a purely azimuthal equilibrium

Figures

10. Conclusion.....129

REFERENCES.....135

PART I

1. INTRODUCTION

The subject of this thesis is an axisymmetric numerical study of Taylor vortices in spherical Couette flow. Spherical Couette flow, defined to be the incompressible flow between differentially rotating concentric spheres, encompasses a rich variety of phenomena as the parameter values are varied. The configuration with inner and outer radii R_1 and R_2 , and angular velocities Ω_1 and Ω_2 is shown in Figure 1.1. R_1 and R_2 can be combined into the non-dimensional gap width

$$\sigma \equiv \frac{(R_2 - R_1)}{R_1} \quad (1.1)$$

which completely specifies the geometry.

When the gap width σ is small, the flow near the equator is a variation of cylindrical Taylor-Couette flow, the classic hydrodynamic problem of flow between two differentially rotating cylinders (Taylor 1923). We specialize further to the case in which the outer cylinder or sphere is at rest, i.e. $\Omega_2 = 0$. The Reynolds number is defined by

$$Re \equiv \frac{R_1^2 \Omega_1}{\nu} \quad (1.2)$$

where ν is the kinematic viscosity. Re and σ supply a complete set of non-dimensional parameters.

The flow is required to satisfy the Navier-Stokes equations

$$\frac{\partial \mathbf{u}}{\partial t} + (\mathbf{u} \cdot \nabla) \mathbf{u} = -\nabla P + \frac{1}{\text{Re}} \nabla^2 \mathbf{u} \quad (1.3)$$

the equation of incompressibility

$$\nabla \cdot \mathbf{u} = 0 \quad (1.4)$$

and the two-point no-slip boundary conditions

$$\mathbf{u}(R_1, \theta) = \Omega_1 R_1 \sin \theta \mathbf{e}_\phi \quad \mathbf{u}(R_2, \theta) = 0 \quad (1.5)$$

The ϕ component of the flow is called azimuthal while the flow perpendicular to \mathbf{e}_ϕ

$$\mathbf{u}_m \equiv \mathbf{u} - u_\phi \mathbf{e}_\phi = u_r \mathbf{e}_r + u_\theta \mathbf{e}_\theta \quad (1.6)$$

is called meridional.

1.1 Spherical and cylindrical Couette flow

The solution to (1.3-1.5) obtained by removing the time dependence and setting Re to zero, thereby eliminating nonlinear terms, is called Stokes flow. The Stokes solution is exclusively azimuthal. Each radial shell moves with a constant angular velocity which varies smoothly from that of the inner radius to zero at the outer radius.

In cylindrical Couette flow (with infinite aspect ratio), due to fortuitious cancellation pressure gradient with the nonlinear terms, the Stokes solution happens also to be a solution to the full nonlinear Navier-Stokes equations (1.3). Apart from scaling, the laminar flow changes with increasing Re only when it becomes unstable. It is not

surprising that cancellation of the nonlinear terms and pressure gradient does not occur in spherical Couette flow. A small meridional velocity is generated by the Stokes solution since the governing equation of the meridional velocity contains nonlinear terms in the azimuthal velocity. The small meridional velocity in turn influences the azimuthal velocity. Spherical Couette flow deviates from the Stokes solution for any finite Reynolds number. The resulting intractability of spherical Couette flow favors cylindrical Couette flow for analytic study, despite the widespread occurrence of spherical geometries in geophysical and astrophysical applications.

Although no closed form solution for spherical Couette flow has been found, a qualitative description for the basic (low Reynolds number) flow can be given. The largest component of the velocity is still azimuthal, and does not depart greatly from Stokes flow. The meridional motion is driven by Ekman pumping, which expels fluid out from the poles along the surface of the rotating inner sphere. The streamlines resulting from the superposition of the azimuthal and the weaker meridional motion are spirals. Despite being three-dimensional, the flow is axisymmetric (i.e., axisymmetric with swirl).

In cylindrical Couette flow, the basic flow (the Stokes flow, in this case) becomes unstable to Taylor vortices when the angular momentum gradient, as measured by the Reynolds

number, reaches a critical level (Rayleigh 1916). Taylor vortices redistribute the angular momentum among cylindrical shells. Taylor vortex flow remains axisymmetric until a higher Reynolds number is attained.

In spherical Couette flow, Taylor vortices also form when Re exceeds a critical value, but only in the equatorial region and only for $\sigma < 0.24$ (Belyaev 1978). The medium gap size $\sigma = 0.18$ which we use was first selected for experimental study by Sawatzki and Zierrep (1970) and Wimmer (1976). Bonnet and Alziary de Roquefort (1976), Bartels (1982), and Schrauf (1983) numerically investigated the almost identical gap size $\sigma = .17647$.

Wimmer, Sawatzki, and Zierrep found three different axisymmetric steady states at $Re \gtrsim 600$, each with a different number of Taylor vortices (zero, one, or two) per hemisphere. The equilibrium attained by the flow depends on its history, in particular on the acceleration of the inner sphere to its final angular velocity. Non-uniqueness in the number of vortices has also been observed experimentally in cylindrical Couette flow (Coles 1965, Snyder 1969, Burkhalter and Koschmieder 1974), especially in short cylinders (Benjamin 1978b). However, the classical mathematical model (Kirchgassner and Sorger 1968, Kogelman and DiPrima 1970) for cylindrical Couette flow assumes cylinders of infinite length and the number of vortices is imposed as one of the parameters.

Initial-value codes for spherical Couette flow have been written by Bonnet and Alziary de Roquefort, and Bartels which are axisymmetric and reflection symmetric about the equator. They have reproduced some of the final states observed by Wimmer, and have observed non-uniqueness caused by acceleration rate, but have failed to generate what is called the one-vortex state as a transition from the basic flow.

Two questions emerge from these previous studies:

1) Why has generation of the one-vortex state eluded other initial-value studies?

2) What is the mechanism by which the history of the flow determines the final steady state?

The thesis answers these questions.

1.2 Organization of thesis

Part I continues the introduction to the problem and describes our numerical simulation. Chapter 2 is a survey of the literature of Taylor vortices in spherical Couette flow. In chapter 3, we describe the numerical methods used in our time-dependent, axisymmetric code. We emphasize that our program differs from previous simulations, in that it does not impose equatorial symmetry and uses spectral methods rather than finite differences. In chapter 4, we show that our program is not only internally consistent, but also gives results which agree well with previous investigations, particularly the experimental measurements of Wimmer.

In Part II, we present our numerically computed flows. Detailed descriptions of the steady flow states for $\sigma = 0.18$ -- with zero, one, and two Taylor vortices -- are in Chapter 5. In Chapter 6 the time evolution of the transitions among the different steady flow states are given. The transitions have not been described previously in either experimental or numerical studies. Question 1) about the "missing transition" that has evaded previous initial-value solvers is answered in chapter 6, since we will see that transition to the one-vortex state occurs asymmetrically about the equator.

In Part III, we analyze the asymmetric transitions in more detail. The numerical steady-state results by Schrauf (1983), describing the mathematical structure of the solution branches, have provided the groundwork for our complementary time-dependent analysis. His steady-state results, as well as our own, are reviewed in chapter 7. The subject of chapter 8 is the antisymmetric linear instability initiating the transition to the one-vortex mode. We answer question 2) about the mechanism determining the final steady state from the history of the acceleration by showing that there is a small interval or "window", in Reynolds number, of unstable states. Chapter 9 is concerned with the non-linear development of the asymmetric transition, in particular, the energy transfer between modes. In chapter 10, we summarize the results and give suggestions for further investigation.

Figure Captions -- Chapter 1

Figure 1.1 Geometry for spherical Couette flow. The inner radius is R_1 and the outer radius is R_2 . The angular velocity of the inner sphere is Ω_1 , that of the outer sphere Ω_2 .

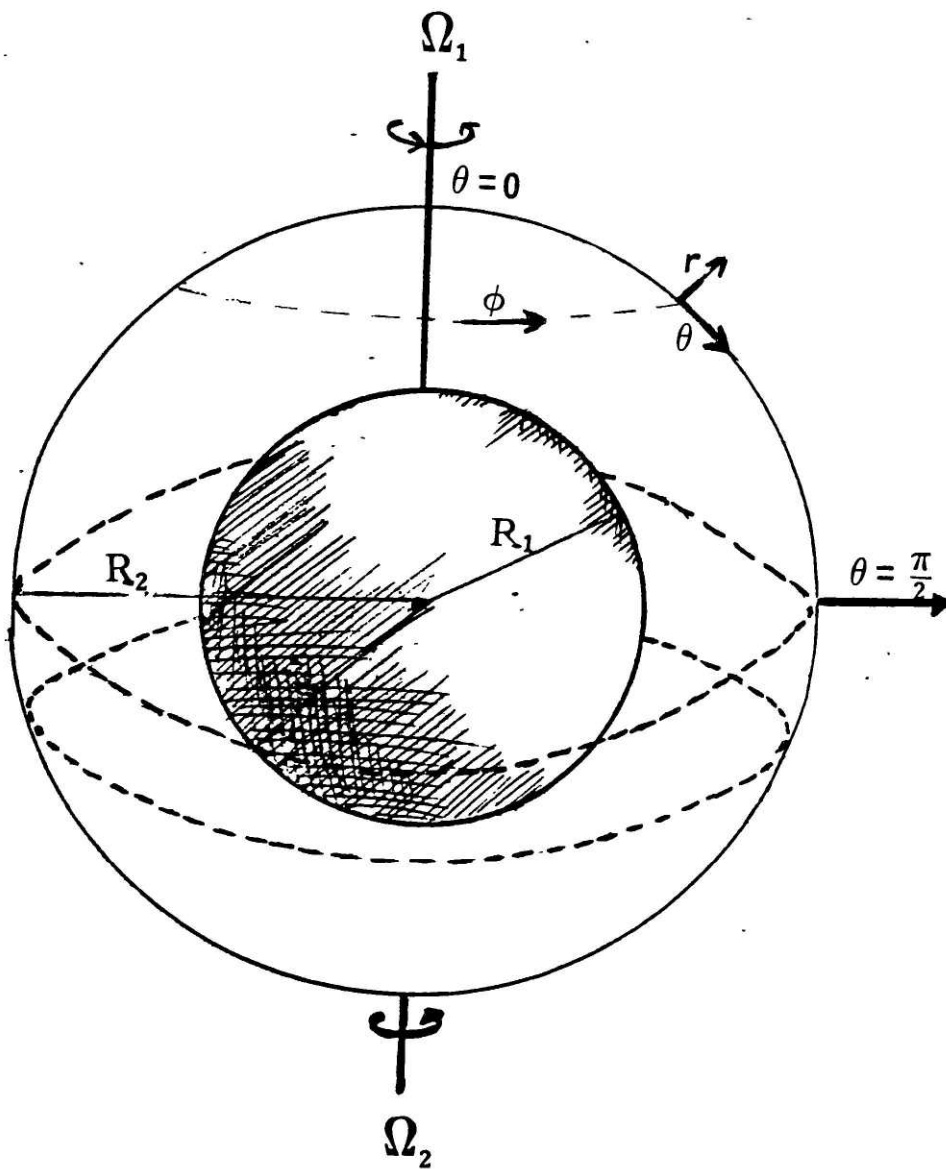


FIGURE 1.1

2. HISTORICAL SURVEY

There have been a number of investigations of spherical Couette flow, both experimental and numerical. We will survey only those relevant to the investigation of Taylor vortices. The critical Reynolds numbers at which Taylor vortices first appear (with $Re \equiv \Omega_1 R_1^2 / \nu$) are highly dependent on gap size, partly because of the use of the length scale R_1 rather than the more appropriate length scale $R_2 - R_1$ used in the standard Re for cylindrical Couette flow. If we wish to compare our data at $\sigma = 0.18$, with results for different gap sizes, it is more appropriate to use the Taylor number $Ta \equiv Re \sigma^{\frac{3}{2}}$. Note that for cylindrical Couette flow, the critical Taylor number at which Taylor vortex formation occurs is $Ta_c = 41.3$.

2.1 Discovery of Taylor vortices in spheres

Bratukhin (1961) performed a linear stability analysis for spherical Couette flow. Expanding the basic flow in powers of Re , he approximated the basic flow by the Stokes solution and the lowest order meridional flow. The axisymmetric eigenfunctions of the linearized perturbation problem are products of Legendre polynomials in θ of order L and spherical Bessel functions in radius, of the same order L . By looking only at perturbations with $L = 1$ and $L = 2$, he obtained $Ta_c = 100$ for $\sigma = 1.0$. The most unstable eigenfunction found was of the same spatial form as the basic flow, not of the Taylor vortex type. Sorokin, Khlebutin,

and Shaidurov (1966) experimentally tested the validity of Bratukhin's analysis for $\sigma = 1.0$, and indeed found only a continuous change with Taylor number, not a sudden transition. There was no qualitative change in the fluid motion. The torque (which, non-dimensionalized by $\frac{1}{2}R_1^5\Omega_1^2$, we will call τ) obeyed, for $Ta < 80$, the relation $\tau \propto (1/Re)$ which can be derived theoretically from the Stokes solution. For $Ta > 100$, the torque obeyed the relation $\tau \propto (1/Re)^{\frac{1}{2}}$, which is associated with boundary layer formation.

Khlebutin (1968) then carried out experiments in the range $.0371 < \sigma < 1.5147$. He observed the formation of Taylor vortices near the equator for $\sigma \leq 0.19$ but not for $\sigma \geq 0.44$. (His experiment did not investigate the range $0.19 < \sigma < 0.44$.) Visual observations of the transition were accompanied by an abrupt increase in the slope of the torque. Although vortices were observed for $0.12 < \sigma \leq 0.19$, a difference in the torque dependence after transition led him to distinguish between these "medium" gaps and the narrow gaps with $\sigma < 0.12$. Khlebutin calculated the the best fit over his five values of σ to be $Ta_c = 49$, which is close to the value for cylinders $Ta_c = 41.3$.

Yakushin (1969) repeated the analysis of Bratukhin for small σ (.07 and 0.1). He approximated the basic flow by the Stokes solution, pointing out that an expansion in Re for the basic flow converges more rapidly for small σ . By solving the linearized perturbation equations numerically,

he was able to investigate the stability of the basic flow to perturbations with $L \leq 30$. He found that the most unstable perturbations were indeed systems of vortices, with amplitude much greater at the equator than at the poles. Significantly, he also found that two perturbations became unstable at the critical Reynolds number, one symmetric with respect to the equator, and the other antisymmetric. He speculated that an asymmetric flow might then develop, from the basic symmetric flow. For $\sigma = 0.1$, his $Ta_c = 50.6$ is in good agreement with Khlebutin's experiments. For $\sigma = 0.07$, the agreement of his $Ta_c = 60.3$ is not as good, and Yakushin attributed this to insufficient numerical resolution. Heuristically, for good spatial resolution of Taylor vortices (assuming they have nearly circular cross-sections), the maximum L must be $\geq \pi/\sigma$, a criterion which is violated for $\sigma = 0.07$, but not for $\sigma = 0.1$.

2.2 Experimental results for $\sigma = 0.18$

Sawatzki and Zierep (1970) described spherical Couette flow in great detail for the narrow and medium gap regime. Wimmer (1976), who helped perform these experiments, later expanded their results. In both regimes, the torque τ obeyed the relation $\tau \propto (1/Re)$ for laminar flow, $\tau \propto (1/Re)^{\frac{1}{2}}$ for supercritical flow, and $\tau \propto (1/Re)^{\frac{1}{3}}$ for turbulent flow.

For the narrow gap ($\sigma = .0527$), they found a critical Taylor number of 41.3 (identical to that in cylinders) at which Taylor vortices form near the equator. According to

Sawatzki and Zierrep, for this narrow gap, at a slightly higher Reynolds number, the vortex axes form spirals and end freely in the flow field, while according to Wimmer, they remain closed and parallel to the equator. In any case, the flow field near the poles is not altered, more vortices are stacked as the Reynolds number is increased, and at a much higher Reynolds number, the vortices become wavy.

For the medium gap ($\sigma = 0.18$), at $Re > 650$ ($Ta > 49.6$) Sawatzki and Zierrep, and Wimmer observe five different stable flow modes. Three modes are axisymmetric, with zero, one, or two Taylor vortices per hemisphere. Which mode occurs at a given Reynolds number depends on the history of the flow, specifically, on how quickly the inner sphere is accelerated to its final angular velocity.

The one-vortex state, which they call Mode III, has one vortex just above and one just below the equator. The two-vortex state, their Mode IV, has two vortices above and two vortices below the equator. The one-vortex state is most easily obtained by starting with the two-vortex state and increasing the Reynolds number. Wimmer notes that this transition, accomplished by the gradual diminution of the vortices nearest the equator, occurs at $Re = 3950$ ($Ta = 302$), He also obtained the one-vortex state directly from the basic state at $Re \approx 650$ ($Ta \approx 49.6$) if the acceleration of the inner sphere is gradual. It is the one- and two-vortex flows which will be of interest to us, so we will

refer to Wimmer's results about these states throughout the thesis.

Sawatzki and Zierep's mode V is a periodic version of the one-vortex state, in which vortices, their axes no longer parallel to the equator, are periodically generated at the equator and spiral to the poles. Wimmer found a similar variation of the two-vortex state, which he called Va. Mode II of Sawatzki and Zierep contains spiral vortices which begin at the poles. Of a completely different character than the Taylor vortices, these are called Stuart vortices. Wimmer did not call this a separate mode because Stuart vortices at the poles could exist in combination with any of the equatorial Taylor vortex flows: the zero-, one-, or two- vortex steady or periodic states. Stuart vortices are always formed at $Re = 5500$ ($Ta = 420$), before the onset of turbulence.

Their Mode I (which we will call the supercritical zero-vortex state) obeys the torque relation $\tau \propto (1/Re)^{\frac{1}{2}}$ but has no vortices. Instead, according to Sawatzki and Zierep, there are boundary layers near the inner and outer spheres, and the region between them rotates like a solid body with angular velocity less than that of the inner sphere. Sawatzki and Zierep note that boundary layer formation inhibits the mechanism causing Taylor vortices. Wimmer also describes a faint and short-lived vortex carried from the equator to the poles during the establishment of this mode.

2.3 Further stability analyses

After numerically obtaining the approximation to the basic flow accurate to seventh order in Re , Munson and Joseph (1971) investigated its stability. They used energy theory, in which one calculates the growth or decay of the energy of disturbances of arbitrary size. This gives a lower bound for Re_c because the disturbance found to yield instability may not in fact be excited. Munson and Menguturk (1975) continued this study with linear stability analysis. Linear theory gives an upper bound on Re_c because the disturbances admitted are limited to the infinitesimal, and other, larger, disturbances may be excited. Munson and Joseph explain that both the energy and the linear theory are greatly complicated by the dependence of the basic flow on the Reynolds number. In each case, a linear eigenvalue problem arises that depends upon the basic flow. The eigenvalue problem not only contains Re as a parameter, but must be solved anew for each Re . The numerical calculations were only carried out for large gaps ($\sigma > .33$). For $\sigma = 1.$, Bratukhin's value, the most unstable perturbation by linear theory was axisymmetric but equatorially asymmetric, while the energy theory yielded a perturbation with neither symmetry.

Munson and Menguturk (1975) also conducted experiments. Although their primary interest was in wide gaps, they also studied a small gap ($\sigma = 0.135$) and observed Taylor vortices

at $Ta_c \approx 45-48$. Their results are in good agreement with those of Khlebutin, Yakushin, and Sawatzki and Zierrep. Munson and Menguturk compared their experimental torques with the theoretical torques calculated by Howarth (1954) for boundary layer (large Re) flow outside a rotating sphere in an infinite medium. Although these theoretical torques are intrinsically independent of gap width, they agreed well for large Re ($Re \geq 2000$) with the measured values even in the small gap $\sigma = 0.135$.

Walton (1978) carried out an analytic linear stability analysis in the narrow gap limit. He used an expansion of the basic flow in powers of $\sigma^{-\frac{1}{2}}Ta$ and σ . Considering axisymmetric and equatorially symmetric eigenfunctions only, and using matched asymptotic expansions, he found the $O(\sigma)$ correction to the cylindrical Ta_c and the number of vortices in the eigenfunction. His values compared favorably with those of Wimmer for $\sigma = 0.0527$. Finally, Soward and Jones (1983) showed specifically that the Ta_c for spheres must be slightly higher than that for cylinders, in the narrow gap limit.

2.4 Wide and narrow gap instability; results for $\sigma = 0.11$

A series of papers by Yavorskaya and others gave a definitive criterion for the difference between narrow and wide gaps. Taylor vortices form if $\sigma < 0.23$ and not if $\sigma \geq 0.24$. More precisely, the experiments of Belyaev, Monakhov, and Yavorskaya (1978) divided $Re-\sigma$ space into four

regions with quite different properties. In the lowest (in Re) region there is only basic flow. This is bounded by a curve Re_c vs. σ , above which there is a region in which the only stable flow is that with Taylor vortices. The upper boundary of this region is another curve, above which the state with no vortices remains stable if the fluid is accelerated into it quickly enough from the basic flow state. Finally, much higher, there is another transition line, smoothly connected to the line of transition for thick layers, above which the fluid becomes unstable to the thick-layer type of instabilities. These are quite different from Taylor cells; in particular, they are non-axisymmetric, equatorially asymmetric, and unsteady, as seen experimentally by Yavorskaya, Belyaev, and Monakhov (1975) with $\sigma = 0.54$.

The explanation of Belyaev et al. for the lack of Taylor vortices in wide gaps is as follows: Yavorskaya (1975) had derived an approximation for the meridional flow and showed its intensity to be $\propto Ta \sigma^{\frac{3}{2}}$. Assuming the onset of Taylor vortices occurs at a fixed Taylor number, independent of σ , we see that the intensity of the meridional flow at onset increases with σ . Belyaev et al. (1978) argue that when the meridional velocity is large enough, the redistribution of angular momentum is sufficient to suppress the instability forming Taylor cells. The suppression of the Taylor instability also exists in thin layers, and had been invoked by Sawatzki and Ziererp to explain the stability of

their mode I, the zero-vortex state at supercritical Re .

Astaf'eva, Vvedenskaja, and Yavorskaya (1978) wrote a numerical time-dependent axisymmetric program whose results they compared with the experiments of Yavorskaya, Belyaev, and Monakhov (1977). They expanded in Legendre polynomials in θ and used a finite difference mesh in radius that concentrated points at the boundaries. In time, they used forwards (Euler) differencing for the nonlinear term and backwards (implicit) differencing for the viscous term. For the thin gap ($\sigma = 0.11$) with a stationary outer sphere, they used 10 points in radius, and up to 90 Legendre polynomials in θ . They obtained states with up to four vortices in each hemisphere. There was overlap in the ranges (in Re) of stability of states, i.e. non-uniqueness.

The numerical simulation of Astaf'eva et al. agrees remarkably well with experiment, especially for states with two or more vortices. The experimental values found by Yavorskaya et al. (1977) for the lower bounds of stability of the two-, three-, and four-vortex states are $Ta \approx 48$, 56, and 63 ($Re \approx 1310$, 1550, 1730), respectively. The values computed by Astaf'eva et al. are only 2-3% higher than the experimental values.

The lower bound of stability of the one-vortex state was found numerically to be 45.8 as compared to the experimental value of 44.7. Experimentally, $Ta = 44.7$ was also found to be the the upper bound of stability of the basic

state -- it is this number which is usually called Ta_c . However, the simulation did not reproduce the upper bound of stability for the basic state. In fact, Astaf'eva et al. could not obtain a one-vortex state as a solution to the initial value problem by starting with the basic flow and merely raising Ta . They were forced to add a disturbance resembling the one-vortex state, which then evolved into a steady one-vortex state. To explain their inability to generate a one-vortex state without adding such a disturbance, Astaf'eva et al. hypothesize, based partly on experimental observations, that this transition must take place through non-axisymmetric or non-equatorially symmetric perturbations.

2.5 Numerical results for $\sigma = 0.17647$

Other numerical time-dependent simulations were also unable to obtain the one-vortex state from the basic flow. Bonnet and Alziary de Roquefort (1976) calculated the flow for a variety of gap sizes, in particular the gap size non-dimensionalized by the outer radius $(R_2 - R_1)/R_2 = 0.15$ which corresponds to $\sigma = 0.17647$, almost Wimmer's $\sigma = 0.18$. Their axisymmetric, equatorially symmetric simulation used finite differences and 65 points in both directions. At $Re = 900$ ($Ta = 66.7$), starting from rest, they obtained two vortices per hemisphere. If started from the steady $Re = 900$ solution, the flow at $Re = 1500$ ($Ta = 111.2$) retained its two-vortex structure, but, if started abruptly from rest,

did not develop vortices. This corresponds qualitatively with Wimmer's finding that no vortices were formed for $Re > 1700$ ($Ta = 118.6$) if the acceleration of the inner sphere to its final value was large.

Bartels (1982), whose methods were similar to those of Bonnet and Alziary de Roquefort, tried to generate the one-vortex mode at $\sigma = 0.17647$, first by using the small accelerations described by Wimmer as producing such a mode. Remarking, like Astaf'eva et al., that perhaps their failure to generate the one-vortex state was due to the imposition of equatorial symmetry, Bartels conducted simulations in the whole space $0 < \theta < \pi$, allowing round-off error to produce asymmetric perturbations. However, he found that this did not greatly influence the final solution. Since our study shows that asymmetric perturbations generated by round-off error substantially alter the evolution of the flow, we hypothesize that Bartels did not carry out the simulation for a sufficient time to observe this effect. Eventually, adopting the same kind of procedure as Astaf'eva et al., the solution was forced to temporarily obey a symmetry condition at 90.7 degree. When this condition was lifted, the solution then relaxed into a stable, steady, equatorially symmetric one-vortex state, provided the Reynolds number was above 700 ($Ta = 51.9$). The vortex disappeared quickly if Re was lowered below 687 ($Ta = 50.9$), and remained a solution at least until $Re = 1500$ ($Ta = 111$).

Starting from rest, the two-vortex state appeared spontaneously at $Re = 700$ ($Ta = 51.9$). For $Re > 1300$ ($Ta > 96$), a zero-vortex solution could be generated for fast enough acceleration, but changed into a two-vortex solution if Re was lowered to 1200 ($Ta = 89$). For all of these solutions, Bartels calculated torques that were agreed well with those of Wimmer. Bartels used 98 points in θ ($0 < \theta < \pi/2$) and 20 in radius for his finite difference scheme, and showed that a mesh of 32 points in θ and 10 in radius was insufficient, generating erroneous results.

Bartels obtained interesting results by varying σ . He found the maximum σ for Taylor vortex formation to be $\sigma = 0.205$ and the maximum number of vortices per hemisphere to be $n \approx .4/\sigma$. Bartel's value of $\sigma = 0.205$ differs slightly from the value $\sigma = .24$ found experimentally by Belyaev et al. (1978), perhaps due to the absence of the one-vortex state. A sudden acceleration from rest resulted in the zero-vortex state for $Ta \geq 17.5/\sigma$.

Schrauf (1983) used the continuation method of Keller to calculate steady states. This type of calculation follows solution branches, regardless of their stability, and had never previously been performed for spherical Couette flow. He studied the axisymmetric and equatorially symmetric steady states of the gap width $\sigma = 0.17647$ for $Re < 1600$, i.e. the zero-, one-, and two-vortex states. Finite differences were used, with a mesh of 11 radial and 61 or

121 θ points.

We briefly describe Schrauf's bifurcation diagram, in which the structure of the branches is far more complex than previously supposed. The most striking of Schrauf's results is that the one-vortex states lie on a separate solution branch, which does not intersect the branch containing the basic flow. Transition from the basic flow to a one-vortex state does not occur by bifurcation. The one-vortex branch has turning points at $Re = 653$ and $Re = 1065$ ($Ta = 48.4$ and $Ta = 79$); steady one-vortex states should not be observed above or below these values, according to his study. At $Re \approx 1065$, Schrauf's one-vortex branch is connected to an unstable branch along which there are both one- and two-vortex states. It then has yet another turning point at $Re \approx 800$, above which it consists of zero-vortex states. The two-vortex states occupy the same branch as the basic flow. Another interesting feature of Schrauf's diagram is the existence of yet more unconnected branches above $Re = 1300$: a one-vortex branch and a zero-vortex branch. One of the stable branches, unconnected to the others, contains zero-vortex states. It does not exist below $Re \approx 1300$ ($Ta \approx 96$) and would seem to be a good candidate for the supercritical zero-vortex states.

Our results are generally in agreement with those of Schrauf where the two studies overlap, with the following exception: in our study, we find that steady one-vortex

states continue to exist until at least $Re = 1300$. At $Re = 1200$, we generated the same steady one-vortex state by using a resolution of 16 points in radius and 128 points in θ as when a finer resolution of 16 by 256 was employed (see chapter 3 for description of our method). We attempted to reconcile this with Schrauf's result that the branch of steady one-vortex states ended at $Re \approx 1065$. This Re is also mentioned by Wimmer as corresponding to a transition to the two-vortex state when the system was accelerated very slowly. However, we found a transition from the one-vortex state to the two-vortex state to occur only by using a coarser resolution (8 points in r and 64 points in θ) at $Re = 1200$. We therefore conclude that a steady one-vortex state exists at $Re = 1200$ if sufficient resolution is employed.

3. NUMERICAL METHODS

3.1 Equations of Motion

With the assumption of axisymmetry, the four equations and variables of incompressible fluid mechanics reduce to only two. Because axisymmetry implies that the meridional part of \mathbf{u} is divergence-free (as well as \mathbf{u}), it can be written as a curl. We write

$$\mathbf{u} = \omega \mathbf{e}_\phi + \nabla \times (\psi \mathbf{e}_\phi) \quad (3.1)$$

where

$$\omega = \omega(r, \theta) \quad \psi = \psi(r, \theta)$$

Thus

$$u_r = \frac{1}{r \sin \theta} \frac{\partial \psi \sin \theta}{\partial \theta} \quad u_\theta = -\frac{1}{r} \frac{\partial r \psi}{\partial r} \quad (3.2)$$

The standard formulation (Rosenhead 1963) is

$$\mathbf{u} = \frac{1}{r \sin \theta} [\omega' \mathbf{e}_\phi + \nabla \psi' \times \mathbf{e}_\phi] \quad (3.3)$$

The relationship between the standard formulation and ours is

$$\omega' = \omega r \sin \theta \quad \psi' = \psi r \sin \theta \quad (3.4)$$

ψ' is the meridional stream function; contours of constant ψ' are streamlines of the meridional velocity. No significance is attached to this difference in formulations.

Define the operator A^2 by its action on the scalar f :

$$A^2 f \equiv \left(\nabla^2 - \frac{1}{r^2 \sin^2 \theta} \right) f \quad (3.5)$$

Note that

$$A^2 f = e_\phi \cdot \nabla^2 f e_\phi \quad (3.6)$$

and that if f is axisymmetric, then

$$e_\phi \cdot \nabla \times [\nabla \times (f e_\phi)] = -A^2 f \quad (3.7)$$

The equation for the ϕ component of u is

$$\frac{\partial \omega}{\partial t} = e_\phi \cdot u \times (\nabla \times u) + \frac{1}{Re} A^2 \omega \quad (3.8)$$

while the equation for the ϕ component of $\nabla \times u$ is

$$\frac{\partial A^2 \psi}{\partial t} = -e_\phi \cdot \nabla \times [u \times (\nabla \times u)] + \frac{1}{Re} A^4 \psi \quad (3.9)$$

The no-slip boundary conditions on ω are

$$\begin{aligned} \omega &= \Omega_1 R_1 \sin \theta \quad \text{at } r = R_1 \\ &= 0 \quad \text{at } r = R_2 \end{aligned} \quad (3.10)$$

The velocity cannot be singular at the poles:

$$\omega = 0 \quad \text{at } \theta = 0, \pi \quad (3.11)$$

although the angular velocity $\frac{\omega}{r \sin \theta}$ is generally non-zero.

We decompose ω into

$$\omega = \bar{\omega} + \tilde{\omega} \quad (3.12)$$

where $\bar{\omega}$ satisfies the inhomogeneous boundary conditions (3.10-.11) and the equations

$$A^2 \bar{\omega} = 0 \quad \frac{\partial \bar{\omega}}{\partial t} = 0 \quad (3.13)$$

That is, $\bar{\omega}$ is the (steady) Stokes solution

$$\bar{\omega} = \left(\alpha r + \frac{\beta}{r} \right) \sin \theta \quad (3.14)$$

$$\text{where } \alpha \equiv \frac{-\Omega_1 R_1^3}{R_2^3 - R_1^3} \quad \text{and} \quad \beta \equiv \frac{R_1^3 R_2^3}{R_2^3 - R_1^3}$$

and is not a solution to the full nonlinear equations. The function $\tilde{\omega}$ satisfies the same equation as ω , that is

$$\frac{\partial \tilde{\omega}}{\partial t} = \mathbf{e}_\phi \cdot \mathbf{u} \times (\nabla \times \mathbf{u}) + \frac{1}{\text{Re}} A^2 \tilde{\omega} \quad (3.15)$$

but with homogeneous boundary conditions

$$\tilde{\omega} = 0 \quad \text{at} \quad r = R_1, R_2 \quad (3.16)$$

$$\tilde{\omega} = 0 \quad \text{at} \quad \theta = 0, \pi \quad (3.17)$$

Boundary conditions for Ψ are derived as follows: The condition

$$u_r = 0 \quad \text{at} \quad r = R_1, R_2 \quad (3.18)$$

implies that $\Psi' = \Psi r \sin \theta$ is constant on each of R_1, R_2 . The constraint of axial symmetry that there be no flow across the poles

$$u_\theta = 0 \quad \text{at} \quad \theta = 0, \pi \quad (3.19)$$

implies that the two constants are the same. This constant is arbitrary (only $\nabla \Psi'$ is significant) and can be set to zero. Since Ψ' is zero on each of R_1, R_2 then also

$$\Psi = 0 \quad \text{at} \quad r = R_1, R_2 \quad (3.20)$$

The boundary condition

$$u_\theta = 0 \quad \text{at} \quad r = R_1, R_2 \quad (3.21)$$

along with equation (3.20) implies that

$$D\Psi \equiv \frac{\partial \Psi}{\partial r} = 0 \quad \text{at} \quad r = R_1, R_2 \quad (3.22)$$

Axisymmetry requires u_θ to be an odd function of θ (a sine series), and u_r an even function of θ (a cosine series).

These imply that ψ is odd, so that

$$\psi = 0 \quad \text{at} \quad \theta = 0, \pi \quad (3.23)$$

3.2 Spatial approximation

We use a pseudo-spectral method (Lanczos 1956, Gottlieb and Orszag 1977). Functions are represented in spectral space, as a finite series of N basis functions. Derivatives are taken in spectral space, where the derivative operator is exact. Multiplications are convolutions in spectral space, and are expensive (requiring $O(N^2)$ operations) and inexact (introducing aliasing). Therefore we perform our multiplications in physical space, where they are exact and inexpensive, requiring only N operations per multiply. The advantages of the pseudo-spectral method are lost if the transforms between spectral and physical space are numerically time-consuming.

Each term in our spectral sum is a product of a basis function in θ and a basis function in r . In the radial direction, we use Chebyshev polynomials, which are normalized such that $T_n(x) \equiv \cos[n \cos^{-1}(x)]$. Taking the Chebyshev transform of a function sampled at the collocation points $x_k = \cos(\frac{k\pi}{N})$ is accomplished by a Fast Fourier Transform. The spacing of the Chebyshev collocation points is denser at the boundaries ($O(\frac{1}{N})^2$) than in the interior ($O(\frac{1}{N})$), enabling boundary layers to be adequately resolved with small N . Since Chebyshev polynomials are solutions to

a singular Sturm-Liouville problem, their spectral sums converge exponentially fast.

We use Fourier series in the θ direction. Previous authors (e.g. Bratukhin 1961, Yakushin 1969, Munson and Joseph 1971, Astaf'eva et al. 1978) have expanded in Legendre polynomials because they are the natural basis functions for a spherical geometry, in that they are the eigenfunctions of the θ part of the Laplacian (the associated Legendre polynomials P_n^1 are the eigenfunctions of the θ part of the operator A^2 defined above). However, we have chosen to expand in Fourier series to take advantage of Fast Fourier Transforms. Although analagous fast Legendre transforms are in theory possible, at present they are not as fast and standard as their Fourier counterparts. There is no advantage in using eigenfunctions of A^2 if the time saved in inverting the linear operator would be spent in the transforms necessitated by the nonlinearity of the problem. A^2 is not diagonal in a Fourier series basis, but it is upper triangular, which is still advantageous, as we will see in section 3.4.

Both sine series and cosine series are complete in the interval $0 \leq \theta \leq \pi$. The homogeneous boundary conditions (3.17) and (3.23) dictate the use of a sine series $f = \sum f_n \sin n\theta$ for both $\tilde{\omega}$ and ψ . Each of the basis functions $\sin n\theta$ satisfies the homogeneous boundary conditions in θ ; this is the Galerkin method (Gottlieb and Orszag 1977)

of imposing boundary conditions. No Gibbs phenomenon can arise from the sine expansion since the velocities are periodic in θ and have no discontinuities. We do not restrict the expansion to equatorially symmetric fields, which would consist of using only the functions $\sin n\theta$ with odd n for ω and with even n for ψ .

Although convenient to work with, sine series have the disadvantage of sampling equally spaced points in θ (i.e. their roots are equally spaced), whereas the flow we are studying has most of its spatial structure at the equator. Legendre series would not provide much improvement since their roots are nearly equally spaced in θ . It is possible that the most economical approach overall would be to map from the upper half-circle $0 < \theta < \pi/2$ to the interval $[0,1]$, and from the lower half-circle $\pi/2 < \theta < \pi$ to the interval $[-1,0]$, imposing matching conditions at the equator, and using Chebyshev polynomials on each interval. In this way, the equatorial region would be mapped to the boundaries of two intervals, where the Chebyshev collocation points are densely spaced. Using a Chebyshev representation, with its small spacing between points, would not present a problem with respect to stiffness because there is little or no flow across the equator.

3.3 Temporal approximation

We now consider the approximation of time derivatives. Implicit methods are more stable than explicit

methods, allowing larger time steps to be taken. They are, however, impractical with the nonlinear term of the Navier-Stokes equations. We use a globally second-order accurate Adams-Bashforth approximation with the nonlinear terms. With the viscous term, we use the Crank-Nicolson approximation, which also has global accuracy $O(\Delta t)^2$. The Crank-Nicolson approximation is implicit, eliminating what would be the very stringent stability requirement on Δt due to viscosity. The over-all time-stepping equation, of global accuracy $O(\Delta t)^2$, is, with J representing a nonlinear operator and f representing $\tilde{\omega}$ or $A^2\psi$

$$f(t+\Delta t) = f(t) + \frac{\Delta t}{2} [3J(f(t)) - J(f(t-\Delta t))] + \frac{\Delta t}{2} \left[\frac{1}{Re} A^2 f(t) + \frac{1}{Re} A^2 f(t+\Delta t) \right] \quad (3.24)$$

Define the operator C^2 arising from the Crank-Nicolson approximation by

$$C^2 \equiv \left(I - \frac{\Delta t}{2Re} A^2 \right) \quad (3.25)$$

and the nonlinear terms J_ω and J_ψ by

$$J_\omega \equiv e_\phi \cdot [u \times (\nabla \times u)] \quad (3.26)$$

$$J_\psi \equiv - e_\phi \cdot \nabla \times [u \times (\nabla \times u)]$$

The complete algorithm is then

$$C^2 \tilde{\omega}(t+\Delta t) = \frac{\Delta t}{2} [3J_\omega(t) - J_\omega(t-\Delta t)] + \left(I + \frac{\Delta t}{2Re} A^2 \right) \tilde{\omega}(t) \quad (3.27)$$

subject to the boundary conditions (3.16)

$$C^2 \xi(t+\Delta t) = \frac{\Delta t}{2} [3J_\varphi(t) - J_\varphi(t-\Delta t)] \quad (3.28)$$

$$+ \left(I + \frac{\Delta t}{2\text{Re}} A^2 \right) \xi(t)$$

$$A^2 \psi = \xi \quad (3.29)$$

The last two equations obey boundary conditions (3.20) and (3.22)

3.4 Solution of elliptic equations

Our method requires us to solve two elliptic equations

$$C^2 f = g \quad (3.30)$$

$$\text{and } A^2 f = g \quad (3.31)$$

Consider (3.31), which is the simpler of the two. Define the operators A_r^2 and A_θ^2 by

$$A_r^2 \equiv \frac{\partial}{\partial r} r^2 \frac{\partial}{\partial r} \quad A_\theta^2 \equiv \frac{1}{\sin\theta} \frac{\partial}{\partial \theta} - \frac{1}{r^2 \sin^2 \theta}$$

(3.32)

so that

$$r^2 A^2 = A_r^2 + A_\theta^2 \quad (3.33)$$

A_r^2 contains only radial derivatives, and multiplication by functions of r . A_θ^2 consists only of derivatives in θ and multiplication by functions of θ . Because $r^2 A^2$ is separable, it is easier to solve $(r^2 A^2) f = r^2 g$ than $A^2 f = g$.

The representation of A_θ^2 in sine- θ space is upper triangular. In fact, half of the upper triangular elements are zero because A^2 is parity preserving. In this representation specifically each element is defined

$$a_{jk} \equiv A_{\theta}^2(j,k) = \begin{matrix} -j(j+1) & \text{for } k=j \\ -2j & \text{for } k>j, j+k \text{ even} \end{matrix} \quad (3.34)$$

A_r^2 is not upper triangular in Chebyshev space because boundary conditions are imposed at $r = R_1, R_2$. For this reason, and because of the necessity of multiplying and dividing by r^2 , we solve the equation in a mixed representation of physical- r and spectral θ . A_r^2 is first calculated in Chebyshev space by computing its action on Chebyshev polynomials. The resulting matrix is transformed so as to act in physical- r space. (Vectors in physical- r space consist of function values at the Chebyshev collocation points.)

The full operator $r^2 A^2$ can be written as a block matrix

$$\left[\begin{array}{c|c|c|c|c} A_r^2 + a_{11}I & 0 & a_{13}I & 0 & \cdot \cdot \cdot \\ \hline 0 & A_r^2 + a_{22}I & 0 & a_{24}I & \cdot \cdot \cdot \\ \hline 0 & 0 & A_r^2 + a_{33}I & 0 & \cdot \cdot \cdot \\ \hline \cdot & \cdot & \cdot & \cdot & \cdot \\ \cdot & \cdot & \cdot & \cdot & \cdot \\ \cdot & \cdot & \cdot & \cdot & \cdot \end{array} \right]$$

(3.35)

where I is the identity matrix and where a_{jk} are defined in equation (3.34). The equation to be solved is

$$r^2 A^2 \begin{bmatrix} f_1 \\ f_2 \\ f_3 \\ \vdots \\ \vdots \end{bmatrix} = \begin{bmatrix} g_1 \\ g_2 \\ g_3 \\ \vdots \\ \vdots \end{bmatrix} \quad (3.36)$$

In (3.36) f_j is the function of r which is the coefficient of $\sin(j\theta)$. The submatrices of $r^2 A^2$ act on the functions f_j .

Because (3.35) is block upper triangular, the equation can be solved by a sub-matrix back-solve. Let N_r be the number of points (or polynomials) in r , N_θ the number of points in θ . We reduce the $N_\theta N_r \times N_\theta N_r$ matrix equation to N_θ matrix equations, each $N_r \times N_r$, one for each "row" of (3.35-3.36) The last (N_θ) row gives

$$(A_r^2 + a_{N_\theta, N_\theta} I) f_{N_\theta} = g_{N_\theta} \quad (3.37a)$$

The second to last ($N_\theta-1$) row is

$$(A_r^2 + a_{N_\theta-1, N_\theta-1} I) f_{N_\theta-1} = g_{N_\theta-1} \quad (3.37b)$$

The $N_\theta-2$ row is (3.37c)

$$(A_r^2 + a_{N_\theta-2, N_\theta-2} I) f_{N_\theta-2} + c_{N_\theta-2, N_\theta} f_{N_\theta} = g_{N_\theta-2}$$

The $N_\theta-3$ row is (3.37d)

$$(A_r^2 + a_{N_\theta-3, N_\theta-3} I) f_{N_\theta-3} + c_{N_\theta-3, N_\theta} f_{N_\theta} = g_{N_\theta-3}$$

and so on.

Each of the $N_r \times N_r$ matrix equations (3.37) is to be solved by an eigenvector-eigenvalue, or Zang-Haidvogel (1979), factorization. Each of the matrix operators

$(A_r^2 + a_{jj}I)$ has the same eigenvectors; its eigenvalues are merely shifted by a_{jj} . Therefore the factorization need be done only once. We store only A_θ^2 and the eigenvector-eigenvalue decomposition of A_r^2 . The number of operations required is $O(N_r N_\theta^2 + N_\theta N_r^2)$. The eigenvector-eigenvalue solution of the full matrix would require $O(N_r^2 N_\theta^2)$ operations. The total storage needed is $O(N_r^2 + N_\theta^2)$, as compared to $N_r^2 N_\theta^2$ for the whole matrix.

The requirement for stability for an ordinary back-solve is diagonal dominance. The analogous requirement for a sub-matrix back-solve is that $|A_r^2 + a_{jj}I| < |a_{jk}I|$ for all $k \neq j$ (where the norm $|\cdot|$ of a vector is its largest element). This requirement is due to the fact that at step j of the back-solve, each error $\epsilon_k, k > j$, is multiplied by $a_{jk} \cdot (A_r^2 + a_{jj}I)^{-1}$. Equivalently, $|\lambda + a_{jj}|$ must be greater than $|a_{jk}|$ for all eigenvalues λ of A_r^2 and for all $k \neq j$. This condition is met for the matrices we use.

We proceed the same way for the matrix C^2 of (3.25)

$$\begin{aligned} r^2 C^2 &= r^2 \left(I - \frac{\Delta t}{2Re} A^2 \right) & (3.38) \\ &= \left[r^2 I - \frac{\Delta t}{2Re} A_r^2 \right] - \left[\frac{\Delta t}{2Re} A_\theta^2 \right] \\ &\equiv C_r^2 + C_\theta^2 \end{aligned}$$

where A_r^2 and A_θ^2 are defined as before.

To finish solving for $\tilde{\omega}$ it remains only to impose the boundary conditions (3.16). This is done by substituting the radial boundary conditions into the boundary rows of

each of the N_θ sub-matrix equations. Homogeneous Dirichlet conditions are particularly simple to apply, requiring us merely to drop the boundary rows and columns from each sub-matrix $C_r^2 + a_{jj}I$. There remains a set of N_θ sub-matrix equations, each of which is now of size $(N_r-2) \times (N_r-2)$.

Imposing the homogeneous Cauchy boundary conditions (3.20, 3.22) on ψ while solving equations (3.27 -.28) for ξ and ψ is more complicated. There are no boundary conditions for ξ , while there are four boundary conditions for ψ . The complications in the fourth-order system are due to the elimination of the pressure and of one velocity component.

We use the set of Greens functions h_{jk} which are the solutions to the homogeneous equation

$$C^2 A^2 h = 0 \quad (3.39)$$

with boundary conditions

$$\begin{aligned} A^2 h_{jk}(r, \theta) &= \delta_{r, R_j} \delta_{\theta, \theta_k} & j = 1 \text{ or } 2 ; \quad k = 1, \dots, N_\theta \\ h_{jk}(r, \theta) &= 0 & \text{at } r = R_1, R_2 \end{aligned} \quad (3.40)$$

Solving for each of the $2 \cdot N_\theta$ solutions h_{jk} requires $O(N_\theta^3 N_r)$ operations, but is only done once, in a pre-processing step. At each iteration, we use the Greens functions to compute ψ by:

1) Solving

$$r^2 C^2 \xi = r^2 g \quad (3.41)$$

where g is the right hand side of (3.28), subject to arbitrary boundary conditions. In practice, we use the homogeneous Dirichlet boundary conditions, i.e. $\xi=0$ at R_1, R_2 , since the matrix and procedure are those used in solving for $\tilde{\omega}$.

2) Solve

$$r^2 A^2 \psi_p = r^2 \xi \quad (3.42)$$

for a particular solution ψ_p , imposing homogeneous Dirichlet boundary conditions.

3) Form the homogeneous solution ψ_h : the linear combination of the solutions h which satisfies

$$D \psi_h = -D \psi_p \quad (3.43)$$

4) Finally, set

$$\psi = \psi_p + \psi_h \quad (3.44)$$

so that ψ satisfies (3.22), as well as (3.20) and (3.27-28).

Since each h has $(N_r - 2)N_\theta$ entries, the storage for all h_{jk} 's (denoted by H) is $2(N_r - 2)N_\theta^2$, by far the largest array required, since we generally use $N_\theta = 128$ and $N_r = 16$. It is possible to reduce the storage at the expense, as usual, of an increase (20%) in the time per iteration. Rather than storing all of H , we need only store the boundary rows of $D H$, a total of $4N_\theta^2$ entries. Two additional sub-matrix back-solves are then necessary to find the appropriate homogeneous solution to add to the particular ψ .

3.5 Eigenvectors and eigenvalues; unstable equilibria

The calculation of eigenvectors and eigenvalues requires little modification of the computational method. The linearized Navier-Stokes equations, governing the linear evolution of a perturbation \mathbf{u} to a given equilibrium \mathbf{U} is

$$\frac{\partial \mathbf{u}}{\partial t} = \mathbf{Q}(\mathbf{U}) \mathbf{u} \quad (3.45)$$

$$(\mathbf{Q}(\mathbf{U})) (\mathbf{u}) \equiv - (\mathbf{u} \cdot \nabla) \mathbf{U} - (\mathbf{U} \cdot \nabla) \mathbf{u} - \nabla P + \frac{1}{\text{Re}} \nabla^2 \mathbf{u}$$

where P is such that $\frac{\partial \mathbf{u}}{\partial t}$ is divergence-free and where \mathbf{u} satisfies homogeneous boundary conditions. The full nonlinear interaction must be replaced by the cross terms

$$- (\mathbf{u} \cdot \nabla) \mathbf{U} - (\mathbf{U} \cdot \nabla) \mathbf{u} \quad (3.46)$$

Specifically, this involves replacing the nonlinear terms J_ω and J_ψ defined in (3.26) by

$$\begin{aligned} J'_\omega &\equiv \mathbf{e}_\phi \cdot [\mathbf{U} \times (\nabla \times \mathbf{u}) + (\mathbf{u} \times (\nabla \times \mathbf{U}))] \\ J'_\psi &\equiv - \mathbf{e}_\phi \cdot [\nabla \times (\mathbf{U} \times (\nabla \times \mathbf{u})) + \nabla \times (\mathbf{u} \times (\nabla \times \mathbf{U}))] \end{aligned} \quad (3.47)$$

We then use exactly the time-stepping algorithm (3.27-3.29) whose implementation we have described above. By letting \mathbf{u} evolve in time, it converges to the eigenvector with the largest growth rate. This is an application of the power method (e.g., Dahlquist and Bjork 1974). Note that by using (3.27-.29) we are not finding the eigenvectors and eigenvalues of $\mathbf{Q}(\mathbf{U})$, but of an operator which is an approximation to $\exp(\mathbf{Q}(\mathbf{U})\Delta t)$, valid to second order in Δt . By using the power method on $\mathbf{Q}(\mathbf{U})$, we would obtain the

eigenvalue of largest magnitude, approximately $-\frac{1}{\text{Re}}(N_r^2 + N_\theta^2)$, which is negative. Its associated eigenvector is a high frequency mode with fast viscous decay, not the growing instability we seek.

The largest eigenvalue $\exp(\lambda\Delta t)$ of $\exp(Q(U)\Delta t)$ is approximated by the Rayleigh quotient

$$\frac{(\mathbf{u}(t), \mathbf{u}(t+\Delta t))}{(\mathbf{u}(t), \mathbf{u}(t))} \quad (3.48)$$

where $\mathbf{u}(t+\Delta t)$ is the solution of the linearized equations (3.42 - .45). The simplest possible inner product is used in (3.48),

$$(\mathbf{u}_1, \mathbf{u}_2) = \sum_{n,r} [\omega_1(n,r)\omega_2(n,r) + \psi_1(n,r)\psi_2(n,r)] \quad (3.49)$$

where $f(n,r)$ is the coefficient of $\sin n\theta$ at r . We normalize \mathbf{u} at each time step, so the denominator of (3.48) need not be calculated separately. The eigenvalue of $Q(U)$ is λ , the growth rate of \mathbf{u} , and the eigenvectors of the two operators are the same.

The power method converges linearly: the error in the approximation decreases by a factor of $\exp[-(\lambda-\lambda')\Delta t]$ where λ' is the next largest positive eigenvalue of $Q(U)$. However, good initial guesses are available, and we are able to use the growing eigenvector at one Reynolds number as an initial guess for its neighbor. Convergence may be improved in the ways usually used with the power method: shifting and relaxation. Both are accomplished by adding to the new approximate eigenvector a multiple of the previous approxi-

mation. In this calculation, we did not find that either shifting or relaxation yielded a significant improvement.

Knowing that an initial value code will pick up and amplify instabilities like an experiment, the question may arise of how we have calculated the unstable equilibria U whose growing eigenvectors we seek. The answer is that we have only had need to calculate states which are unstable in a very manageable way: they are stable to all equatorially symmetric perturbations, but unstable to an equatorially antisymmetric eigenvector. To calculate these unstable equilibria U , we merely set the antisymmetric part of the flow field to zero after each time step. It is easy to suppress an instability when its form is known. In doing this, we have basically duplicated the symmetric initial value calculations of previous authors (Bartels 1982, Bonnet and Alziary de Roquefort 1976, and Astaf'eva et al. 1979).

4. TESTS

In this section, we present comparisons of several aspects of our simulations with previous work. We then describe the results of internal tests of our code.

4.1 Transitions and limits of stability

As previously noted, critical Reynolds numbers, with $Re \equiv \Omega_1 R_1^2 / \nu$ are highly dependent on gap size (partly because of the use of the length scale R_1 rather than the more appropriate $R_2 - R_1$). To compare our data at $\sigma = .18$, with results for different gap sizes, it is more appropriate to use the Taylor number $Ta \equiv Re \sigma^{\frac{1}{2}}$. For cylindrical Couette flow with infinite, ratio, it has been found that Ta_c approaches a value $Ta_c = 41.3$ (see DiPrima and Swinney 1981) as σ approaches zero. For spherical Couette flow, Khlebutin (1968) has experimentally determined a value of $Ta_c \approx 49.0$ as the best fit over several different gap sizes. Nevertheless, different gap sizes yield flows that differ, even qualitatively. In Table 4.1, we present several different kinds of critical Taylor numbers, for our simulation and also for the studies described in the introduction. In some studies, the comparable numbers are given only graphically; we have indicated such approximate values by a "~". Reynolds numbers are presented from our simulation and from the experiments of Wimmer (1976), the only studies to use exactly $\sigma = 0.18$.

Formation of Taylor vortices may involve hysteresis, so that the lower limit of stability or existence of a given state (designated by "lowest one" and "lowest two" in the Table) may differ from that of its onset (designated by "zero to one" and "zero to two"). Some experimental studies (Yavorskaya 1977) have specifically stated that hysteresis did not occur in their measurements; our simulation shows hysteresis in the zero- to one- vortex transition, but to an almost undetectable extent. When experimentalists did not specify which kind of critical value they had calculated, we assumed it referred to onset. Not all numerical studies can measure both kinds of Ta_c . A linear stability analysis can only measure the Taylor number at onset of vortex formation. Previous initial value codes -- those of Bartels (1982), Astaf'eva et al.(1978), and Bonnet et al.(1976) -- which sought to measure Ta_c at onset of the one-vortex state, in fact were unable to reproduce this transition.

4.2 Torques

The most common experimental measurement in Taylor-Couette flow is the torque required to keep the inner sphere rotating at the angular velocity associated with the given Reynolds number. In the steady state this is equal to the torque exerted by the fluid on the stationary outer sphere. The non-dimensionalization for the torque used by Wimmer, Bartels, and Schrauf is

$$\tau = \frac{T}{\frac{1}{2}R_1^5\Omega_1^2} \quad (4.1)$$

The torque for Stokes flow is exactly

$$\tau_{\text{STOKES}} = \gamma / \text{Re} \quad (4.2)$$

where

$$\gamma \equiv 16\pi / \left(1 - \frac{R_1^3}{R_2^3}\right) \quad (4.3)$$

$\gamma = 128.43$ for $\sigma = 0.18$. Wimmer, Khlebutin, and Munson and Menguturk indeed find experimentally that $\tau \approx 1/\text{Re}$ for spherical Couette flow below Re_c . In Figure 4.1, we show the values of $\tau/\tau_{\text{STOKES}} = \tau \text{Re}/\gamma$ from our numerical simulations (solid line) and from Wimmer's experimentally measured torques (O's, from Wimmer, private communication) for $\text{Re} \leq 600$. Wimmer's measurements are systematically about 7% higher than our torques, but also 7% higher than that of Stokes flow even for $\text{Re} = 176$ (the lowest Reynolds number measured by Wimmer). At such a low Reynolds number (recall that the corresponding Reynolds number based on the gap width is 32), such a large deviation from Stokes flow would not be expected. We therefore suggest that Wimmer's torques contain an excess of about 0.07 of the Stokes torque. the presence of the rods necessary for turning the inner sphere (Zierep, private communication) or to the intrinsic difficulty in measuring torques to this accuracy (Koschmieder, private communication). This is not important for Wimmer's comprehensive study, which ranged over four decades of Re , from laminar flow through turbulence, and where τ varied from 0.032 to 0.782, but is important for our detailed study

of the differences between the zero-, one-, and two- vortex states for $Re \leq 1500$, whose torques differ by as little as 2%.

With vortices, Wimmer finds $\tau \approx (1/Re)^{\frac{1}{2}}$, which is roughly what is found by Khlebutin and Munson and Menguturk. In Figure 4.2, we show $\tau Re/\gamma$ for $200 \leq Re \leq 1200$. Our zero-, one-, and two- vortex states are on the solid curve, short-dashed curve, and long-dashed curve respectively. Wimmer's values, with 0.07 subtracted from each, are located at the numerals 0, 1, and 2, indicating the number of vortices.

4.3 Sizes of vortices

Although Taylor vortices are approximately circular, so the ratio λ of their height to the gap width is near one, Wimmer found that the exact size of the vortices is strongly dependent on Reynolds number. He measured the size of the vortex nearest the equator for both one and two vortex states, and found that their size varied from 0.54 to 1.3. This enables us to make another comparison of our numerical results with his experiment. Unlike the torque, which is a property of the entire flow field (most of which has no vortices), the vortex size is a very local measurement. It shows marked changes as a critical Reynolds number is approached and is therefore well-suited for indicating the turning point of a secondary branch by a near-vertical tangent (Benjamin 1978b).

In Figure 4.3, we show the sizes of the vortices for $600 \leq \text{Re} \leq 1200$. Wimmer's experimental points (private communication) are indicated as before by the numerals representing the number of vortices in the state. The short-dashed curve is the one-vortex state from our simulation. We show the size of both of the vortices in the two-vortex states by displaying the location of the boundaries of the vortices with the long-dashed and solid curves. These two curves almost meet at $\text{Re} = 740$, the lowest Reynolds number for which we have found that the two-vortex state exists, indicating that the vortex farther from the equator is infinitesimal at onset. Our curves again systematically exceed most of Wimmer's data, beginning at about 5% at $\text{Re} = 900$ and increasing with Re to 10% at $\text{Re} = 1200$. In our favor, though, we note that the three "1's" above $\text{Re} = 900$ which lie closest to our curve are taken from a separate experiment in which "in the lower range of Re the angular velocity is changed very carefully and slowly" (Wimmer 1976). These are then likely to be the true steady values, and our agreement with them is extremely good.

4.4 Internal tests

The exact equations of motion satisfy the integrated laws of conservation of angular momentum and conservation of energy. For any scalar F , we adopt the notation $\Delta F \equiv F(t'') - F(t')$ and $\int F \equiv \int_{t'}^{t''} F(t) dt$. Multiplying both sides of the ϕ component of the Navier-Stokes equations through by

$r \sin \theta$ (the distance from the axis of rotation), and integrating over volume and time, we get

$$\Delta A = \int \dot{A} = \int [\tau_2 - \tau_1] \quad (4.4)$$

where the angular momentum is

$$A = \int r \sin \theta u_\phi dV \quad (4.5)$$

and the torques are

$$\tau_i = \frac{1}{Re} \int r \sin \theta \left[\frac{\partial u_\phi}{\partial r} - \frac{u_\phi}{r} \right] dS \quad (4.6)$$

where the integral for τ_i is evaluated at R_i .

We calculate $\tau_i(t)$ at each step, and integrate in time to $O(\Delta t)^2$ by using the trapezoidal rule. $\int [\tau_2 - \tau_1]$ should be equal to ΔA to order $(\Delta t)^2$, where A is computed directly by numerical integration of equation (4.3). The energy conservation law is

$$\Delta E = \int \dot{E} dt = \int [\dot{E}_{in} - \dot{E}_{dis}] dt \quad (4.7)$$

The rate of energy input is proportional to the angular velocity times the torque at the inner wall

$$\dot{E}_{in} = \frac{1}{2} \Omega_1 \tau_1 \quad (4.8)$$

(The factor of $\frac{1}{2}$ arises from the non-dimensionalization (4.1)). The viscous dissipation of energy is

$$\begin{aligned} \dot{E}_{dis} &= \frac{1}{Re} \int \mathbf{u} \cdot \nabla^2 \mathbf{u} dV - \dot{E}_{in} \\ &= \frac{1}{Re} \left(\frac{16\pi}{3} + \int |\nabla \times \mathbf{u}|^2 dV \right) \end{aligned} \quad (4.9)$$

Again using the trapezoidal rule to integrate in time, equa-

tion (4.5) should be correct to $O(\Delta t)^2$.

We have found that $\Delta A - \int \dot{A}$ and $\Delta E - \int \dot{E}$, as well as the errors in A and E themselves, vary like $(\Delta t)^2$.

In addition, for each numerical initial value experiment, the fractional errors $(\Delta A - \int \dot{A})/\Delta A$ and $(\Delta E - \int \dot{E})/\Delta E$ should be small compared to ΔA and ΔE themselves. It is a more stringent test if the flow changes a great deal. In Table 4.2, we present data for the values of these quantities for such a run, a transition from a zero- to a one- vortex state. The parameter values are those we will actually use: $\Delta t = \text{inner rotation period} / 70$, $N_{\theta} = 128$, and $N_r = 32$. The units of Table 4.2 are those we will use elsewhere: ΔA is non-dimensionalized by $\frac{1}{2} R_1^5 \Omega_1^2$, while ΔE has been divided by the energy of the Stokes solution.

The initial state for the data in Table 4.2 is a steady zero-vortex state at $Re = 650$. The Reynolds number is set abruptly to $Re = 700$ by lowering the viscosity. From revolution 0 to 7 there is a systematic undershoot and overshoot, as a meta-stable zero-vortex state is reached. From revolution 7 to 27 there are slowly decaying oscillations about the meta-stable state, and from revolution 27 to 80 the change from a zero- to a one-vortex state takes place. Since the values of A and E oscillate, we have divided the run into periods in which they change monotonically.

The conservation tests are not only a check of the

internal consistency of the code, but also of the temporal resolution. This is important since we will describe the evolution of the transitions in time as well as the steady states. The spatial resolution of $N_r = 16$ and $N_\theta = 128$ has also been checked, by comparison with runs at higher resolution. It has been noted (Bartels 1982) that results are especially sensitive to the resolution in θ . Recall that we study the entire hemisphere $0 < \theta < \pi$ whereas previous numerical simulations have assumed equatorial symmetry and used only $0 < \theta < \pi/2$. However, the spectral method we use should require fewer spectral coefficients than the number of sample points required by finite difference calculations.

Our results are of three types: transitions, eigenvectors, and steady states. We find that the transitions occurring either when N_θ is set to 256, or when N_r is set to 32 are the same as those occurring with our 16 by 128 resolution. An eigenvalue calculated with $N_\theta = 256$ points agrees to five significant digits with the eigenvalue calculated using $N_\theta = 128$. We find that for $Re \leq 1200$, the resolution of 16 by 128 is adequate, yielding steady states which are identical to those produced using a finer (16 by 256) resolution. However, the use of $N_r = 8$ and $N_\theta = 64$ at $Re = 1200$ yields different, and therefore erroneous, results.

Figure Captions -- Chapter 4

Figure 4.1 Torque / Stokes torque for $Re \leq 600$. Solid line shows torques of states numerically computed by this study, 0's are the experimental torques of Wimmer (private communication). Note that the experimental points exceed 1 by about 7% as Re approaches 0.

Figure 4.2 Torque / Stokes torque for $200 \leq Re \leq 1200$. Numerically computed zero-, one-, and two-vortex states are on the solid curve, short-dashed curve, and long-dashed curve respectively. Wimmer's values (private communication), with 0.07 subtracted from each, are located at the numerals 0, 1, and 2, indicating the number of vortices.

Figure 4.3 Vortex sizes in units of the gap size. The short-dashed curve is the size of the vortex in the numerically computed one-vortex states. The long-dashed curve is the size of the vortex nearest the equator in the numerically computed two-vortex states. The size of the second vortex in the two-vortex state is the difference between the solid curve and the long-dashed curve. Note that the solid and long-dashed curves almost meet at $Re = 740$, indicating that the second vortex is infinitesimal at onset. Wimmer's experimental points (private communication) are indicated by numerals representing the number of vortices in the state.

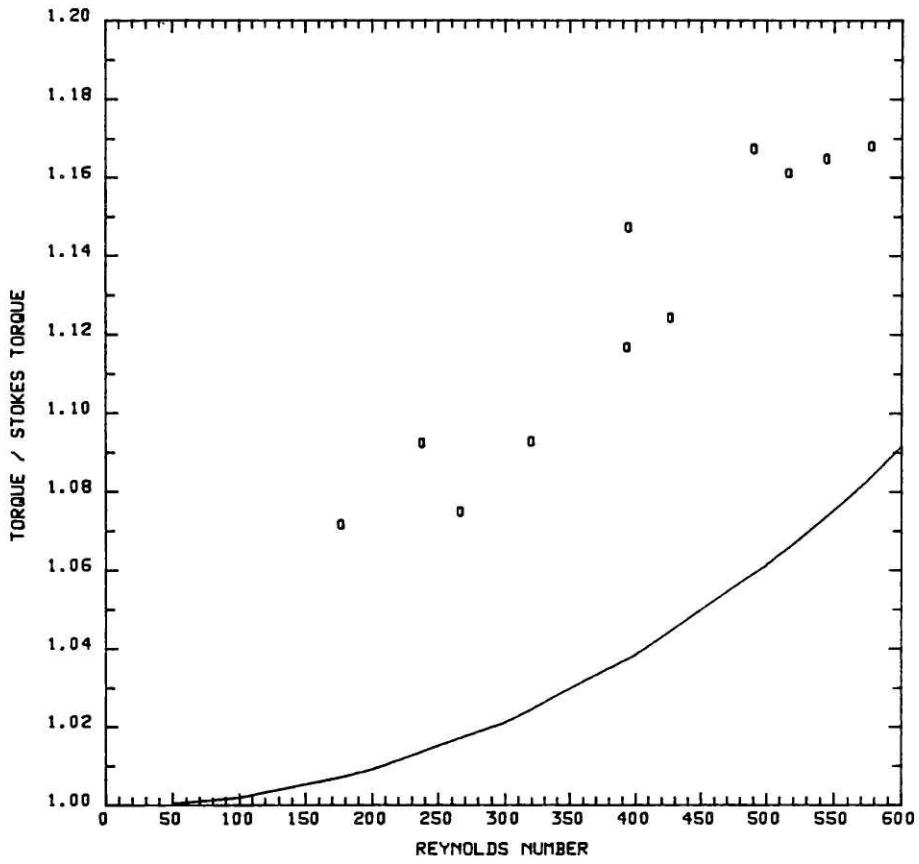


FIGURE 4.1

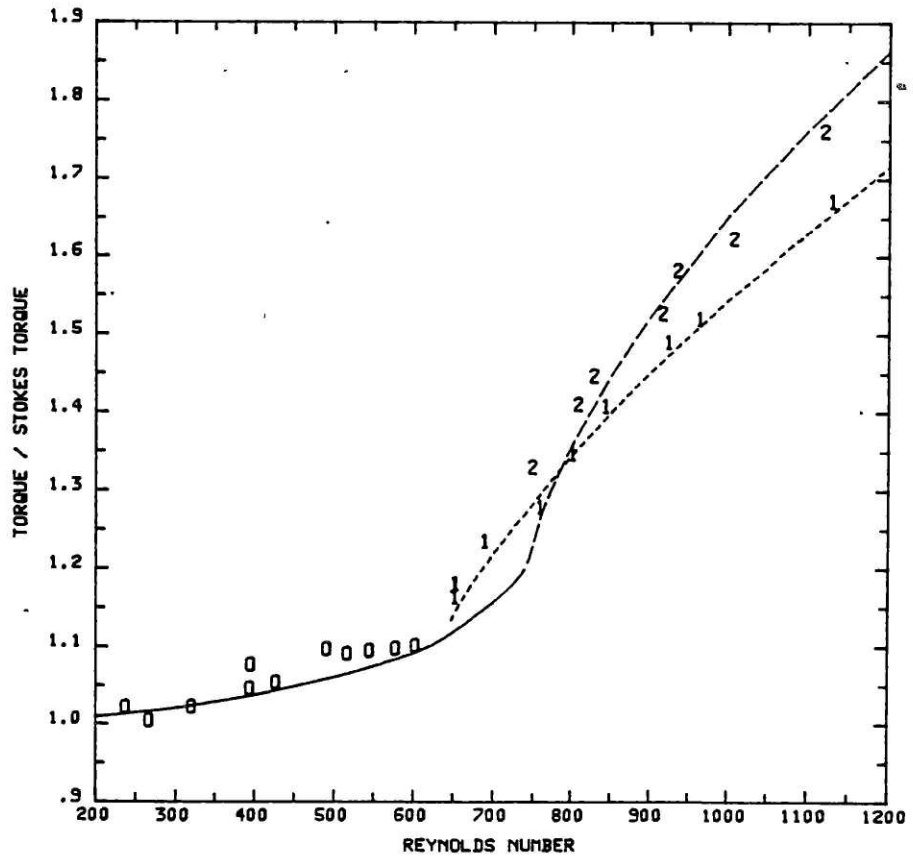


FIGURE 4.2

VORTEX BOUNDARIES

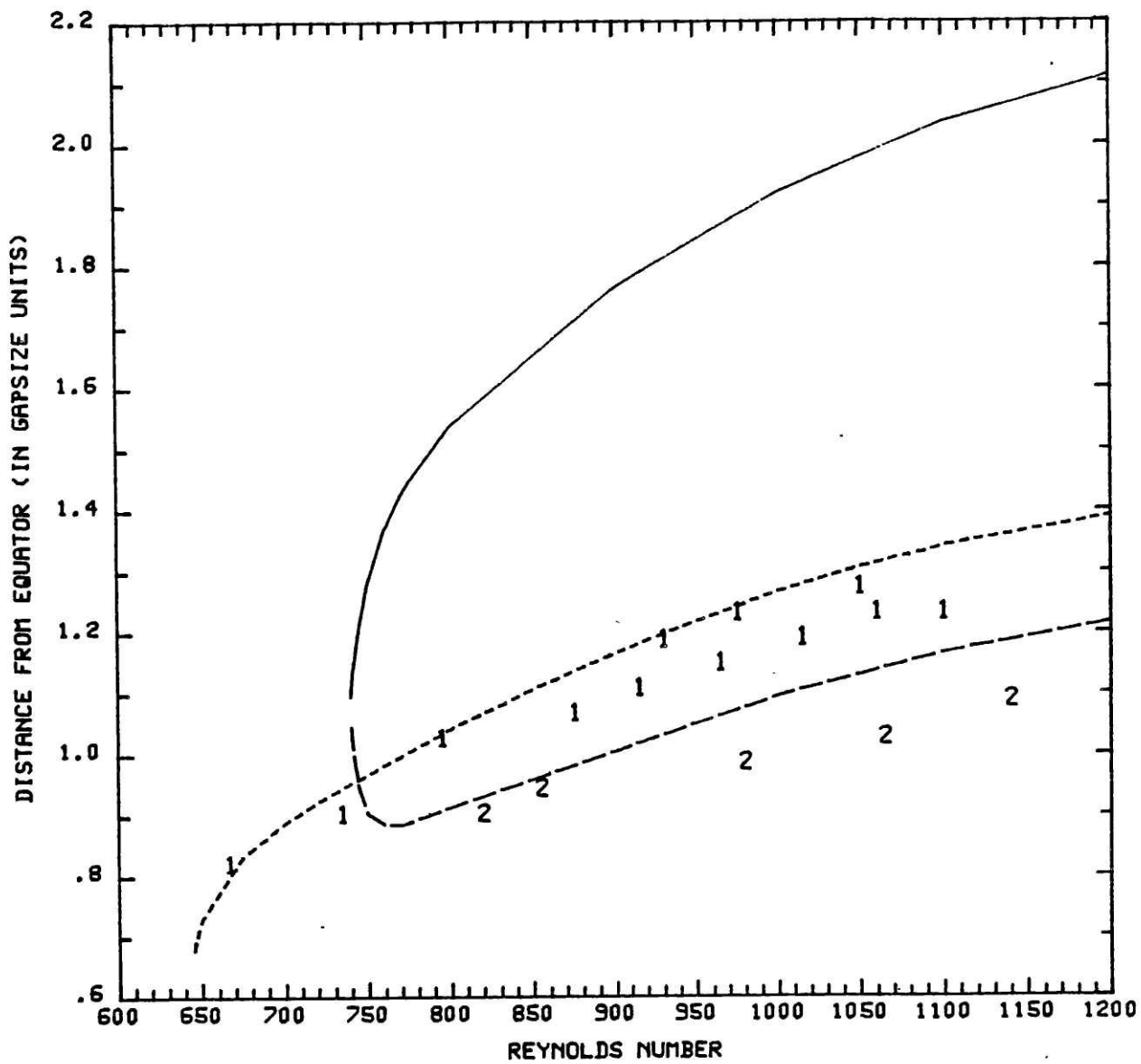


FIGURE 4.3

TABLE 4.1

AUTHOR	σ	STABILITY OF ONE	FORMATION OF ONE	STABILITY OF TWO	FORMATION OF TWO
<u>NUMERICAL</u>					
this study	0.18	49.2	49.8	56.5	56.5
Schrauf ¹	0.17647	48.4	----	~55.6	~55.6
Bartels ²	0.17647	50.9	----	55.6-59.3	55.6-59.3
Bonnet ³	0.17647	----	----	51.9-66.7	51.9-66.7
Astaf'eva ⁴	0.11	45.8	----	~48.3	~48.3
Sowarth ⁵	0.18	----	46.8	----	----
Walton ⁶	0.18	----	44.8	----	----
Yakushin ⁷	0.1	----	50.6	----	----
<u>EXPERIMENTAL</u>					
Wimmer ⁸	0.18	47.7-48.5	49.6-49.9	57.3-57.9	61.1-61.9
Buhler ⁹	0.154	~48.3	~48.3	~54.4	----
Yavorskaya ¹⁰	0.11	44.7±.6	44.7±.6	~47.8	~47.8
Munson ¹¹	0.135	----	~48.1	----	----
Khlebutin ¹²	0.19	----	44.7±1.6	----	----
	0.1225	----	53.6±3.8	----	----
	best fit	----	49.0	----	----
<u>REYNOLDS NUMBERS</u>					
this study	0.18	645	652	740	740
Wimmer ⁸	0.18	625-635.	650-653	750-758	800-810

Table 4.1 Critical Taylor numbers ($Ta \equiv Re\sigma^{\frac{3}{2}}$) for formation and stability of Taylor vortices in spherical Couette flow. Shown are the lowest values of Ta for which formation of the one-vortex state occurs, for which the one-vortex state is stable, for which formation of the two-vortex state occurs, and for which the two-vortex state is stable.

¹Schrauf 1983

²Bartels 1982

³Bonnet and Alziary de Roquefort 1976

⁴Astaf'eva, Vvedenskaya, and Yavorskaya 1978

⁵according to formula in Sowarth and Jones 1983

⁶according to formula in Walton 1978

⁷Yakushin 1969

⁸Wimmer, private communication

⁹Buhler, private communication

¹⁰Yavorskaya, Belyaev, and Monakhov 1977

¹¹Munson and Menguturk 1975

¹²Khlebutin 1969 included is his best fit to data from five gap sizes

TABLE 4.2

t'	t''	ΔA	$\int \dot{A} - \Delta A$	ratio	ΔE	$\int \dot{E} - \Delta E$	ratio
0	2	$-2. \times 10^{-4}$	$-4. \times 10^{-12}$	$2. \times 10^{-8}$	$-3. \times 10^{-3}$	$-9. \times 10^{-7}$	$3. \times 10^{-4}$
2	7	$9. \times 10^{-5}$	$-4. \times 10^{-11}$	$5. \times 10^{-7}$	$7. \times 10^{-4}$	$2. \times 10^{-7}$	$3. \times 10^{-4}$
7	27	$-1. \times 10^{-5}$	$-9. \times 10^{-11}$	$9. \times 10^{-6}$	$-9. \times 10^{-5}$	$-4. \times 10^{-8}$	$4. \times 10^{-4}$
27	80	$-2. \times 10^{-3}$	$-2. \times 10^{-10}$	$1. \times 10^{-7}$	$-1. \times 10^{-2}$	$3. \times 10^{-7}$	$3. \times 10^{-5}$

Table 4.2 Tests of conservation of angular momentum and energy. During each time interval $[t', t'']$, the exact solution satisfies $\Delta A = \int \dot{A}$ and $\Delta E = \int \dot{E}$. Data is taken from the numerical experiment described in section 6.3, in which a zero- to one- vortex transition occurred. ΔA is in units of $\pi R_1 \Omega_1$ while ΔE is in units of the Stokes energy.

PART II: DESCRIPTIVE RESULTS

5. DESCRIPTION OF FLOWS

In this chapter, we describe steady axisymmetric spherical Couette flows at various values of the Reynolds number $Re \equiv R_1^2 \Omega_1 / \nu$. As mentioned previously, the gap ratio used here and throughout the thesis is $\sigma \equiv (R_2 - R_1) / R_1 = 0.18$. The figures we will present are results of our numerical calculation as described in chapter 3.

5.1 Basic Flow

As stated previously, the azimuthal velocity of spherical Couette flow is the dominant component and is approximately equal to Stokes flow at low Reynolds number. The Stokes solution is

$$u_\phi = (\alpha r + \beta / r^2) \sin\theta \quad (5.1)$$

$$\text{where } \alpha \equiv \frac{-\Omega_1 R_1^3}{R_2^3 - R_1^3} \quad \text{and} \quad \beta \equiv \frac{R_1^3 R_2^3}{R_2^3 - R_1^3}$$

so that the angular velocity depends only on radius:

$$\frac{u_\phi}{r \sin\theta} = \alpha + \beta / r^3 \quad (5.2)$$

To understand the meridional motion, consider the flow near the poles, where the geometry resembles that between parallel differentially rotating disks. Ekman pumping causes fluid to be thrown outward centrifugally along the rotating disk (inner sphere) and pulled from the center of the stationary disk (outer sphere). The fluid moving down

from the north pole along the inner sphere meets fluid moving up from the south pole at the equator. The upward- and downward- moving streams join into an outward equatorial jet, called the equatorial outflow boundary. The jet divides at the outer sphere to flow in opposite directions towards the poles. Outflow boundaries are radial lines along which $u_\theta = 0$ and $u_r > 0$; analogously, inflow boundaries have $u_\theta = 0$ and $u_r < 0$. Inflow and outflow boundaries are clearly visible in laboratory visualization studies, since they can be observed from the surface of the outer sphere. The fluid in the northern and southern hemispheres does not mix. We shall henceforth refer to the large-scale meridional circulation in each hemisphere as a large basic vortex. The superposition of the azimuthal flow with the weaker meridional motion yields fluid paths which are spirals.

In an expansion of spherical Couette flow in Reynolds number, the lowest order term is Stokes flow (5.1), which is azimuthal. The first order correction u_m is meridional:

$$u_m \equiv \nabla \times (e_\phi f(r) \sin 2\theta) \quad (5.3)$$

where $f(r) = \sum c_n r^n$

The meridional velocity components are

$$u_r = -(f' + f/r) \sin 2\theta \quad u_\theta = f/r (3 \cos 2\theta + 1) \quad (5.4)$$

Figures 5.1a and 5.1b depict this basic three-dimensional flow at $Re = 600$. Both 5.1a and 5.1b are pro-

jections of the flow onto the r - θ plane at fixed ϕ . (Only one r - θ slice is necessary for all ϕ since the flow is axisymmetric.) In this chapter, the gap width is exaggerated for clarity of the features (the radial interval [1,1.18] is mapped linearly to [1,2]). The tick marks along the outer sphere are spaced so that the circumferential distance between tick marks is equal to one gap width, providing a guide to the scaling. The tick marks along the inner sphere are spaced at intervals of $\pi/16$ radians. The long pair of tick marks denote the equator.

Figure 5.1a shows the projected streamlines of the meridional flow. Streamlines whose circulation is positive (counter-clockwise) are solid contours and those whose circulation is negative (clockwise) are dashed contours. The streamfunction is antisymmetric in θ for an equatorially symmetric flow. The solid streamline at the equator is the outflow boundary between the two hemispheres of opposite circulation. The spacing between contour lines is only a qualitative guide to the magnitude of the meridional flow since, rather than spacing the contours at equal intervals of the stream function values, we have used a tanh mapping of the stream function, when necessary, to exaggerate weak features. Figure 5.1b shows the contours of constant angular velocity. Unlike the meridional streamlines, these lines are not tangent to the velocity. Instead they indicate the surfaces of equal magnitude of the angular velocity which decreases monotonically from the inner to the outer sphere.

Energy spectra convey useful information about a flow. We are interested in the θ dependence, so we decompose \mathbf{u} into vector spherical harmonics $\mathbf{Y}_{L,L+I,M}$ which, when multiplied by spherical Bessel functions of r , are eigenfunctions of the vector laplacian. Using the notation of Edmonds (1960) (see also Morse and Feshbach, 1953)

$$\mathbf{u}(r, \theta, \phi) = \sum_{L=0}^{\infty} \sum_{M=-L}^L \sum_{I=0,1} u_{L,L+I,M}(r) \mathbf{Y}_{L,L+I,M}(\theta, \phi) \quad (5.5)$$

For an axisymmetric flow field, the azimuthal velocity is

$$u_{\phi}(r, \theta) = \sum_L u_{L,L}(r) \mathbf{Y}_{L,L,0}(\theta) \quad (5.6)$$

and the meridional velocity is

$$u_m(r, \theta) = \sum_L u_{L,L+1}(r) \mathbf{Y}_{L,L+1,0}(\theta) \quad (5.7)$$

The energy can be decomposed into

$$E = E_{\phi} + E_m \quad (5.8)$$

where

$$E_{\phi} = \sum_L E_{\phi}(L) = \sum_L \int \frac{1}{2} u_{L,L}^2 \quad (5.9)$$

and

$$E_m = \sum_L E_m(L) = \sum_L \int \frac{1}{2} u_{L,L+1}^2 \quad (5.10)$$

The integrals are to be taken over $[R_1, R_2]$. There is no $L = 0$ component in a divergence-free velocity field with homogeneous normal boundary conditions.

For an equatorially symmetric flow, the sums in (5.6)

and (5.9) only contain terms with odd L , while the sums in (5.7) and (5.10) are over even L . Then, $E(L)$ arises exclusively from azimuthal flow if L is odd ($E(L) = E_{\phi}(L)$), from meridional flow if L is even ($E(L) = E_m(L)$). Since $E_{\phi}(L)$ and $E_m(L)$ differ in structure and magnitude, they are shown separately. The solid line in Figure 5.1c and all subsequent spectra is the azimuthal spectrum $E_{\phi}(L)$, the dashed line the meridional spectrum $E_m(L)$. The label "L symmetric" is to be interpreted as: for L odd, the value of $E(L)$ is to be found on the solid (azimuthal) curve, while for L even it is to be found on the dashed (meridional) curve. The spectrum of an equatorially antisymmetric state, where the situation is reversed, will bear the label "L antisymmetric", meaning that $E(L)$ is on the solid (azimuthal) curve for L even, and on the dashed (meridional) curve for L odd. We will not show "mixed spectra", those of an asymmetric flow, in which each $E(L)$ is a sum of azimuthal and meridional components.

Figure 5.1c shows the energy spectrum of the basic flow at $Re = 600$. The total energy has been non-dimensionalized by the energy of the Stokes flow, and the graph is logarithmic.

5.2 Pinches

As the Reynolds number is increased, the basic flow develops what Bonnet and Alziary de Roquefort (1976) called a pinching of streamlines. A pinch is characterized by

saddle point in the stream function, or equivalently, a stagnation point in the meridional projection of the velocity field. The stream function has two local maxima per hemisphere. Vortical motions occur near the equator. However, these are not Taylor vortices: their circulation is of the same sign as the large basic vortex and there is no inflow or outflow boundary separating the vortical motions from the rest of the basic flow. In a pinch, there is radial flow, but it does not extend to the surface of the sphere, so the pinch is not an obvious feature to a laboratory observer. We emphasize this distinction because of confusion in the published literature (cf., review article by Roesner, 1977).

We find that pinches occur for $Re \geq 630$, but that the development of pinches is not accompanied by large or abrupt changes in the dependence on Re of physical properties of the flow, such as the torque. The extent of each pinch is about one gap width from the equator. Figure 5.2a and 5.2b are pictures (analogous to 1a and b) of the basic flow at $Re = 650$ with pinches. Figure 5.2c is the spectrum of this flow, which has a local maximum at a wavenumber $L = 20$. This value of L corresponds to the length scale of the pinches, $L = 2\pi R_2 / 2(R_2 - R_1) = \pi R_2 / (R_2 - R_1) \approx 20$.

Hereafter, we will refer to the basic flow, with or without pinches, simply as a zero-vortex state. For $Re \geq 1200$, another stable axisymmetric state without Taylor vor-

tices exists, which we will not describe in this chapter. This state will always be referred to as the supercritical zero-vortex state, to distinguish it from the basic zero-vortex state.

5.3 Taylor vortices

We now consider the Taylor vortex flows occurring at $\sigma = 0.18$. Sawatzki and Zierep (1970) and Wimmer (1976) observed two axisymmetric, equatorially symmetric steady states with Taylor vortices: the one- and two-vortex states. Figure 5.3 shows the one-vortex state, which has one Taylor vortex in each hemisphere, at $Re = 900$. Figure 5.4 shows the two-vortex state, with two Taylor vortices per hemisphere, at the same $Re = 900$. It is not surprising that the Taylor vortices should be located near the equator, since it is only in the equatorial region that the geometry between concentric spheres resembles that between concentric cylinders. In addition, the local Reynolds number $Re(\theta) \equiv R_1^2 \Omega_1 \sin\theta / \nu$, which measures the local centrifugal force, is highest at the equator.

Looking at Figures 5.3a and 5.4a, we see that the size of the vortices is on the order of one gap width. Vortices meet without shearing, since the circulation alternates in sign. The straight radial contours are the inflow and outflow boundaries separating the Taylor vortices from each other and from the large basic vortices. Note that the equatorial boundary is outwards for the two-vortex state,

but inwards for the one-vortex state. The equatorial inflow boundary was seen and explained by Wimmer and Sawatzki and Zierep: If the large basic vortices are to retain their sign of circulation, there must be outflow boundaries between them and their neighboring Taylor vortices. This simple consideration yields the correct direction of the equatorial boundaries.

In Figures 5.3b and 5.4b, the distortion of the surfaces of constant angular velocity from spheres is quite noticeable, especially at the inflow and outflow boundaries. This demonstrates the advection of angular momentum by the Taylor vortices.

The spectra of the one- and two- vortex states are shown in Figures 5.3c and 5.4c. We see that the azimuthal energy continues to dominate the meridional energy. The spectra of the one- and two- vortex states have "scallop-shaped" shapes. This suggests a convolution of a Gaussian or similar function with the spectrum of a periodic function. Convolution of spectra corresponds to multiplication in physical space; the velocity field must be periodic with a modulated amplitude. We see then qualitatively that "scallop-shaped" spectra are to be expected from a velocity field with vortices located only at the equator.

We examine a one-dimensional model problem which gives rise to a scallop-shaped spectrum. Let $g(\theta)$ be the odd periodic extension of a Gaussian function centered at $\frac{\pi}{2}$.

$$g(\theta) \equiv \frac{1}{2a} \left[\frac{\pi}{2} \right]^{\frac{1}{2}} \sum_n (-1)^n \exp \left[- \frac{(\theta - \pi/2 - n\pi)^2}{2a^2} \right] \quad (5.11)$$

Its Fourier transform is

$$G(k) = \exp \left[- \frac{k^2 a^2}{2} \right] (-1)^{\frac{k-1}{2}} \quad , \quad k \text{ odd} \quad (5.12)$$

$$= 0 \quad , \quad k \text{ even}$$

Let

$$h(\theta) \equiv \sin(k_0 \theta) \quad (5.13)$$

The spectrum of the product $g(\theta) h(\theta)$ is the square of the convolution of $G(k)$ with $H(k) = \delta_{k, k_0}$

$$E(k) = \exp \left[- (k - k_0)^2 a^2 \right] \quad , \quad k - k_0 \text{ odd} \quad (5.14)$$

Now let h' be a more complicated periodic function with wavenumber k_0

$$h'(\theta) \equiv \sum_n \exp(-bnk_0) \sin(nk_0 \theta) \quad (5.14)$$

The spectrum of the product $g(\theta) h'(\theta)$ is

$$(5.15)$$

$$E'(k) = \sum_{n, m} \exp \left[- \frac{a^2}{2} ((k - nk_0)^2 + (k - mk_0)^2) - bk_0(n+m) \right]$$

(The sum is to be taken over n, m such that $k - nk_0$ and $k - mk_0$ are odd). If k_0 is large enough so that the points $k - nk_0$ are well separated, the spectrum is approximately

$$(5.16)$$

$$E'(k) = \sum_n \exp \left[- ((k - nk_0)^2 - 2bnk_0) \right] \quad , \quad k - nk_0 \text{ odd}$$

which has exponentially decreasing rounded maxima located at

$$k = nk_0 \quad (5.17)$$

and sharp minima at

$$k = \frac{k_0}{2} + \frac{b}{a} + nk_0 \quad (5.18)$$

Equation (5.16) has the qualitative form of the spectrum of the one-vortex state (Figure 5.3c). If k_0 is smaller, or if h is the sum of two periodic functions with different wavenumbers, more complicated spectra can occur. The two-vortex state (Figure 5.3d), for example, has a doubly-scalloped structure.

Figure Captions -- Chapter 5

- Figure 5.1 The basic flow at $Re = 600$. The gap width is exaggerated. Figure 5.1a shows the meridional streamlines. The solid and dashed streamlines denote positive and negative circulation, respectively. Figure 5.1b shows the contours of constant angular velocity. Figure 5.1c is the energy spectrum of the flow. The solid and dashed curves denote the azimuthal and meridional components, respectively.
- Figure 5.2 The basic state with pinch at $Re = 650$. Figures 5.2a, b, and c show the meridional streamlines, contours of constant angular velocity, and energy spectrum, as in Figure 5.1.
- Figure 5.3 The one-vortex state (one Taylor vortex in each hemisphere) at $Re = 900$. Figures 5.3a, b, and c show the meridional streamlines, contours of constant angular velocity, and energy spectrum, as in Figure 5.1.
- Figure 5.4 The two-vortex state (two Taylor vortices in each hemisphere) at $Re = 900$. Figures 5.4a, b, and c show the meridional streamlines, contours of constant angular velocity, and energy spectrum, as in Figure 5.1.

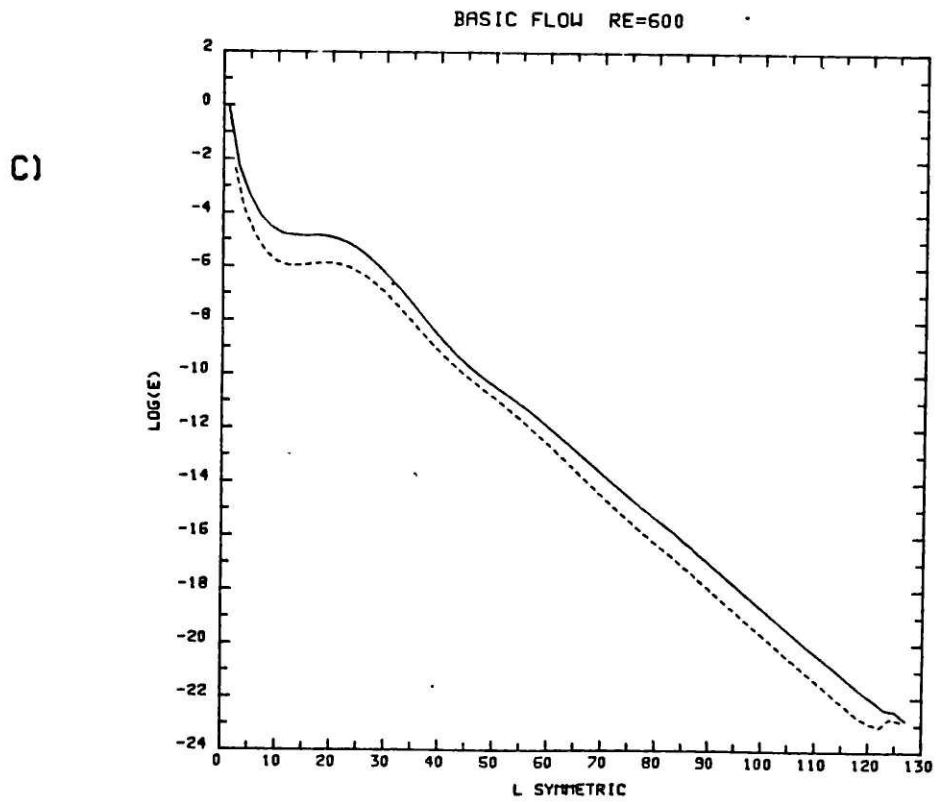
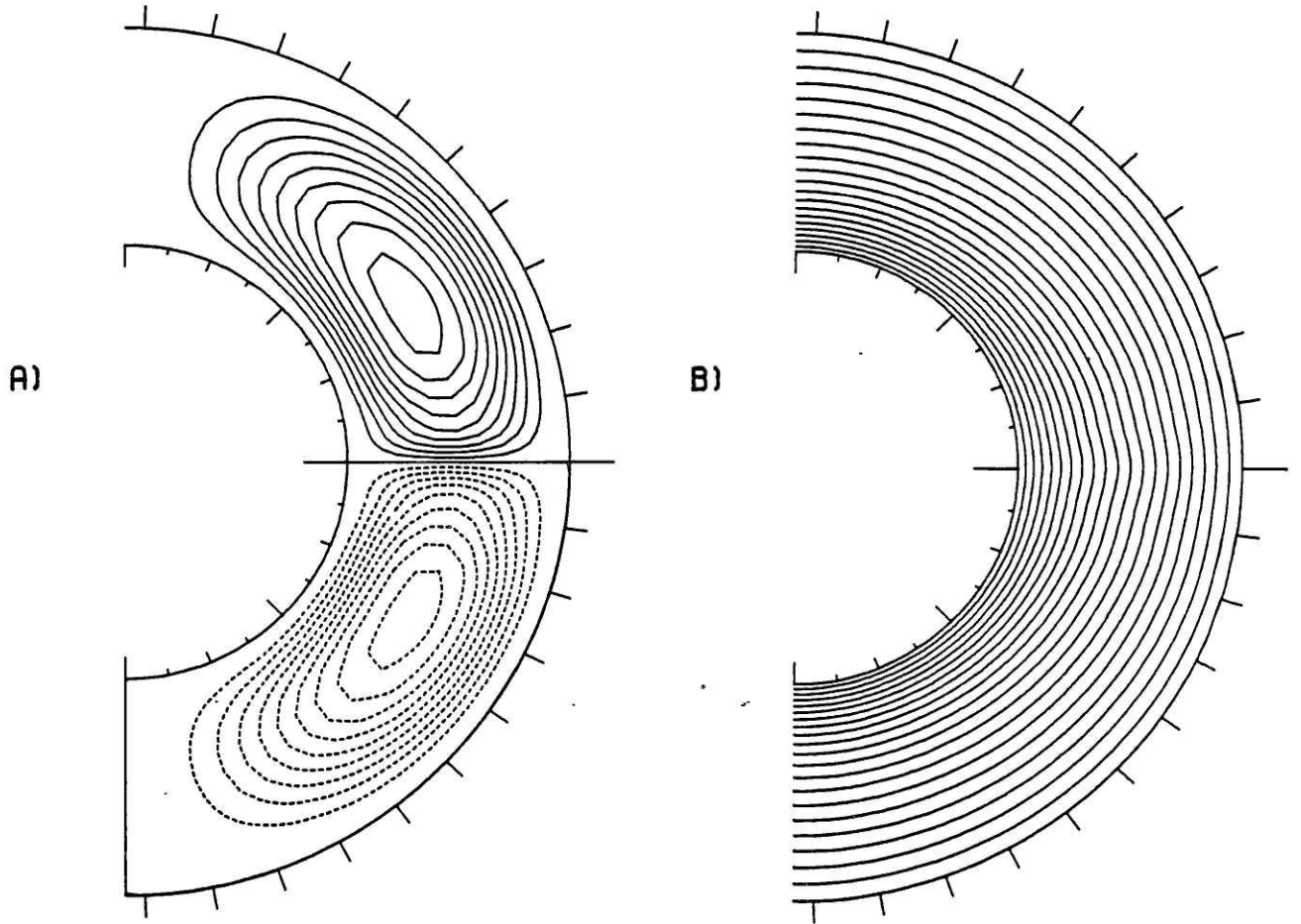
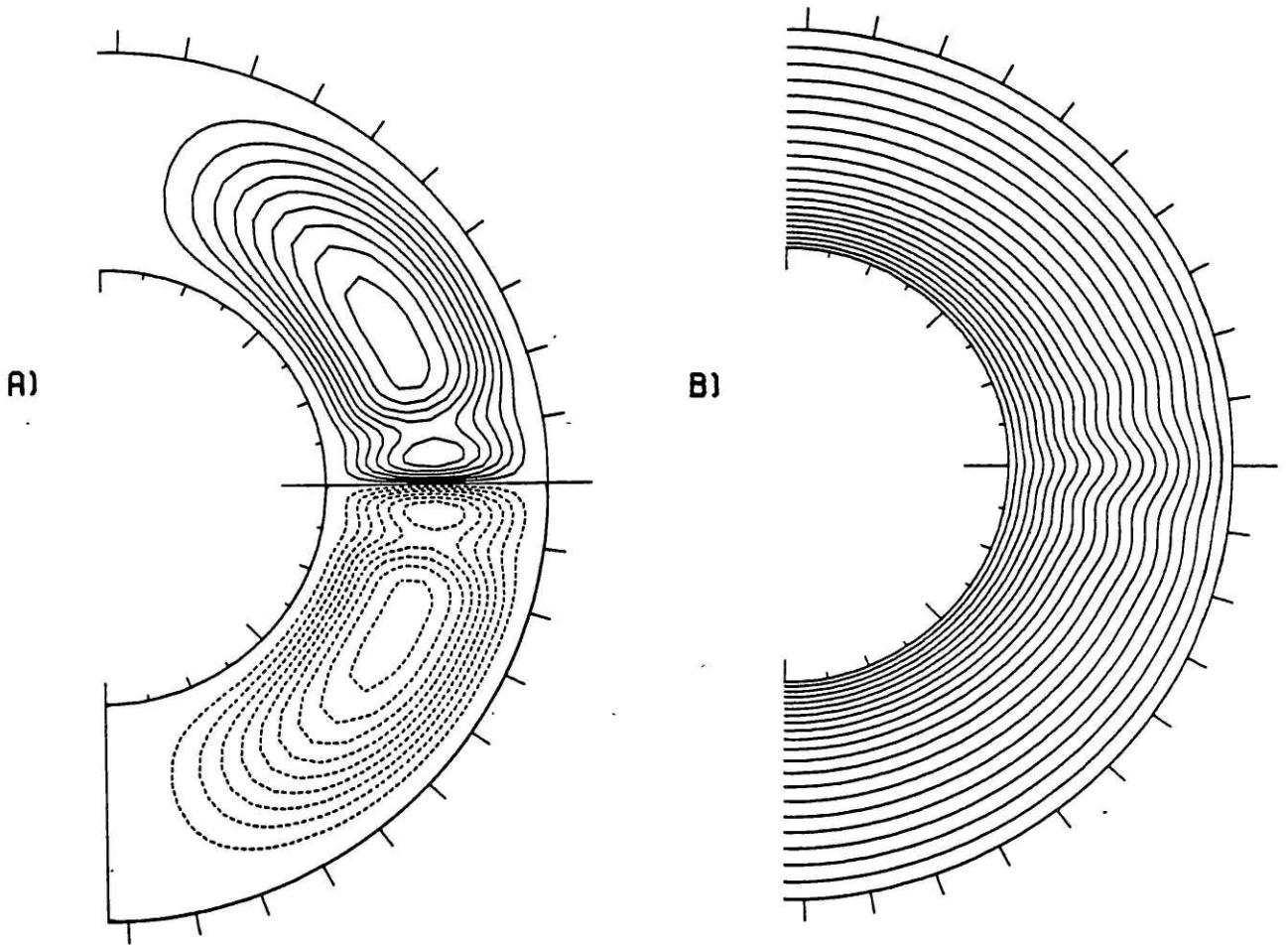


FIGURE 5.1



BASIC FLOW WITH PINCH RE=650

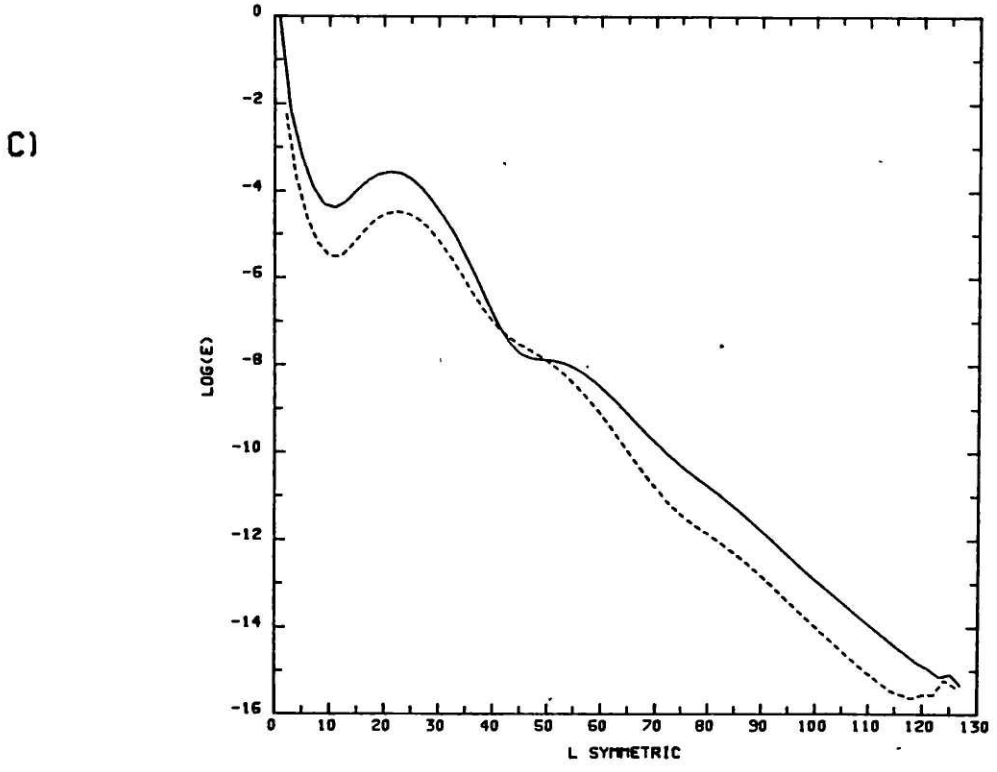


FIGURE 5.2

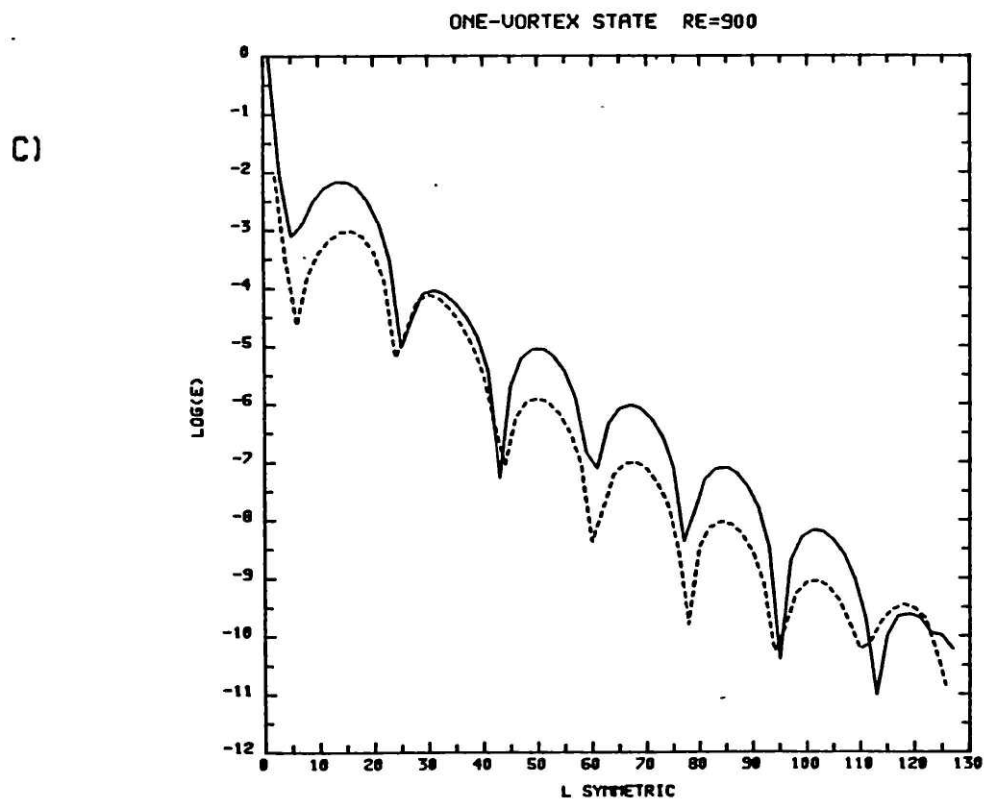
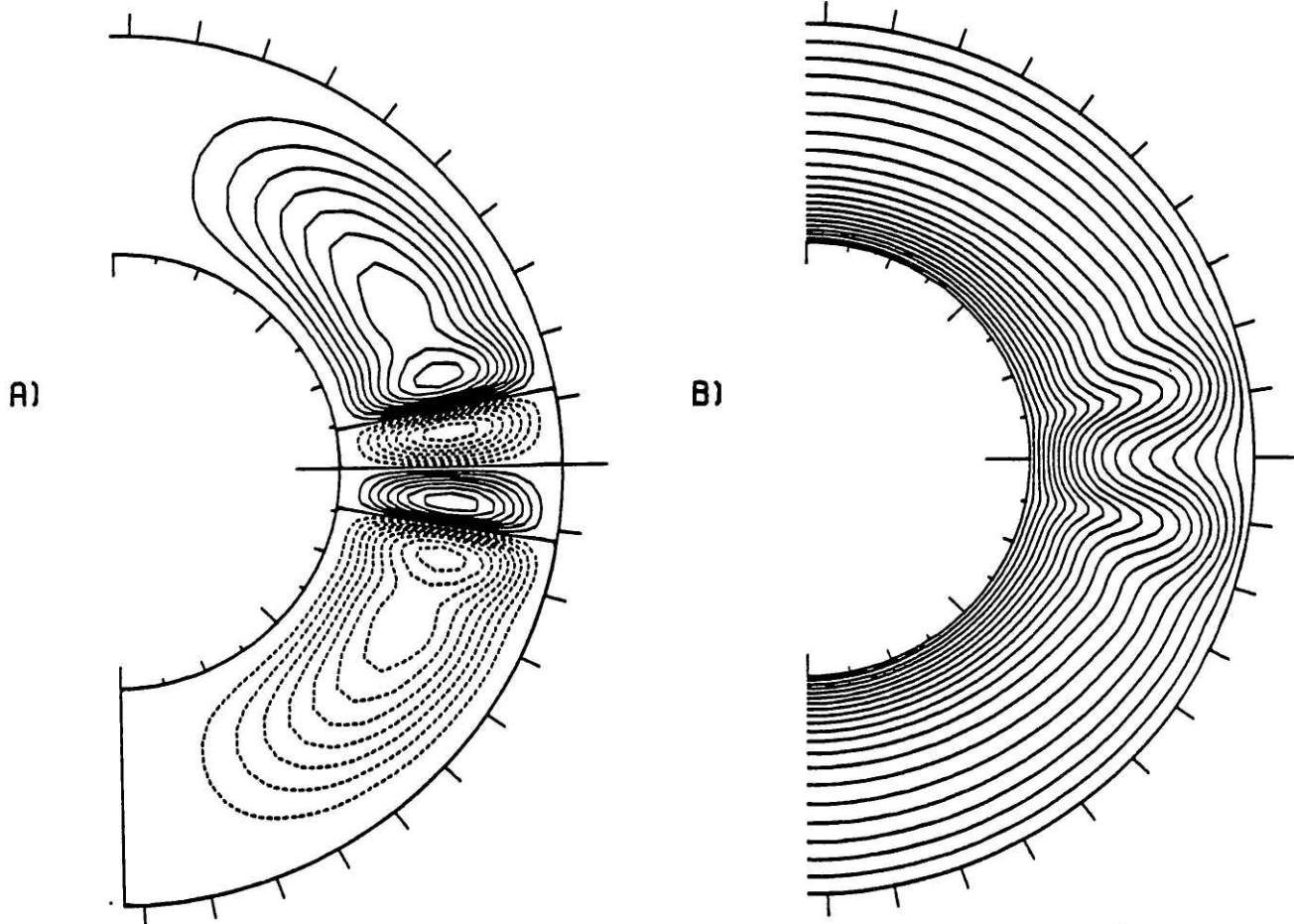
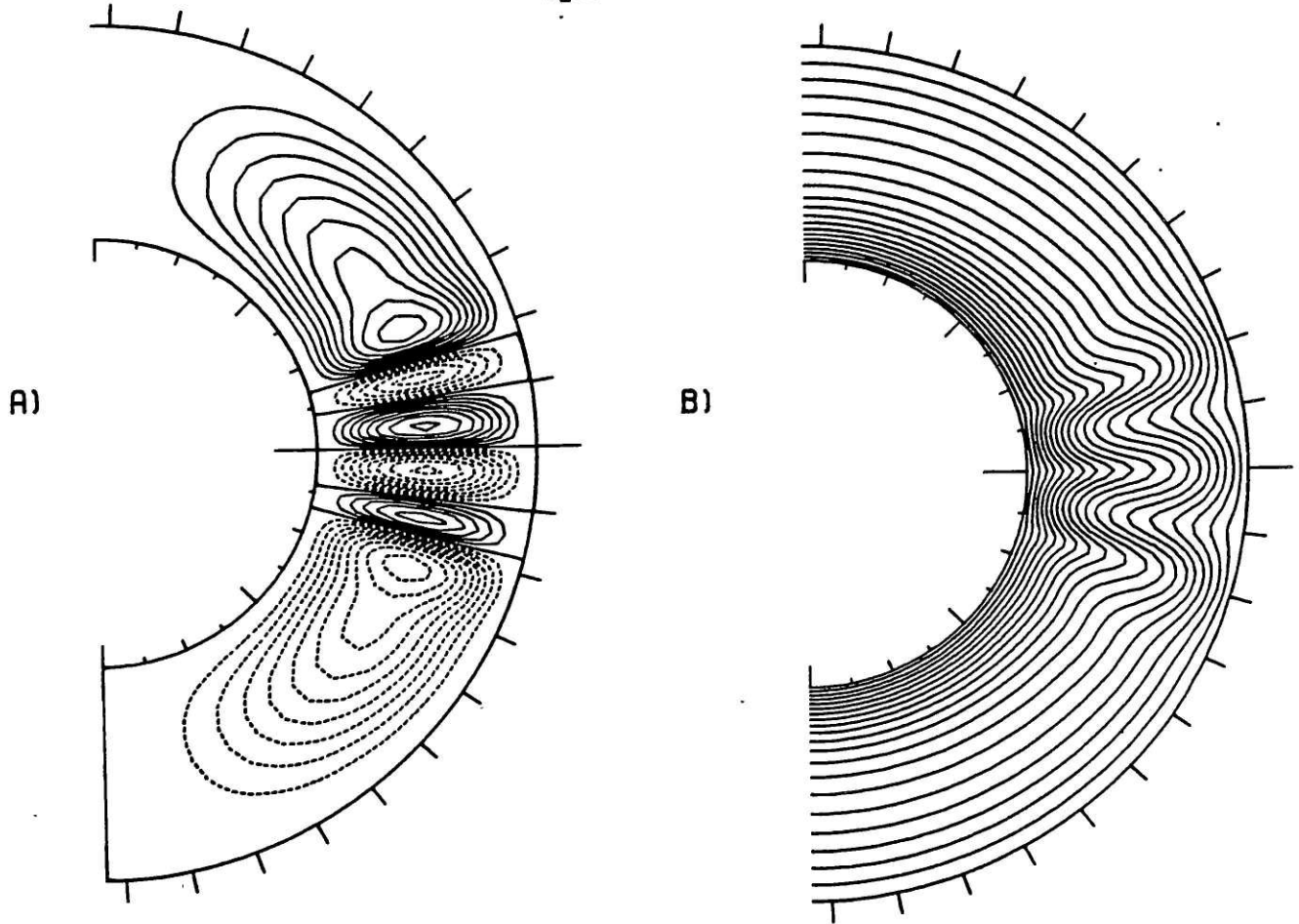


FIGURE 5.3



TWO-VORTEX STATE RE=900

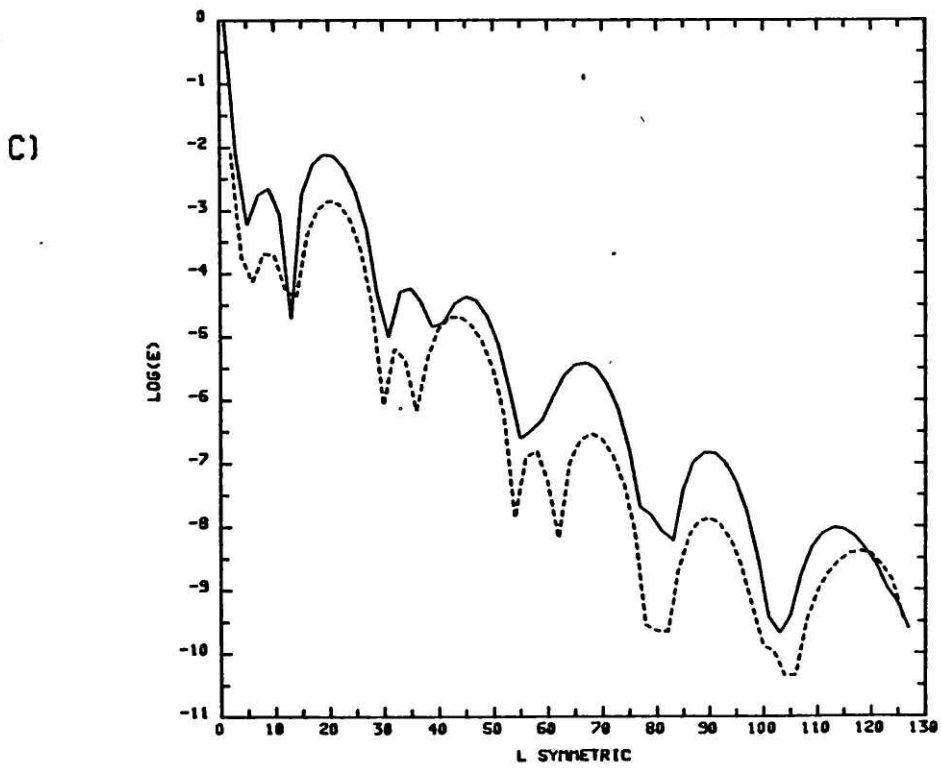


FIGURE 5.4

6. DESCRIPTIONS OF TRANSITIONS

Before analyzing the transitions physically and mathematically, it is important to describe them in detail. The equilibrium states have been described experimentally (Sawatzi and Zierep 1970, Wimmer 1976) and numerically (Bonnet and Alziary de Roquefort 1976; Bartels 1982; Schrauf 1983). However, the path by which one state changes into another has never been shown. Numerical results are a useful addition to experimental results in this regard, since the laboratory observer is restricted to viewing the outer sphere. Numerical simulations are also versatile, able to begin with either an unstable equilibrium (as is usual in analytic studies or non-equilibrium state (the usual case in experimental studies)).

In this chapter, we will show pictures of the time development of four types of transitions. These are: the zero- to two-, the one- to zero-, the zero- to one-, and the two- to one- vortex transitions. The first two have been reproduced numerically, while the third has not previously been simulated. We will see that there are a number of conceptual problems associated with the zero- to one- vortex transition, and we will show how these are resolved. The two- to one- vortex transition has until recently (Buhler, private communication) escaped experimental notice. We will see that it has much in common with the zero- to one- vortex transition. The two- to zero- vortex transition is not dis-

cussed separately since it is merely the reverse of the zero- to two- vortex transition. A one- to two- vortex transition is known to occur experimentally (Wimmer 1976), but we have not numerically simulated it.

6.1 Zero- to two- vortex

The zero- to two- vortex transition is readily produced in the laboratory and has been previously simulated numerically (Bartels 1982, Bonnet and Alziary de Roquefort 1976) but its time development has not been described. We will describe the zero- to two- vortex transition that takes place at $Re = 800$ and $\sigma = 0.18$. In Figure 6.1, we show six snapshots of the meridional flow. To allow the picture to be drawn to scale, and display both sides of the equator, only the sector $\pi/2 \pm \pi/8$ of the arc is shown. The markers along the outer sphere are located at intervals of one gap width along the sphere. The markers along the inner sphere are at intervals of $\pi/64$ radians. Each is labelled by the time in revolutions of the inner sphere from the start of the run.

The flow executes a fluid mechanical version of the biological maxim "Ontogeny Recapitulates Phylogeny": its evolution in time resembles the succession of steady states with increasing Reynolds number. The initial state (not pictured) at $T = 0$ is the Stokes flow (not an equilibrium state). By $T = 1$, the large basic vortices have formed; the meridional flow has the qualitative features of equation

(5.4). At $T = 2$, pinches have begun to form because of the centrifugal forces at the equator.

By $T = 3$, the pinches have grown more prominent and stretched. As each pinch separates from its basic vortex, the flow becomes unstable to formation of recirculation vortices (see Taneda 1979 for general discussion of recirculation vortices). This is in fact what happens: By $T = 4$, each pinch has broken off from its large basic vortex and a new and very weak recirculating vortex has formed in the space between them. (The formation of recirculation vortices will also be discussed in section 6.3, since it occurs in the zero- to one- transition as well.) In the descriptions to follow, the term "recirculating vortex" will be used to mean any Taylor vortex whose circulation is opposite to the large basic vortex of its hemisphere.

The recirculating vortices have grown considerably in size and strength by $T = 5$. The flow is close to its steady state, attained by $T = 20$. The timescale for the transition is dynamical, not viscous, since it occurs in a few revolution times. It is a local phenomenon; the transition time is insufficient for information to propagate from the poles.

Figure 6.2 shows the same evolution in time of the radial velocity profile $u_r(\bar{R}, \theta)$ at the mid-shell $\bar{R} \equiv (R_1 + R_2)/2$. Each profile is labelled by the time, in revolutions, at which it occurs is given along the abscissa, and the distance from the equator is shown on the ordinate

in units of gap size (only the equatorial region is shown). Within each profile, distance along the abscissa also measures the magnitude of the velocity. All the profiles have the same scale, so the figure provides a quantitative comparison of the magnitude of the meridional flow at different times and locations. The maximum meridional velocity in the figure is $u_r(\text{max}) = .088$ in units of the maximum azimuthal velocity $R_1\Omega_1$. The local Re based on the gap width and $u_r(\text{max})$ is 12, about the Reynolds number at which recirculation vortices form in two dimensional flows. Note that radial velocity profiles do not distinguish qualitatively between vortices and pinches.

Figure 6.3 shows the integrated physical quantities τ_1 (the torque at the inner sphere) and $\dot{A} = \tau_1 - \tau_2$ (the time derivative of angular momentum) as a function of time. The torque τ_1 increases as the pinches and vortices form, redistributing angular momentum. Graphs showing the variation of τ_1 and \dot{A} with time are signatures of the different transitions; when the same transition takes place at a different Re, the graphs change quantitatively but not qualitatively.

6.2 One- to zero- vortex

The progression of this transition, shown in Figure 6.4, is straightforward. The initial condition is the steady one-vortex state at $Re = 645$. When the Reynolds number is lowered to 644, the recirculating equatorial vortices monotonically decrease in energy. The transition proceeds

almost imperceptibly until about $T = 50$. By $T = 70$, the equatorial vortices have become noticeably weaker and smaller. At $T = 76$, they have disappeared altogether. Pinches are then formed, and equilibrium reached by $T = 80$. The transition is slow; the time scale is viscously dominated.

Figure 6.5 makes especially clear the change at the equator from an inflow to an outflow boundary. At $T = 76$, when the vortices have disappeared but the pinches have not yet formed, there is an outflow boundary seen in Figure 6.4, but Figure 6.5 shows it to be very weak. The radial outflow increases as the pinch is formed. The maximum meridional velocity is .034. In Figure 6.6, we see the torque gradually decreasing as the recirculating vortex diminishes, reaching a minimum at $T = 76$. The pinch then forms, redistributing angular momentum and thereby increasing the torque.

6.3 Zero- to one- vortex

We begin by speculating on how the one-vortex state might be formed in light of the two transitions we have described so far. Suppose the pinch broke off to become a vortex, as in the zero- to two- vortex transition of Figure 6.1, but that this was not accompanied by the formation of a second recirculating vortex. Then the circulation of the vortex would have the wrong sign: recall that the circulation of a Taylor vortex must be opposite to that of a

neighboring Taylor vortex or large basic vortex. Transition to the one-vortex state cannot happen this way.

Suppose instead that the zero- to one- vortex transition was the reverse of the one- to zero- vortex transition. From Figure 6.4, we see that this would require the generation of a pair of vortices at the equator, which is a strong outflow boundary in the zero-vortex state. It has been noticed (Marcus 1983, Mullin 1982) that vortices separated by outflow boundaries are tightly bound. It is difficult to insert new pairs of vortices at an outflow boundary, which would separate the bound vortices (Mullin 1982).

In the preceding paragraphs, we have examined two possible scenarios for the zero- to one- vortex transition and rejected them both. The first -- breaking off a pinch without forming a recirculating vortex -- does not yield the one-vortex state as described in section 5.3. The second -- generation of a vortex pair at the equatorial outflow boundary -- is geometrically possible, but physically unlikely. How then does this transition occur? It has been conjectured that the zero- to one-vortex transition takes place either non-axisymmetrically or non-equatorially symmetrically (Yavorskaya et al. 1978, Bartels 1982), but neither possibility has been investigated.

In Figure 6.7 we show the evolution in time of the zero- to one- vortex transition at $Re = 700$. The initial state is the steady zero-vortex state at $Re = 650$. It is

necessary here to allude to the mechanism of the transition, to be explained in the next two chapters. This transition is caused by a linear instability of the zero-vortex state at $Re = 700$. The flow spends about 10 revolutions relaxing to the zero-vortex state at $Re = 700$, and another 20 revolutions changing imperceptibly, as the initially infinitesimal perturbation grows to threshold value. The actual transition, starting at about $T = 30$, is insensitive to whether the initial condition is the stable $Re = 650$ or the unstable $Re = 700$ zero-vortex state.

Having explained this, we can say that the sequence in Figure 6.7 begins at $T = 30$ with the $Re = 700$ zero-vortex state. There is a large vortex and pinch in each hemisphere. The pinch in the northern hemisphere moves away from the large basic vortex and moves across the equator ($T = 37$). Two wedge-shaped recirculating zones form, one at each wall ($T = 39.4$). These meet ($T = 40$) to become the recirculating vortex of the northern hemisphere and separating the pinch from its basic vortex. This is the same process that occurs in the zero- to two-vortex transition, but here the pinch breaks off in only one hemisphere. The former pinch continues to move down ($T = 42$), eventually becoming the vortex associated with the southern hemisphere ($T = 70$). The re-establishment of symmetry is gradual.

The spontaneous breaking of symmetry is clearly seen in Figure 6.8 as the equatorial outflow boundary moves down,

and is eventually replaced by an inflow boundary. The maximum value of u_r in Figure 6.8 is .066 .

In Figure 6.9, the initial rapid increase and overshoot of τ_1 and \dot{A} are characteristic of an abrupt increase in Re of about this magnitude, rather than of the transition. The system then settles into the unstable $Re = 700$ zero-vortex equilibrium.

One consequence of the transition mechanism is that the amount of time spent by the numerically simulated flow in the unstable equilibrium is not physically meaningful. The time spent in the unstable state depends on the growth rate of the instability but also on its initial value. The initial value, in turn, depends on factors such as the numerical resolution and round-off error and is therefore non-physical. Numerical error-introducing processes are the analogues of experimental perturbations -- this is why an initial value code can function like an experiment in responding to instabilities -- but there is no reason to suppose the rate of introduction of perturbations to be the same. For calibration purposes only, we note that for $Re = 800$ when no asymmetric transitions are occurring, with our usual resolution of 16 radial Chebyshev coefficients and 128 angular Fourier coefficients, the energy of the antisymmetric part of the flow is about 10^{-24} of the total energy. This is the initial energy of the "infinitesimal" perturbation used by the simulation.

When the transition finally happens it is extremely rapid, accompanied by a sudden increase in $|\dot{A}|$. The inner torque τ_1 increases monotonically to its final value while the vortices are formed. It is relatively insensitive to the re-establishment of symmetry: angular momentum is transported by the vortices regardless of their position relative to the equator.

6.4 Two- to one- vortex

The two- to one- vortex transition, also asymmetric, has not received nearly as much attention as the zero- to one- vortex transition. In fact, it has never been mentioned in either the numerical or the published experimental literature, although it can be seen in Buhler's transition diagram (private communication). The absence of the two- to one- vortex transition in the numerical literature is easily explained by its asymmetry. The lack of mention in the experimental literature could be due to the fact that this transition occurs only in a very small range of Reynolds number $740 < Re < 775$.

Figure 6.10 shows the time evolution of the transition from a two-vortex state to the one-vortex state at $Re = 750$. We have started at $T = 0$ with the stable $Re = 800$ two-vortex state as an initial condition, and have abruptly decreased Re to 750. Much of what we have said about the zero- to one- vortex transition applies to the two- to one- vortex transition, also caused by a linear instability. That is,

the actual transition, starting at about $T = 50$, is unaffected by whether the initial condition is the one we have actually used -- the two-vortex state at $Re = 800$ -- or the two-vortex state at $Re = 750$, which is unstable.

At $T = 50$ in Figure 6.10 we show the unstable $Re = 750$ two-vortex state. Note that the recirculating vortices are narrow, their circumferential extent less than 40% of the gap width. As shown in Figure 4.3 and discussed by Wimmer (1976) and Yavorskaya (1977), the size of vortices is a function of Re . We may conjecture that the recirculation vortices at $Re = 750$ are unstable because their small size subjects them to shearing forces.

The recirculating vortex of the southern hemisphere grows smaller ($T = 57$) so that the large basic vortex and the equatorial vortex approach one another ($T = 58$). (The recirculating vortex still exists, but is represented by a blank area because it is too weak to contain a contour line.) Unlike those in steady states, the vortex boundaries are not radial lines. Eventually the recirculating vortex disappears altogether ($T = 60$), leaving the equatorial vortex to become a pinch associated with the large polar vortex. The recirculating vortex of the northern hemisphere expands ($T = 65$) and both vortices move across the equator till a symmetric configuration is re-established ($T = 90$).

Figure 6.11, very similar to Figure 6.8, reminds us that the radial velocity profiles do not distinguish between

the pinches of zero-vortex state and the recirculating vortices of the two-vortex state. The maximum value of u_r in Figure 6.11 is .078 . The asymmetry of the transition is clearly visible. We may speculate, in the same way as we did for the zero- to one- vortex transition, about how the transition could take place symmetrically. It would not suffice for the small recirculating vortices to disappear since then vortices of the same sign would be neighbors, therefore not Taylor vortices. The only remaining alternative would be for the vortices on either side of the equator to disappear. Again this seems physically unlikely, not only on the grounds of destroying an outflow boundary, but also because of the size and strength of the equatorial vortices.

Figure 6.12 shows that the change in τ_1 does not begin until after $T = 60$, indicating that the angular momentum transport is not greatly affected by the disappearance of the recirculating vortex of the southern hemisphere into a pinch. It is rather the increase in size of the recirculating vortex of the northern hemisphere that causes τ_1 to increase. The same disclaimer applies as was made for the zero- to one- vortex transition: the amount of time spent in the unstable two-vortex state has no physical significance.

Figure Captions -- Chapter 6

- Figure 6.1 Meridional flow during the zero- to two- vortex transition. Snapshots of the meridional flow, each labelled with the time in inner sphere revolutions. Only the sector $\pi/2 \pm \pi/8$ is shown.
- Figure 6.2 Radial velocity profiles during the zero- to two- vortex transition. $u_r((R_1+R_2)/2, \theta)$ as a function of θ (ordinate, units of one gap size) and as a function of time (abscissa, units of one inner sphere revolution). All profiles are scaled to the maximum meridional velocity during the transition, $u_r(\max) = .088 \Omega_1 R_1$.
- Figure 6.3 Torques during the zero- to two- vortex transition. The torque at the inner sphere, and the inner sphere torque minus the outer sphere torque are shown as a function of time.
- Figure 6.4 Meridional flow during the one- to zero- vortex transition.
- Figure 6.5 Radial velocity profiles during the one- to zero- vortex transition. $u_r(\max) = .034 \Omega_1 R_1$.
- Figure 6.6 Torques during the one- to zero- vortex transition.
- Figure 6.7 Meridional flow during the zero- to one- vortex transition.
- Figure 6.8 Radial velocity profiles for the zero- to one- vortex transition. $u_r(\max) = .066 \Omega_1 R_1$.
- Figure 6.9 Torques during the zero- to one- vortex transition.
- Figure 6.10 Meridional flow during the two- to one- vortex transition.
- Figure 6.11 Radial velocity profiles during the two- to one- vortex transition. $u_r(\max) = .078 \Omega_1 R_1$.
- Figure 6.12 Torques during the two- to one- vortex transition.

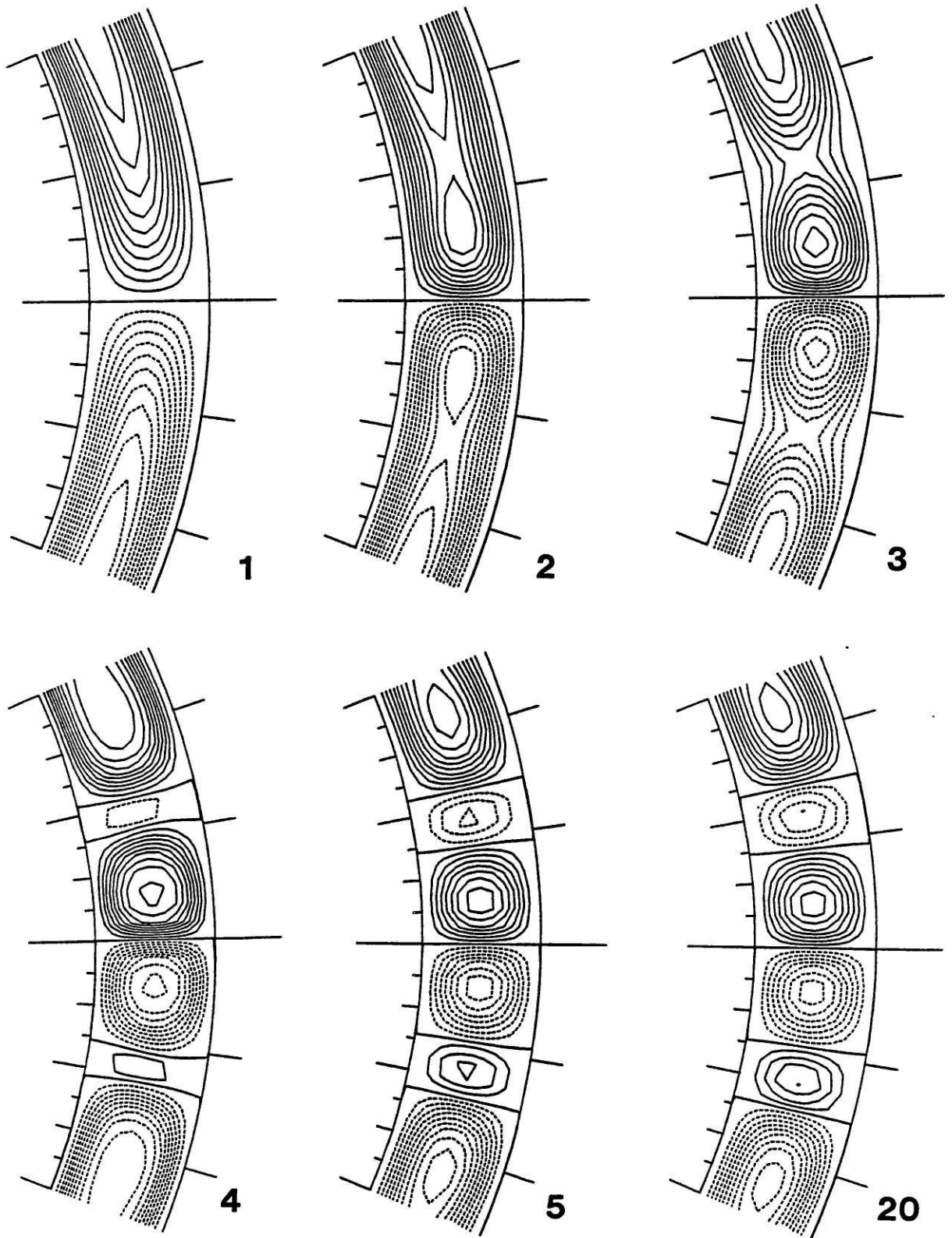


FIGURE 6.1

ZERO- TO TWO- VORTEX TRANSITION

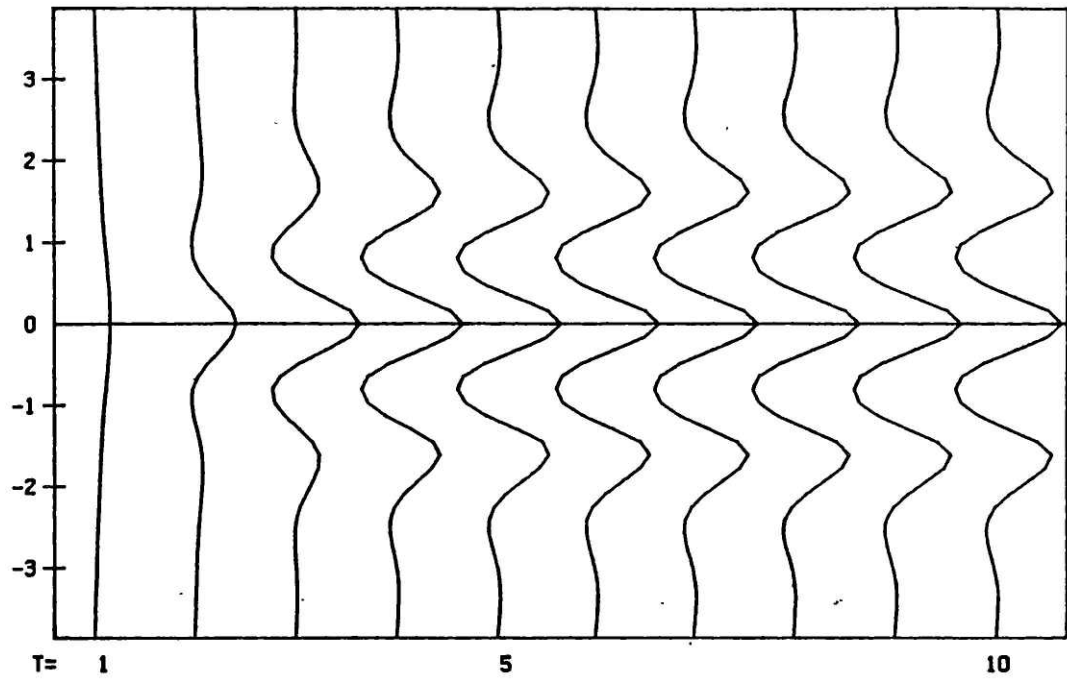


FIGURE 6.2

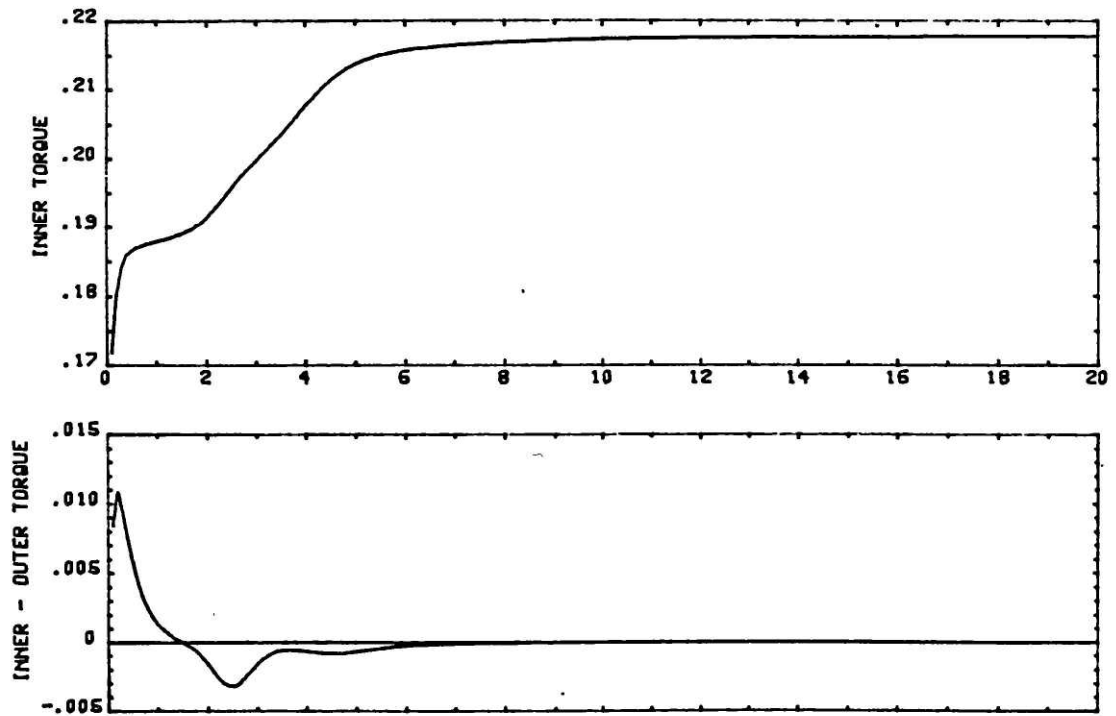


FIGURE 6.3

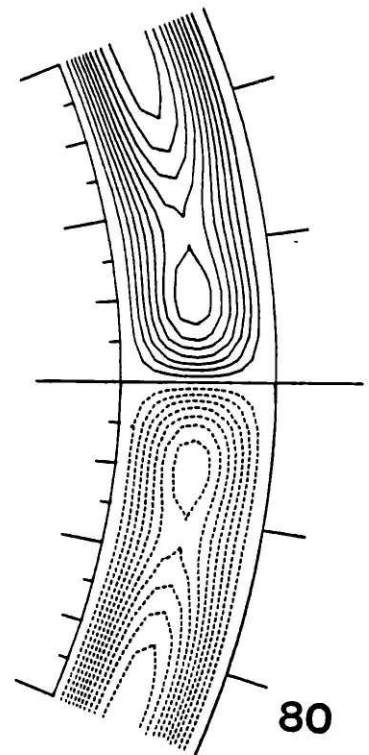
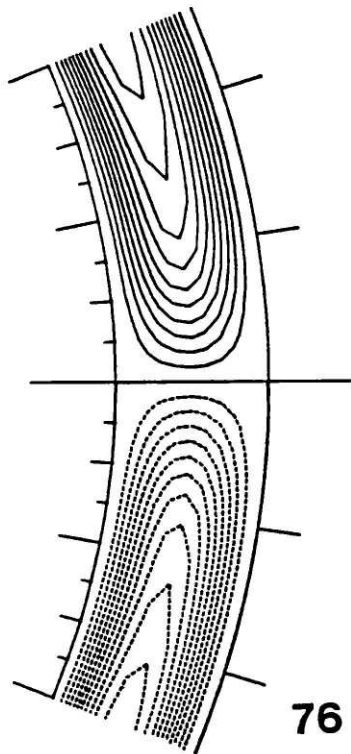
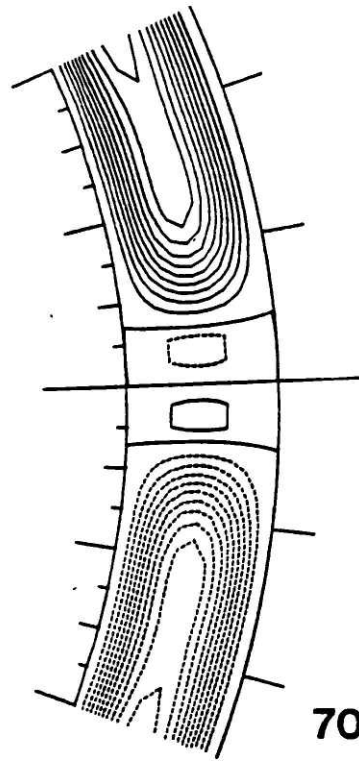
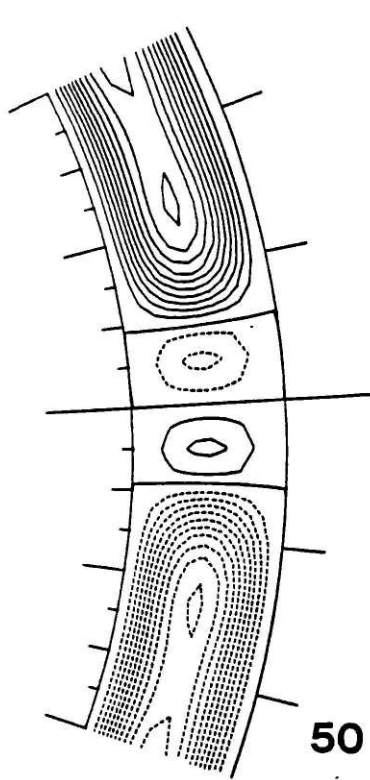


FIGURE 6.4

ONE- TO ZERO- VORTEX TRANSITION

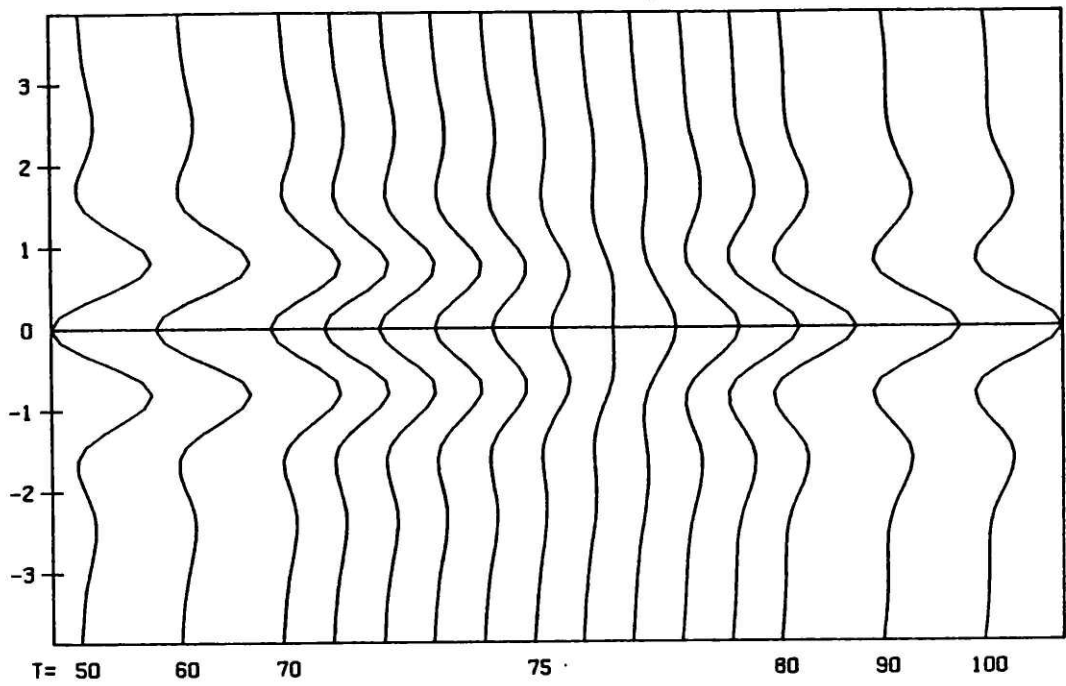


FIGURE 6.5

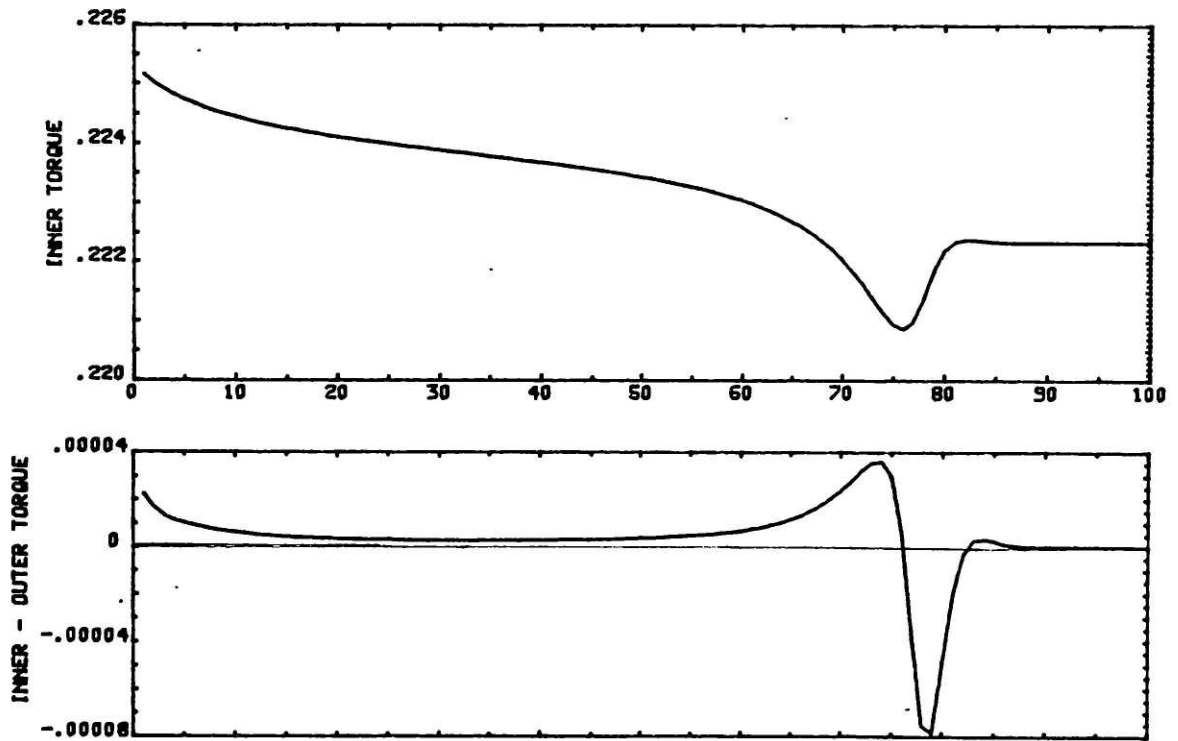


FIGURE 6.6

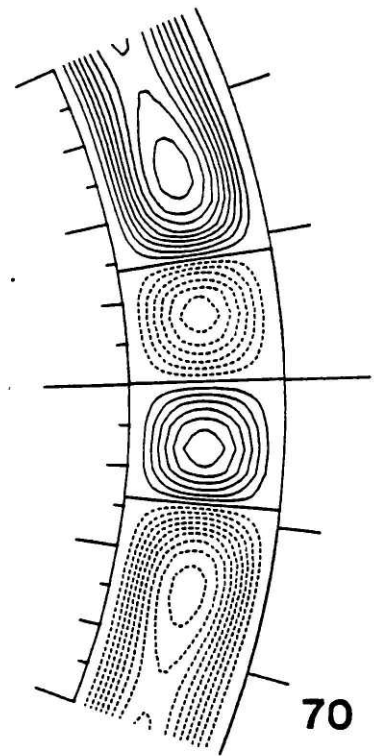
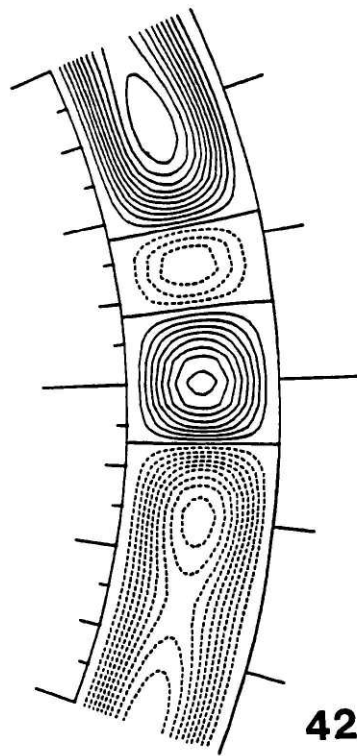
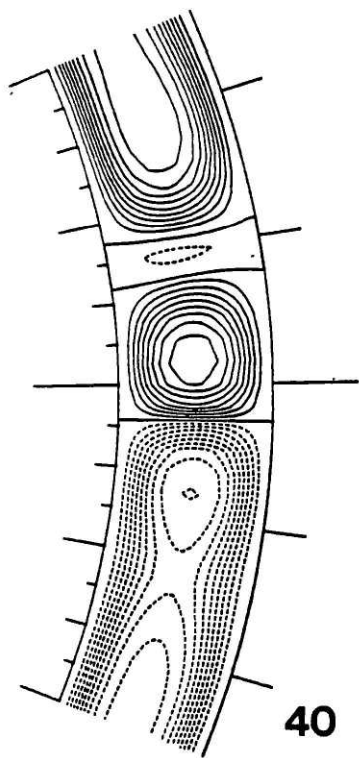
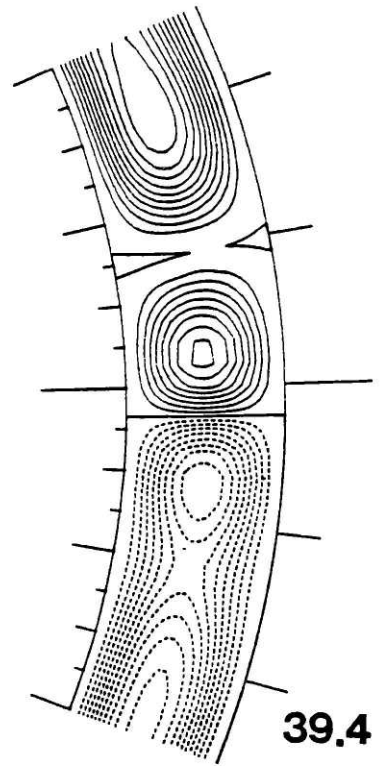
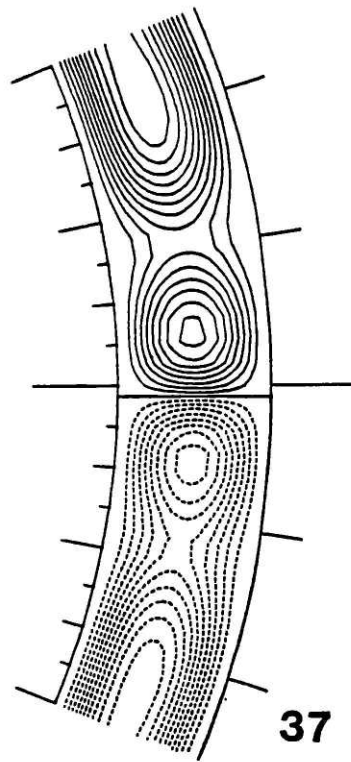
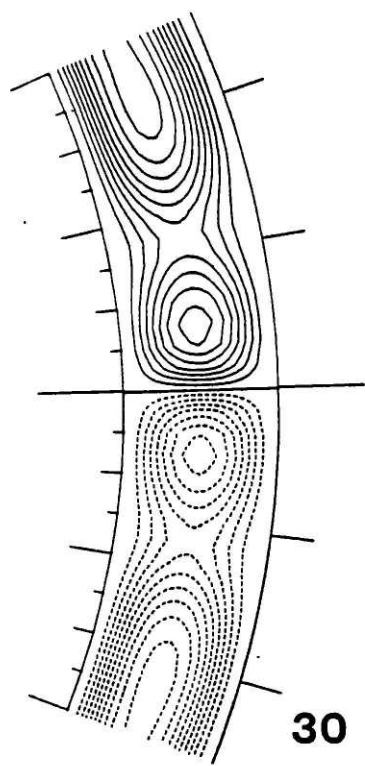


FIGURE 6.7

ZERO- TO ONE- VORTEX TRANSITION

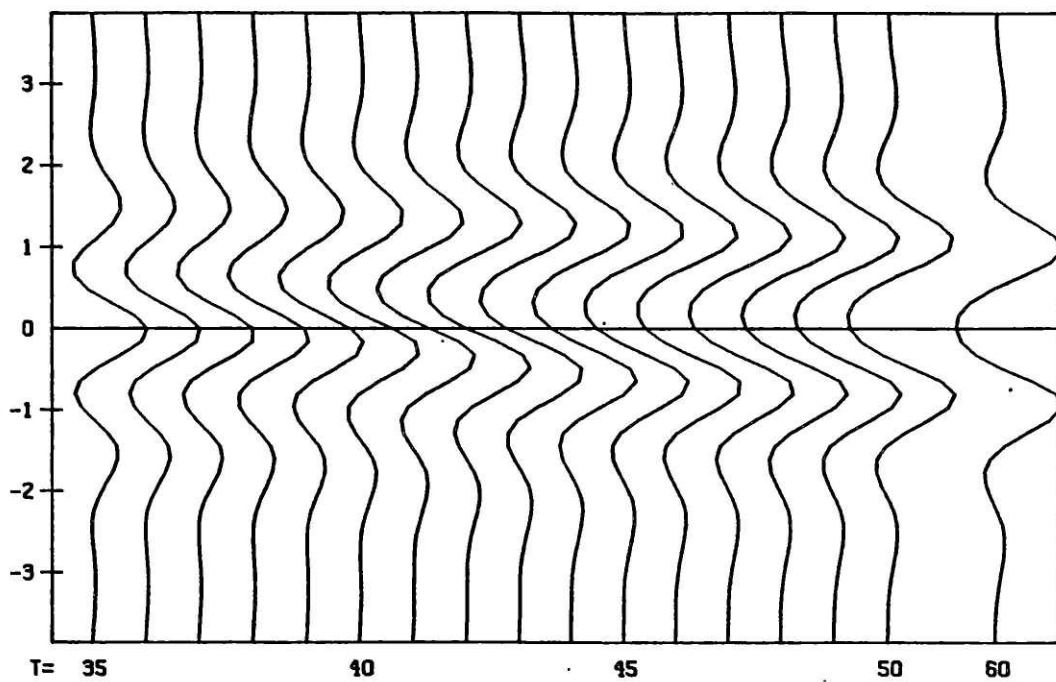


FIGURE 6.8

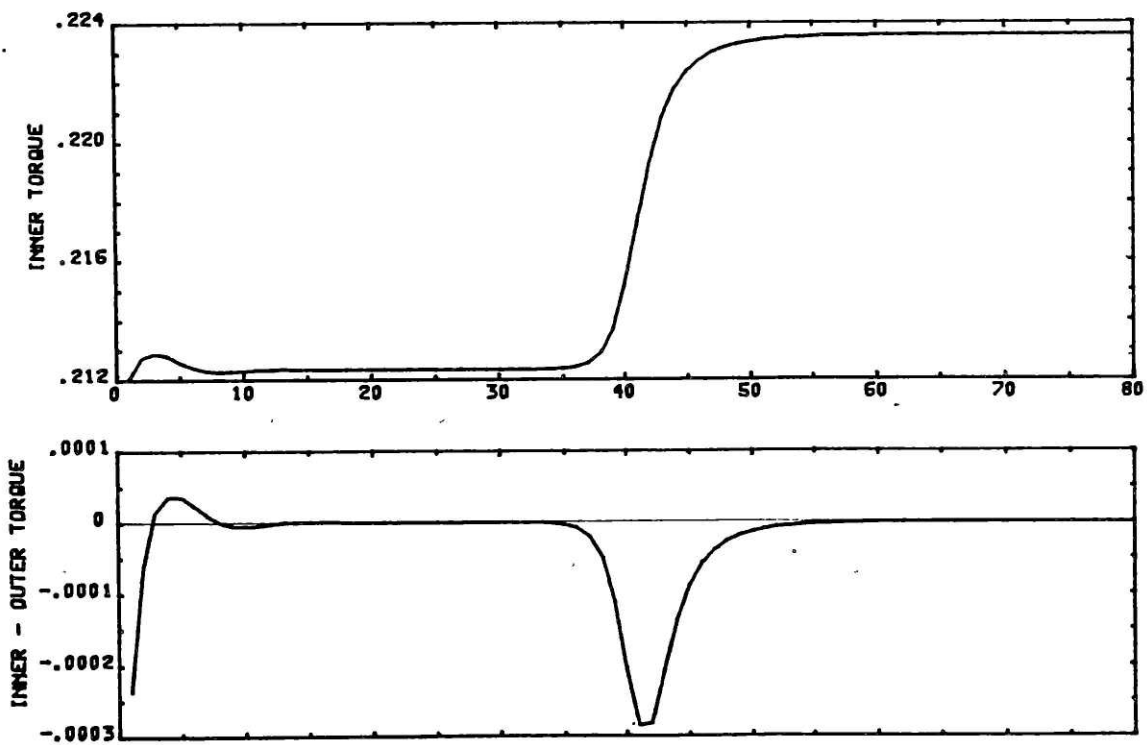


FIGURE 6.9

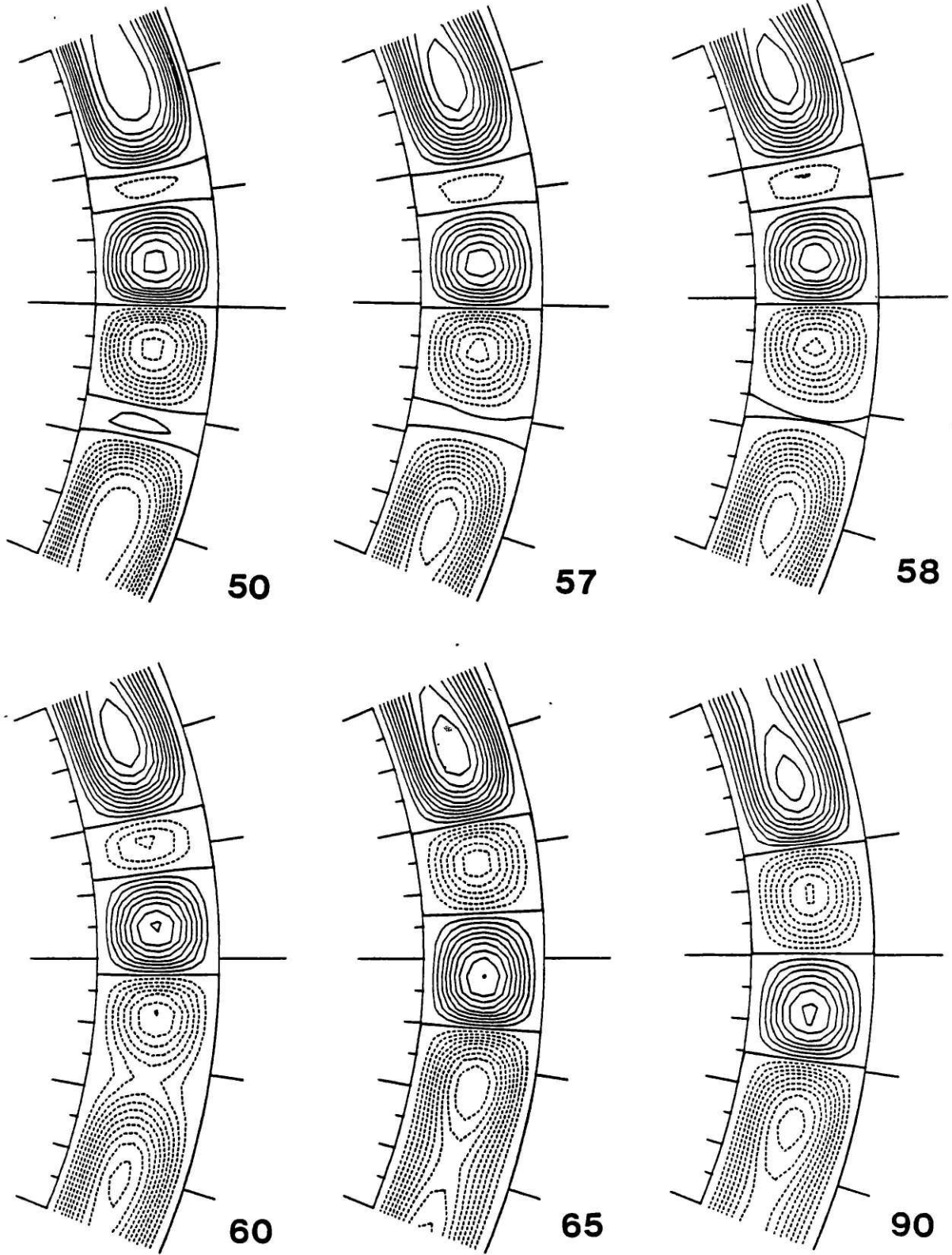


FIGURE 6.10

TWO- TO ONE- VORTEX TRANSITION

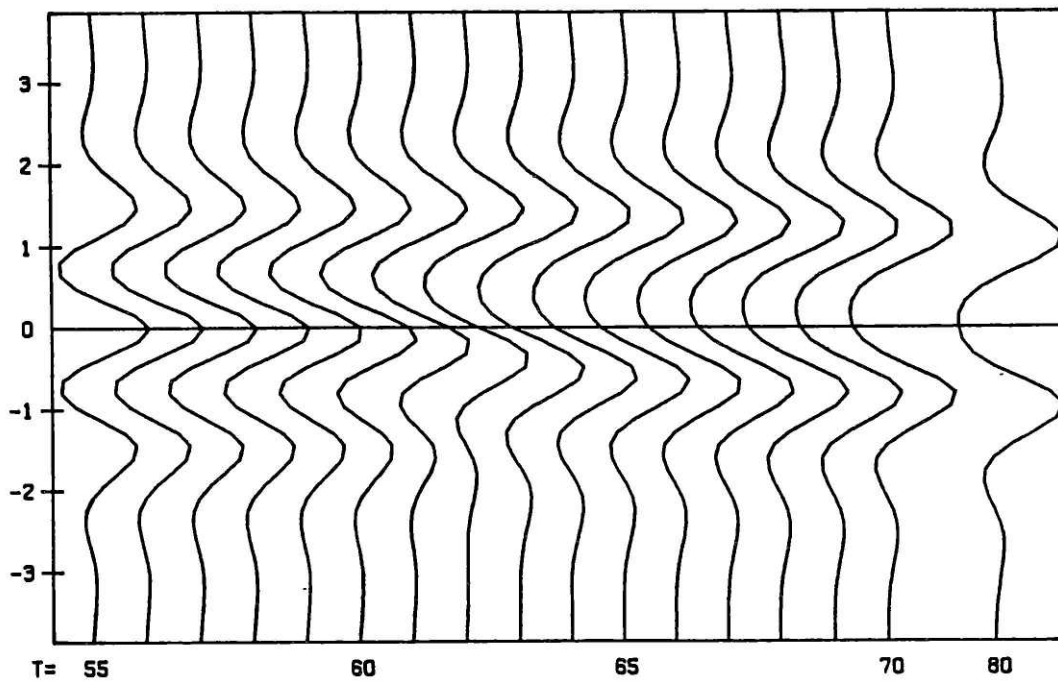


FIGURE 6.11

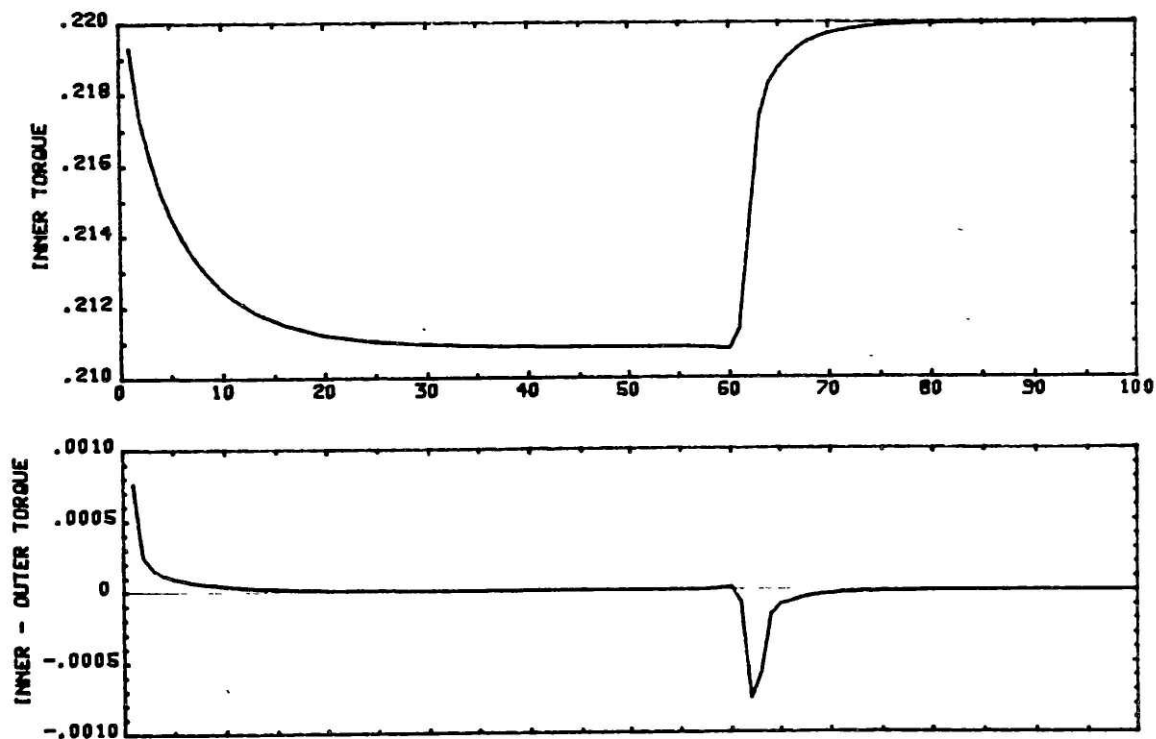


FIGURE 6.12

PART III: ANALYSIS OF RESULTS

7. STEADY STATES

7.1 Bifurcation diagram for spheres

Now that we have described the steady flows and the transitions between them, it is best to consider the global dependence of the steady flows on Reynolds number. Since it is impossible to present a graph of the infinite-dimensional flows as a function of Re , bifurcation diagrams are formed by projecting the flows onto some one-dimensional quantity. Schrauf (1983), who completed an extensive steady-state calculation of this problem, chose to represent each flow by its torque (non-dimensionalized by $\frac{1}{2}R_1^5\Omega_1^2$) τ .

Figure 7.1 is a graph of τ vs. Re for our numerically computed flows. All results to be presented in this chapter refer to steady flows. The torques of zero-vortex states are located on the solid curve, those of one-vortex states are on the short-dashed curve, and the two-vortex states are on the long-dashed curve. Except in regions of rapid change, flows were computed at intervals in Re of 10 or 25. The curve connects the calculated points without any smoothing. A striking feature, discovered independently by Schrauf and by our study, is that the zero-vortex states and two-vortex states lie on the same curve. We find $Re = 740$ as the value separating zero-vortex states from two-vortex states. We showed in Figure 4.3 that the recirculation vortices

(defined in the previous chapter as the Taylor vortices having circulation opposite to the hemisphere's basic vortex) are extremely small for Re near 740. As Re is increased, the recirculation vortices grow radically in size and intensity, thereby increasing the torque. Because of the rapid change near 740, flows were computed for seven values of Re in $730 \leq Re \leq 745$.

Schrauf discovered that the one-vortex states lie on a branch separate from that containing the zero- and two-vortex states. This result, clearly reproduced in Figure 7.1, elucidates some of the as-yet-unexplained phenomena in previous experiments and initial value calculations. We find $Re = 645$ as the lowest value of Re for which a steady one-vortex state exists.

The one-vortex branch and the zero- and two-vortex branch do not intersect, despite the coincidence of torques at $Re \approx 790$. We mean to distinguish here between a branch -- a set of flows, varying continuously with Re -- and the projection of a branch, onto the τ - Re plane in this case, which we have called a curve. The intersection of two curves does not imply an intersection in the two corresponding branches of flows, since intersections occur far more frequently in the projected space than in the infinite-dimensional space of flows. When schematic bifurcation diagrams are used, rather than physical quantities, they are drawn so that no such fortuitous intersections occur.

Figure 7.2 shows a section of τ vs. Re on a larger scale. The arrows in Figure 7.2 indicate schematically the transitions between branches. The arrows connect the initial and final states of three of the transitions described in the previous chapter. The one- to zero- vortex transition when Re is lowered from 645 to 644 occurs because the solution "falls off" the one-vortex branch when the branch ceases to exist. The zero- to one- vortex transition at $Re = 700$ and the two- to one- vortex transition at $Re = 750$ arise from an equatorially antisymmetric instability, to be discussed in the next chapter, of the branch containing the zero- and two- vortex states. Antisymmetric components were suppressed to enable the computation of unstable zero- and two- vortex equilibria. All three transitions are time-dependent processes, taking the flow through regions which are not steady solutions. The change from a zero- to a two-vortex state is not a transition in the same sense, since it does not involve moving from one solution branch to another.

7.2 Branches and turning points

To understand how Figure 7.1 fits into Schrauf's larger bifurcation diagram, we include here a mathematical digression on branches and bifurcations in the Navier-Stokes equations. Our sources, to which we refer the reader for proofs, details and more references, are the works of Joseph (1981), Sattinger (1973), and Benjamin (1976,1978a,1978b,1982). In

spherical and cylindrical Couette flow, as in many hydrodynamic problems, several different steady solutions exist at the same Reynolds number. At low Reynolds number, however, it is a general property of the steady Navier-Stokes equations that the solution is unique (Serrin 1959). The primary branch, in Benjamin's nomenclature, is the unique continuation of this low Re solution to high Re. Any other branch, called a secondary branch, must have a turning point (also called a one-sided bifurcation) below which it ceases to exist. Figure 7.3 is a schematic bifurcation diagram showing a primary branch (a), and a secondary branch (b) with a turning point (c). Turning points may occur elsewhere, for example on a primary branch (d), or at the high-Re limit of a branch (e).

A bifurcation point is the intersection of two branches. If a bifurcation coincides with a turning point of one of the two branches, it can be a sub-critical (f) or a super-critical (g) bifurcation. Sorokin (1961) and Benjamin (1976) showed that in the absence of exceptional symmetry, trans-critical bifurcations (h) (not coinciding with a turning point) are far more common. Perturbations of the equations or boundary conditions can lead to the decoupling of a bifurcation (i,j). The stability of a branch changes upon crossing either a bifurcation point or a turning point (see Joseph), although the stability may also change elsewhere (Sattinger). In 7.3(a)-(j), the solid lines denote stable branches, the dashed lines unstable branches, in

accordance with this rule.

One of the observable distinctions between the different types of bifurcations is the occurrence of hysteresis. At a super-critical bifurcation, there can be no hysteresis: in raising Re , transition from the primary to the secondary branch takes place because the primary flow becomes unstable, and in lowering Re , transition from the secondary to the primary branch occurs because the secondary branch ceases to exist at this point, which can unambiguously be called Re_c . At a sub-critical or trans-critical bifurcation, or when a bifurcation has been decoupled, the value of Re_c will depend on whether Re is increased or decreased.

The global structure of steady solutions is best determined by a steady-state solver, which traces the branches regardless of their stability. Solutions can be calculated which are not actually attained by evolution in time (unstable solutions in particular) and yet play an important mathematical role, much as the analytic continuation of real functions into the complex plane can yield important information about the original real functions. The role of an initial-value solver is complementary; it calculates the evolution in time of the flow along the steady branches, or from one branch to another, which a steady-state solver cannot do.

We can now apply these ideas to spherical Couette flow. The branch containing the zero- and two- vortex states is

the primary branch, which is the unique solution for $Re < 645$. The one-vortex states form a secondary branch. We have said that a secondary branch must terminate at a turning point linking it to the complementary unstable part of the branch. Although we cannot calculate unstable states, we can locate turning points since, as pointed out by Benjamin (1978a,b), measurements (i.e. projections of the flow) along the stable part of a branch should have a slope approaching the vertical as a turning point is approached. Although his discussion refers to experiment, it applies equally well to its numerical equivalent, an initial value solver. Indeed, the one-vortex curve in Figure 7.1 has a near-vertical tangent as Re decreases to 645. (Four points have been calculated in the interval $645 \leq Re \leq 650$.) The dependence of vortex size on Re in Figure 4.3 shows the same behavior.

To follow the secondary branch containing the one-vortex states past its turning point, we turn to Schrauf's study. His bifurcation diagram shows a complementary branch of unstable one-vortex states joining the stable one-vortex branch at the turning point. According to Schrauf, the secondary branch containing the one-vortex states never intersects the primary branch; there is no bifurcation point of any kind. Schrauf also found a plethora of turning points, and of other branches, stable and unstable, in addition to the ones we have described.

7.3 Relation to cylinders

The qualitative nature of these results is not entirely unexpected, in light of Benjamin's (1978a, 1978b, 1982) theoretical and experimental work on transition in finite cylinders. The classical mathematical model of cylindrical Couette flow, (Kirchgassner and Sorger 1968, Kogelman and DiPrima 1970) which is in very good agreement with experiments with long cylinders, assumes cylinders of infinite length. Transition to Taylor vortex flow takes place through a super-critical bifurcation, and no hysteresis should occur.

Benjamin argues that the finiteness of the cylinders has the effect of decoupling the bifurcation so that one branch of the Taylor-vortex solution is joined to the primary branch below Re_c and the other branch of the Taylor-vortex solution is joined to the unstable part of primary branch above Re_c . It is usual for a bifurcation to be decoupled by "imperfections", of which there are two in finite cylinders: the integer constraint posed by the finite length, and the Ekman pumping caused by the endplates. These effects are of course also present in spheres.

In Benjamin's model, transition to Taylor-vortex flow with the preferred number of vortices -- that yielding vortices closest to circular -- takes place continuously. Flows with one more pair or one fewer pair of vortices are located on a disconnected secondary branch. This is exactly what

happens in the spherical case, the two-vortex states being located on the primary branch and the one-vortex states occupying a secondary branch.

Figure Captions -- Chapter 7

Figure 7.1 The torques of steady states as a function of Reynolds number for $600 \leq Re \leq 900$. The solid curve shows torques of zero-vortex states, the short-dashed curve those of one-vortex states, and the short-dashed curve those of two-vortex states. Note that the curves representing zero- and two- vortex states join continuously, and that the one-vortex states are on a different, unconnected curve.

Figure 7.2 Same as Figure 7.1, for $620 \leq Re \leq 800$. The arrows at $Re = 644$, $Re = 700$, and $Re = 750$ show schematically the one- to zero-, zero- to one-, and two- to one- vortex transitions discussed in chapter 6.

Figure 7.3 Schematic bifurcation diagrams. Branches: primary (a) and secondary (b). Turning points (c,d,e). Bifurcations: sub-critical (f), super-critical (g), and transcritical (h). Decoupling of bifurcations (i,j).

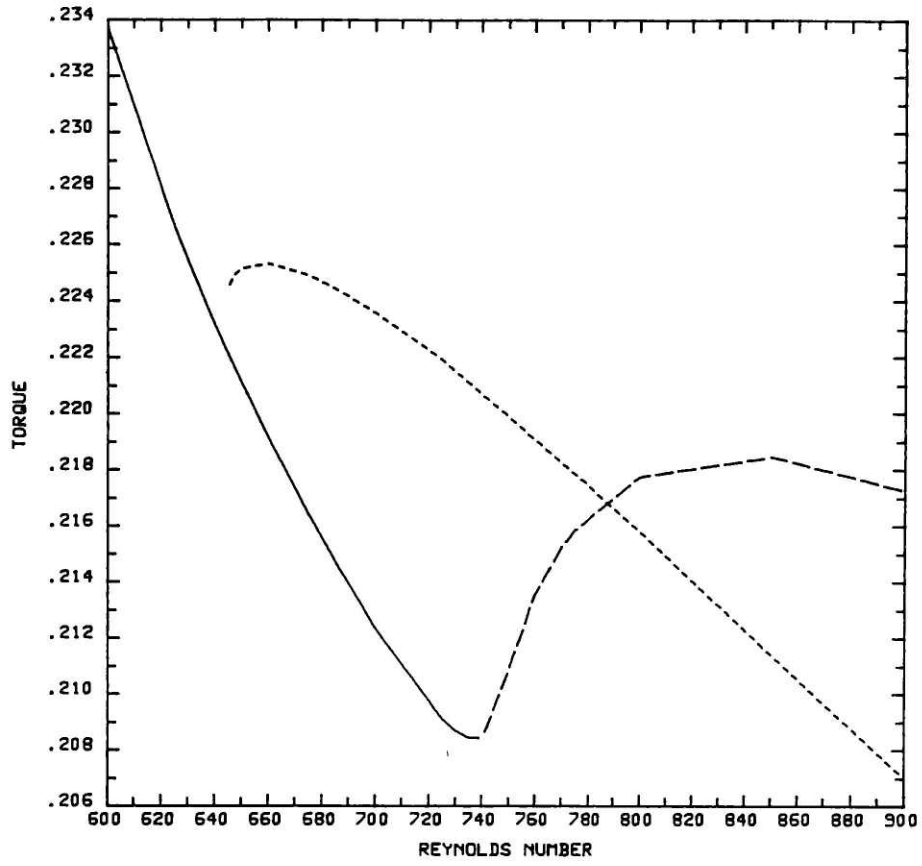


FIGURE 7.1

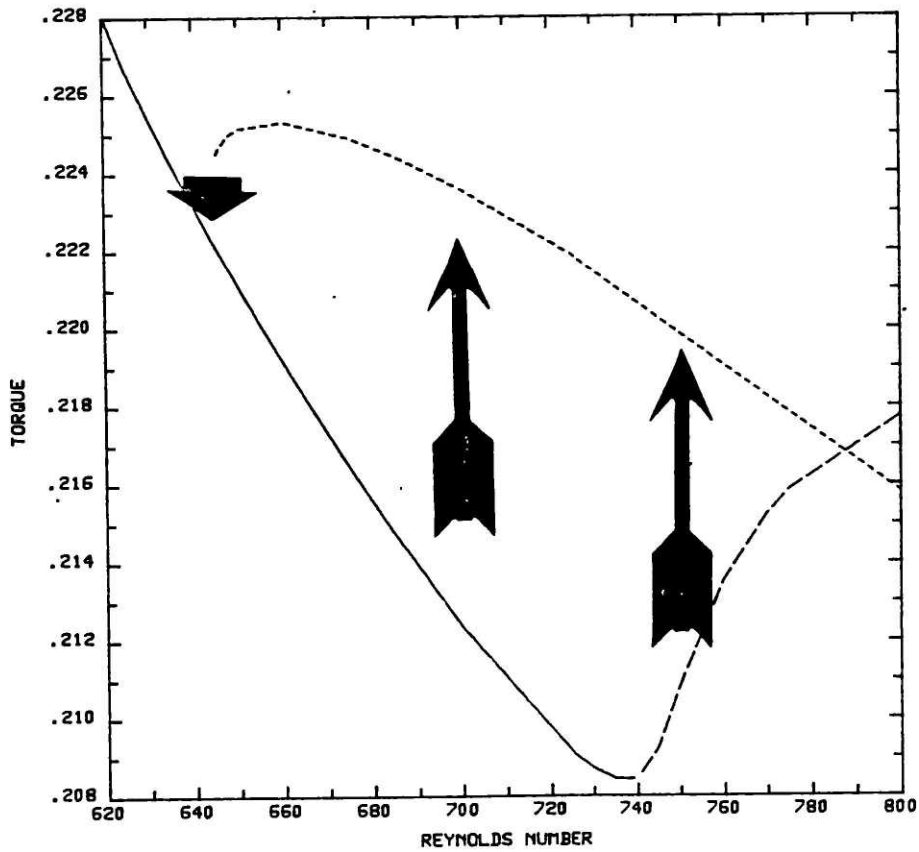


FIGURE 7.2

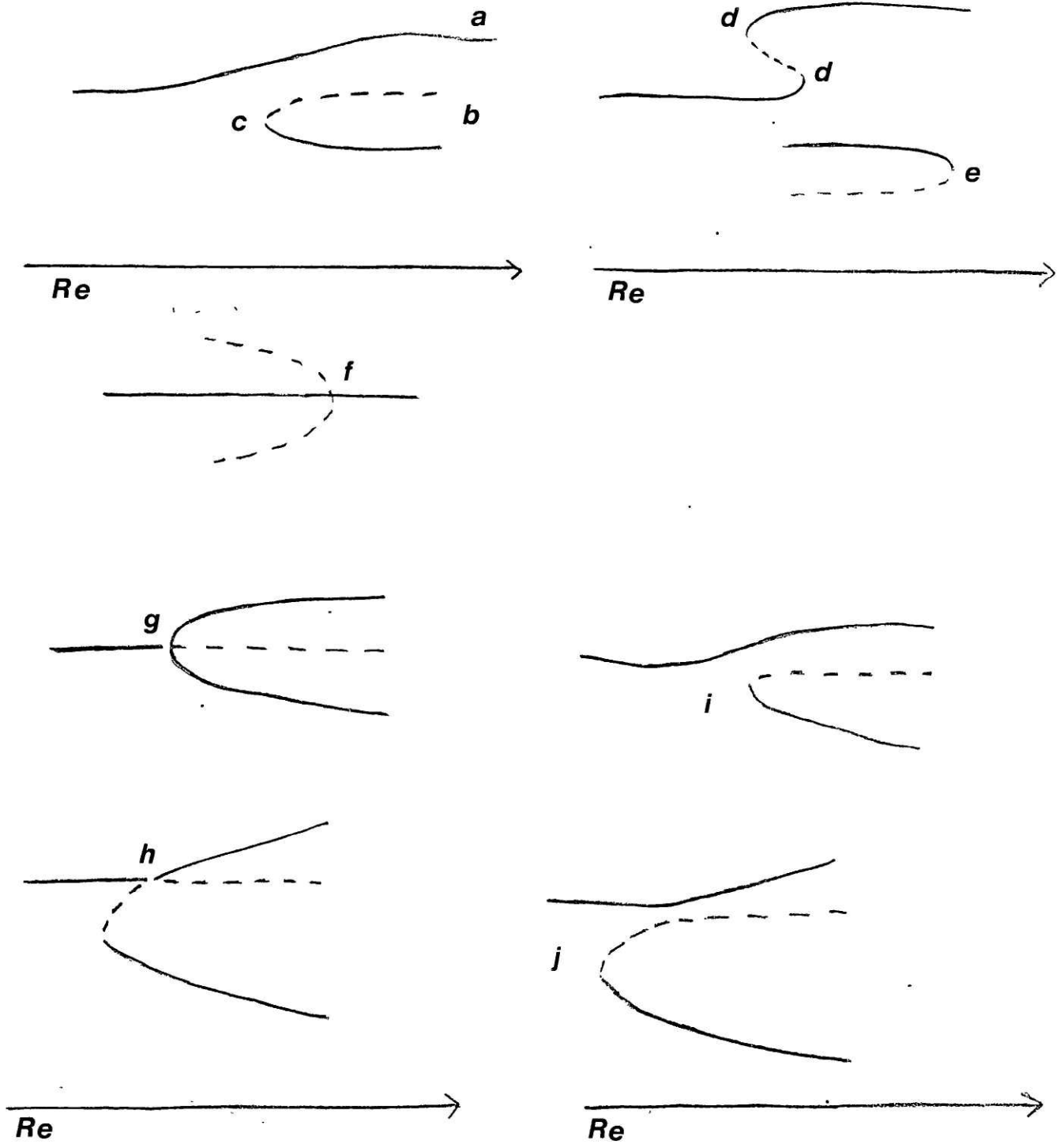


FIGURE 7.3

8. LINEAR INSTABILITY

We have found the instability that initiates transition to the one-vortex branch. The primary branch is stable to all equatorially symmetric perturbations. However, for $651 < \text{Re} < 775$, the branch is linearly unstable to an equatorially antisymmetric perturbation. After the antisymmetric perturbation grows to a threshold value, the actual transition occurs via the highly nonlinear process described in chapter 6. The final state is the (symmetric) one-vortex state. As we have seen in chapter 7, the interval $651 < \text{Re} < 775$ of the primary branch includes both zero-vortex and two-vortex states: the zero- to one-vortex transition and the two- to one-vortex transition are aspects of the same phenomenon.

8.1. Growth rates and the Window

The growth rate (in units of inverse revolution times) of the antisymmetric perturbations as a function of Re is shown as the curve in Figure 8.1. These were calculated by the procedure described in section 3.5. The exact Reynolds number at which the growth rate first exceeds zero is $\text{Re} = 652$, in agreement with Wimmer's experimental data to 3 significant digits. The growth rate then increases with Re until $\text{Re} = 735$, where it reaches its maximum value of 0.68, or equivalently an e-folding time of 1.5 revolutions. Then the growth rate sharply decreases, becoming negative at $\text{Re} = 775$. It is interesting to note that the growth rate

achieves its maximum value at approximately the same Re at which the second recirculating vortex appears (see Figure 4.3) and exactly at the Re at which the torque of the primary branch obtains its minimum value (see Figure 7.1). We conjecture that the rapid decrease in growth rate as a function of Re for $Re > 735$ is due to the stabilizing and angular momentum transporting properties of the second recirculating vortex.

We may call the interval $651 < Re < 775$ a "window" from the primary branch to the one-vortex branch. Once the one-vortex branch is attained, there is no difficulty remaining on it; if the Reynolds number is raised or lowered (to a value for which the one-vortex branch still exists, i.e. $Re \geq 645$), the flow changes smoothly to the one-vortex state corresponding to that Reynolds number. But the branch can only be reached if the time spent in the window, weighted by the growth rate at each Reynolds number, is large enough for the antisymmetric perturbation to reach the threshold level necessary for transition to occur.

This window, then, is the mathematical explanation for Wimmer's phenomenological finding. He found that the final state attained for $Re > 600$ depended strongly on the time taken for spinup of the inner sphere, but that "attention need be paid only to the acceleration in the immediate vicinity of the critical Reynolds number" (Wimmer 1976). A long spin-up time generated the one-vortex state, while a

shorter spin-up time generated the two-vortex state at the same Reynolds number.

We can calculate an approximate lower bound on the amount of time required in Wimmer's apparatus for transition to the one-vortex state to occur. We know that $R_1 = 6.8$ cm and assume the viscosity to be of order $\nu = .01$ cm²/sec. At $Re = 735$, the Reynolds number of fastest growth, the e-folding time is 1.5 revolutions, which is 1 minute. Assume an initial amplitude for perturbations that is 10^{-6} of the velocity (King, private communication). For the perturbation to grow to a level of 10^{-1} , the approximate threshold value necessary for transition, requires 15 minutes. With an initial amplitude of 10^{-2} , transition should require 3 minutes. Wimmer's (1976) data indicates that the time required in his experiment for transition to the one-vortex state is 3 to 9 minutes.

Our model predicts that the zero- and two- vortex states of the primary branch should never be the final steady state for Reynolds numbers in the window $651 < Re < 775$. If sufficient time is not allotted for transition to occur, these unstable equilibria may be mistaken for stable states. The model does not preclude the stability of zero- or two- vortex states on other possible secondary branches, which may exist, in light of Schrauf's (1983) description of the complexity of the branches.

8.2 Relation to Previous Numerical Work

The eigenvectors and eigenvalues we have found are those of the operator $Q(U)$ corresponding to the Navier-Stokes equations linearized about the steady state U :

(8.1)

$$(Q(U)) (u) \equiv - (u \cdot \nabla) U - (U \cdot \nabla) u - \nu \nabla^2 u$$

The domain of $Q(U)$ is restricted to fields u satisfying

$$\nabla \cdot u = 0 \quad (8.2)$$

and the boundary conditions

$$u = 0 \quad r = R_1, R_2 \quad (8.3)$$

It is possible to form the linear operator $Q(U)$ and find its eigenvectors and eigenvalues even if U is not a steady solution. This is equivalent to investigating the stability of the Navier-Stokes equations with an external force

$$F_{ex} \equiv (U \cdot \nabla) U - \nu \nabla^2 U \quad (8.4)$$

or, alternatively, to using U as an approximation to a steady state. We have found another set of eigenvectors and eigenvalues, which we call Stokes eigenvectors and Stokes eigenvalues, by using the Stokes solution, defined in chapter 5, as U .

The crosses on Figure 8.1 are the Stokes eigenvalues for various values of Re . We see that the Stokes eigenvalues are close to the true eigenvalues for $650 < Re < 700$.

In particular the lowest Reynolds number for which the growth rate is positive is 648 for Stokes flow, as compared with 652 for the true primary flow. Mathematically, this indicates that the eigenvalue problem depends much more strongly on Re as a parameter than via the basic flow. Physically, this result indicates that the meridional part of the basic flow does not play an important role in the onset of instability, and that the instability is the same as that which occurs in the formation of Taylor vortices in cylindrical Couette flow. Yakushin's (1969) analysis, in which he computed the eigenvalues and eigenvectors for the Stokes flow, is shown to be a good approximation to the instability that actually occurs. He cannot see the window effect; he does not allow for qualitative change of the primary flow, and the growth rate only increases with Re .

Considerations of equatorial symmetry have played an important role in previous linear stability analyses of both spherical Couette flow and finite cylinders. The operator $Q(U)$ corresponding to the Navier-Stokes equations linearized about a symmetric state U , with symmetric boundary conditions, commutes with the equatorial reflection operator

$$(R(u_r, u_\theta, u_\phi))(r, \theta, \phi) \equiv (u_r, -u_\theta, u_\phi)(r, \pi - \theta, \phi) \quad (8.5)$$

Therefore its eigenvectors have a definite parity and consideration can be restricted to eigenvectors which are either symmetric or antisymmetric. An asymmetric (of neither parity) eigenvector must be the sum of eigenvectors of

opposite parity with the same eigenvalue, so is possible only if an eigenvalue is degenerate. Yakushin found that unstable eigenfunctions occurred in pairs, each consisting of an antisymmetric and a symmetric eigenfunction whose eigenvalues intertwine as Re is varied. That is, the eigenvalues are almost degenerate. Blennerhassett and Hall (1979) found the same result for finite cylinders.

An eigenvalue - eigenvector solver is, however, insufficient for studying transition to the one-vortex branch. Using only linear stability analysis, we would know that the basic branch is unstable to an antisymmetric perturbation of the Taylor-vortex form, but not the evolution of the flow due to this instability, nor its eventual steady-state destination. This drawback is evident when we compare our results to the stability analyses of Yakushin (1969) and Munson et al. (1971,1975). They found that the eigenvectors with the lowest critical Reynolds number were antisymmetric, but believed that experimental verification would require the final states to be asymmetric.

8.3 Eigenvectors

We now show the antisymmetric eigenvectors of the operator $Q(U)$ defined by equations (8.1-8.3) for various flows U . Section 3.5 explains the method of calculation that was used. For illustrative purposes, we begin by showing the Stokes eigenvector -- the unstable eigenvector calculated by using the Stokes flow as an approximation to the

steady state -- at $Re = 700$. Figure 8.2a shows the meridional streamfunction, 8.2b the contours of constant angular velocity, and 8.2c the spectrum of the Stokes eigenvector. Like the other eigenvectors, the Stokes eigenvector has the form of a modulated stack of Taylor vortices. The meridional flow, shown in Figure 8.2a, has the form of vortices. The vortex boundaries (inflow or outflow boundaries) appear as solid radial streamlines. As explained in chapter 5, the meridional streamfunction is symmetric for an antisymmetric flow field. Fluid flows across the equator in antisymmetric velocity field, .

Flow along a Taylor vortex itself (without the addition of the primary flow on which it is to be superimposed) follows a spiral, not circular, path. There is not only meridional flow but also azimuthal flow, shown in Figure 8.2b. We emphasize that, despite its resemblance to Figure 8.2a, Figure 8.2b is of an entirely different nature. Figure 8.2b does not indicate vortices, but the magnitude of the angular velocity. The angular velocity alternates in sign (direction), and has its maximum amplitude at or near the vortex boundaries. The solid radial lines in Figure 8.2b indicate the contours of zero angular velocity of the eigenvector, which pass through or near the vortex centers. In the parts of the arc that are not shown, the vortex structure continues with the same periodicity, but becomes progressively weaker as the poles are approached.

From the spectrum of Figure 8.1c, we see that the azimuthal velocity is in fact the larger of the two components. According to the analysis of spectra in section 5.3, each of the velocity components is the product of a Gaussian or other smoothly peaked function and of a single vector spherical harmonic.

Figure 8.3 shows the primary flow at $Re = 700$, and Figure 8.4 the antisymmetric eigenvector to which it is unstable. At $Re = 700$, the primary flow is a zero-vortex state, and the instability initiates the zero- to one- vortex transition described in chapter 6 (see Figure 6.7). Figure 8.5 is the primary flow at $Re = 750$, and Figure 8.6 its unstable eigenvector. At $Re = 750$, the primary flow is a two-vortex state, and the eigenvector initiates the zero- to two- vortex transition shown in Figure 6.10. The two eigenvectors are very similar to each other. They resemble distorted versions of the Stokes eigenvector. The true eigenvectors are highly concentrated at the equator; as a result, their spectra are broad.

Note that the contours of zero angular velocity of the perturbations are not radial lines. They are close to perpendicular to the contours of constant angular momentum of the primary flow (i.e. parallel to its gradient). We show this by superimposing the contours of zero angular velocity of the eigenvectors, with the angular momentum contours of the Stokes or primary flows. Figures 8.7a - c show the

superimposed contours for the Stokes flow at $Re = 700$, the primary flow at $Re = 700$, and the primary flow at $Re = 750$, respectively.

Figure Captions -- Chapter 8

- Figure 8.1 The growth rate of the antisymmetric eigenvector to which the primary state is unstable, as a function of Reynolds number. The crosses are the growth rates of the antisymmetric eigenvector of the Stokes flow. Growth rates are in units of inverse revolution times.
- Figure 8.2 The antisymmetric eigenvector of the Stokes flow at $Re = 700$. The sector $\pi/2 \pm \pi/8$ is shown. Figures 8.2a, b, and c show the meridional streamlines, contours of constant angular velocity, and energy spectrum.
- Figure 8.3 The primary flow (a zero-vortex state) at $Re = 700$. Figures 8.3a, b, and c show the meridional streamlines, contours of constant angular velocity, and energy spectrum.
- Figure 8.4 The antisymmetric eigenvector of the primary flow at $Re = 700$. Figures 8.4a, b, and c show the meridional streamlines, contours of constant angular velocity, and energy spectrum.
- Figure 8.5 The primary flow (a two-vortex state) at $Re = 750$. Figures 8.5a, b, and c show the meridional streamlines, contours of constant angular velocity, and energy spectrum.
- Figure 8.6 The antisymmetric eigenvector of the primary flow at $Re = 750$. Figures 8.6a, b, and c show the meridional streamlines, contours of constant angular velocity, and energy spectrum.
- Figure 8.7 The contours of zero angular velocity of the antisymmetric eigenvector superimposed on the contours of constant angular momentum of the primary flow. Figures 8.7a, b, and c are the superimposed contours for the Stokes flow at $Re = 700$, the primary flow at $Re = 700$, and the primary flow at $Re = 750$, respectively.

GROWTH RATE OF ANTISYMMETRIC PERTURBATION

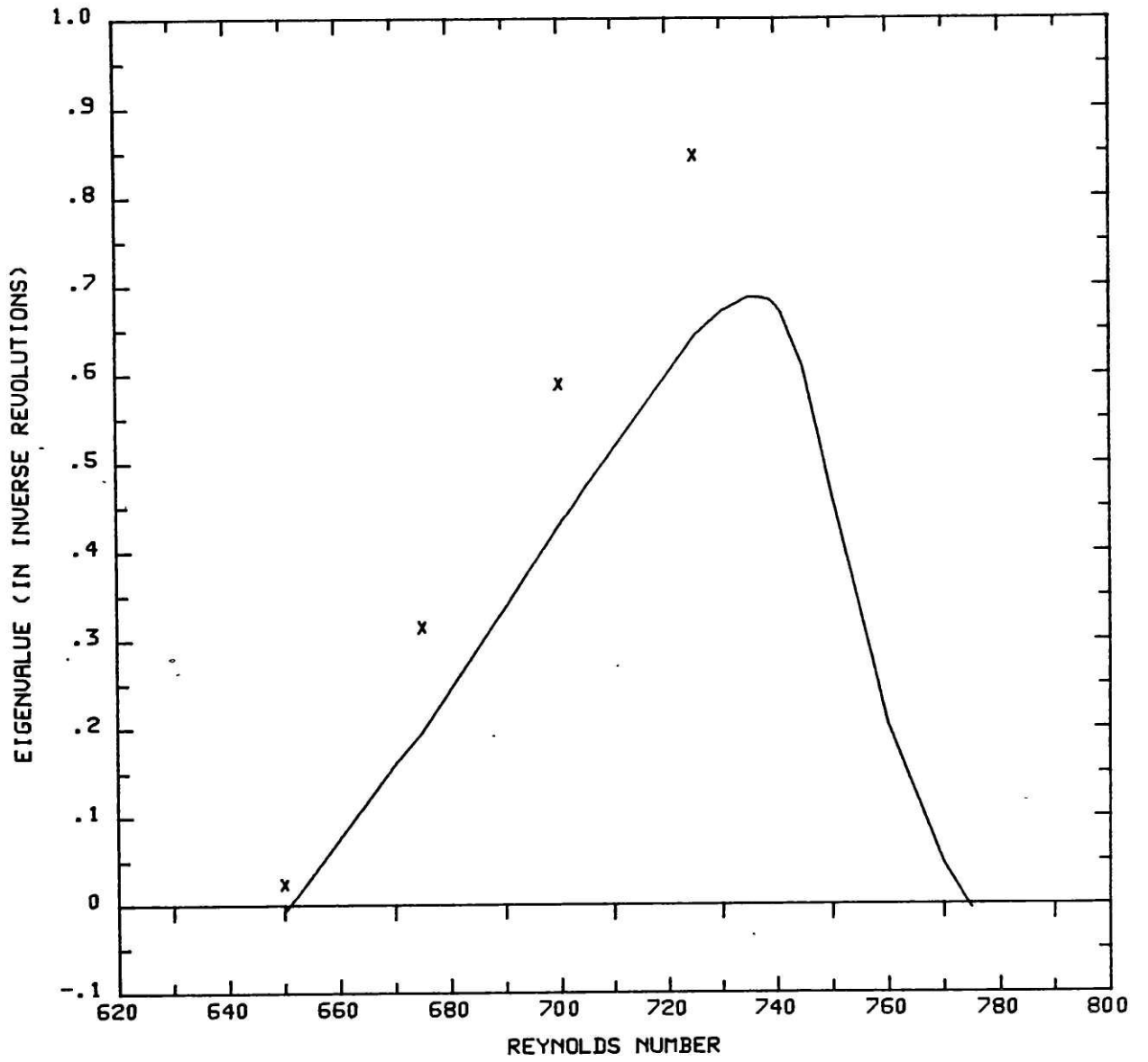


FIGURE 8.1

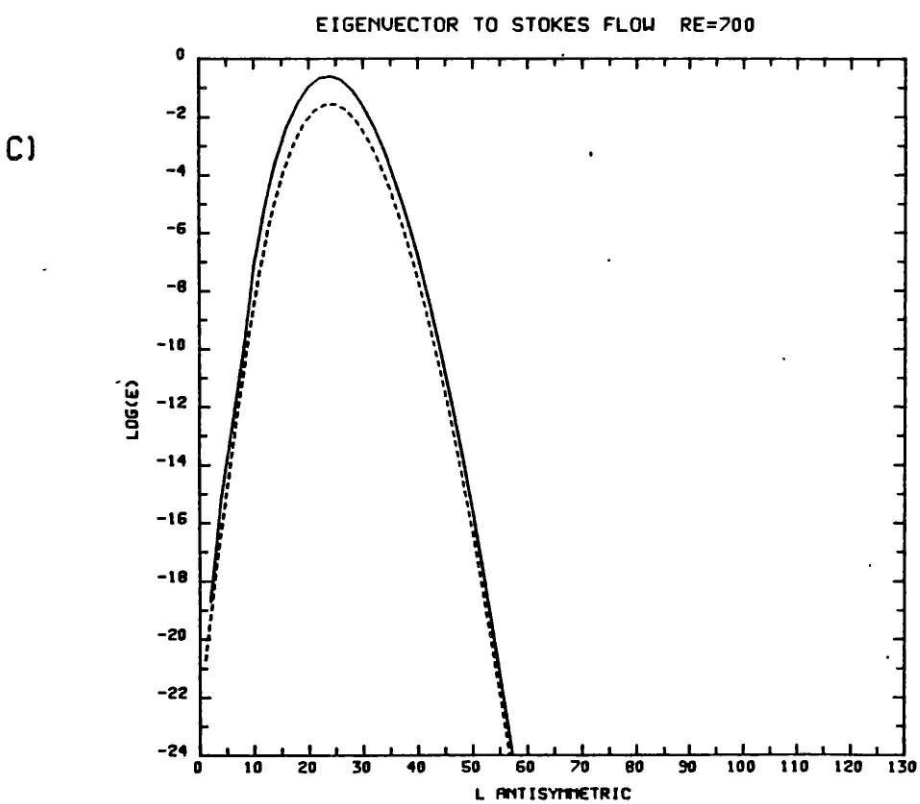
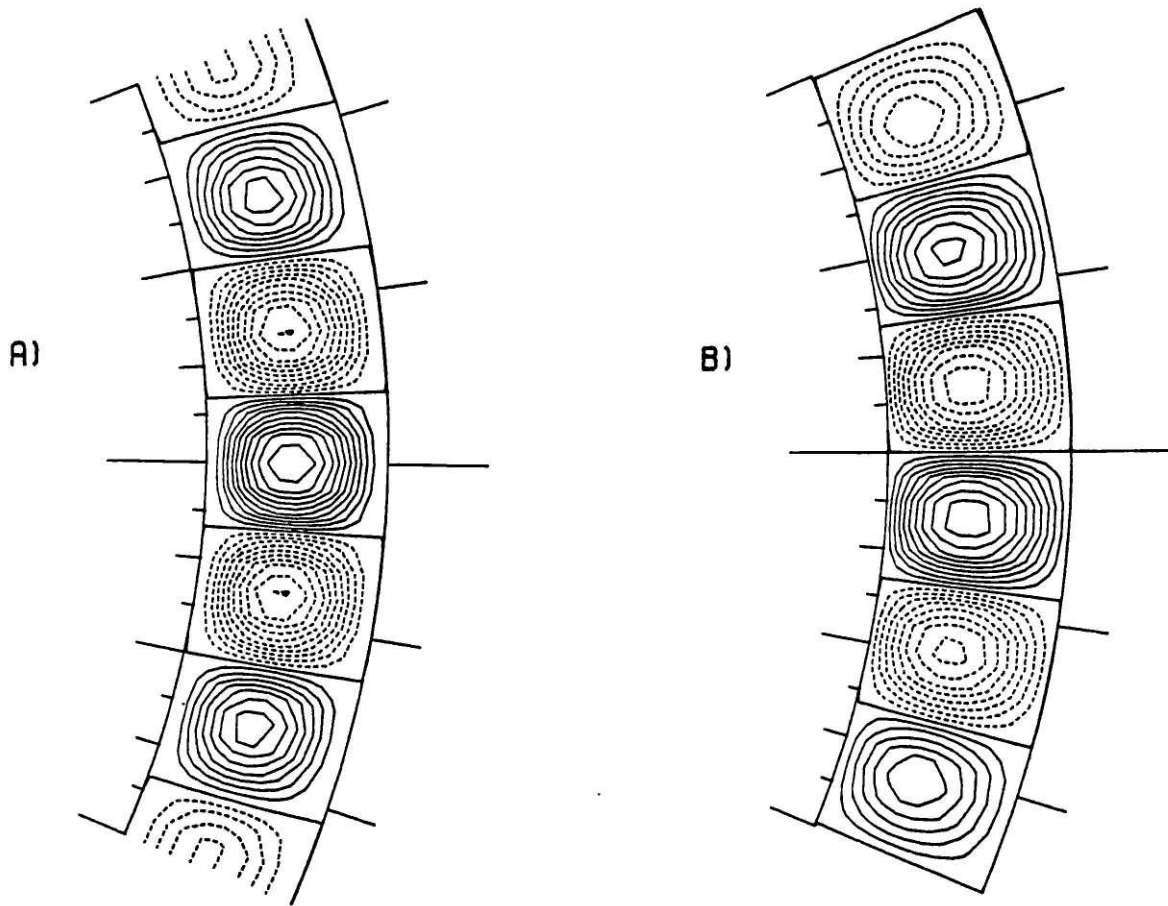


FIGURE 8.2

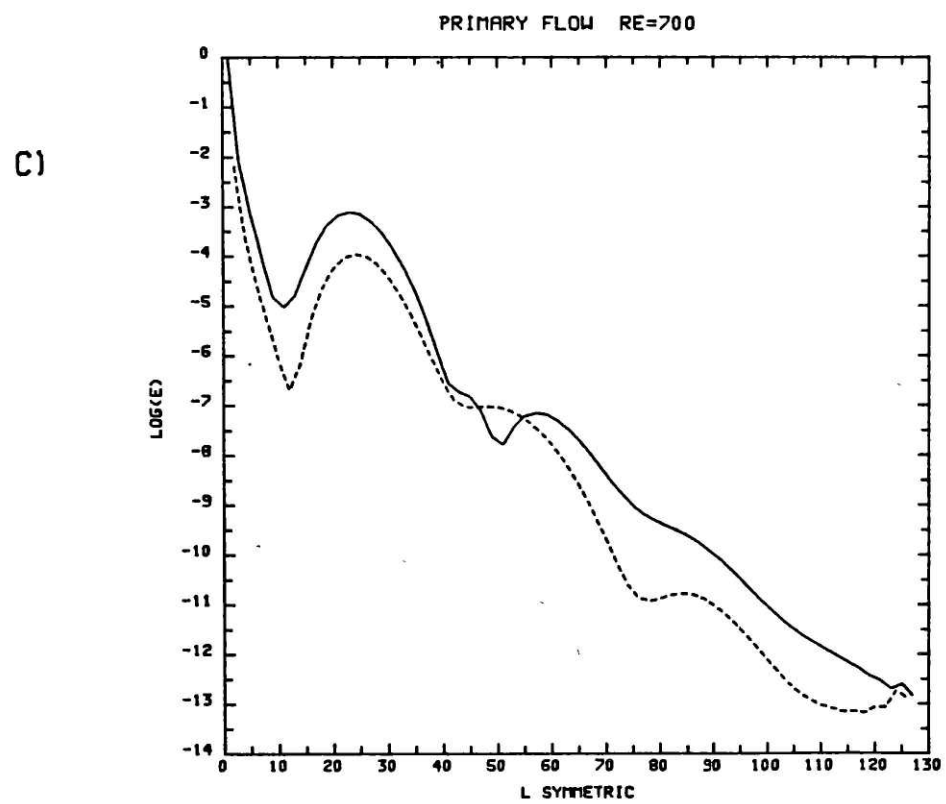
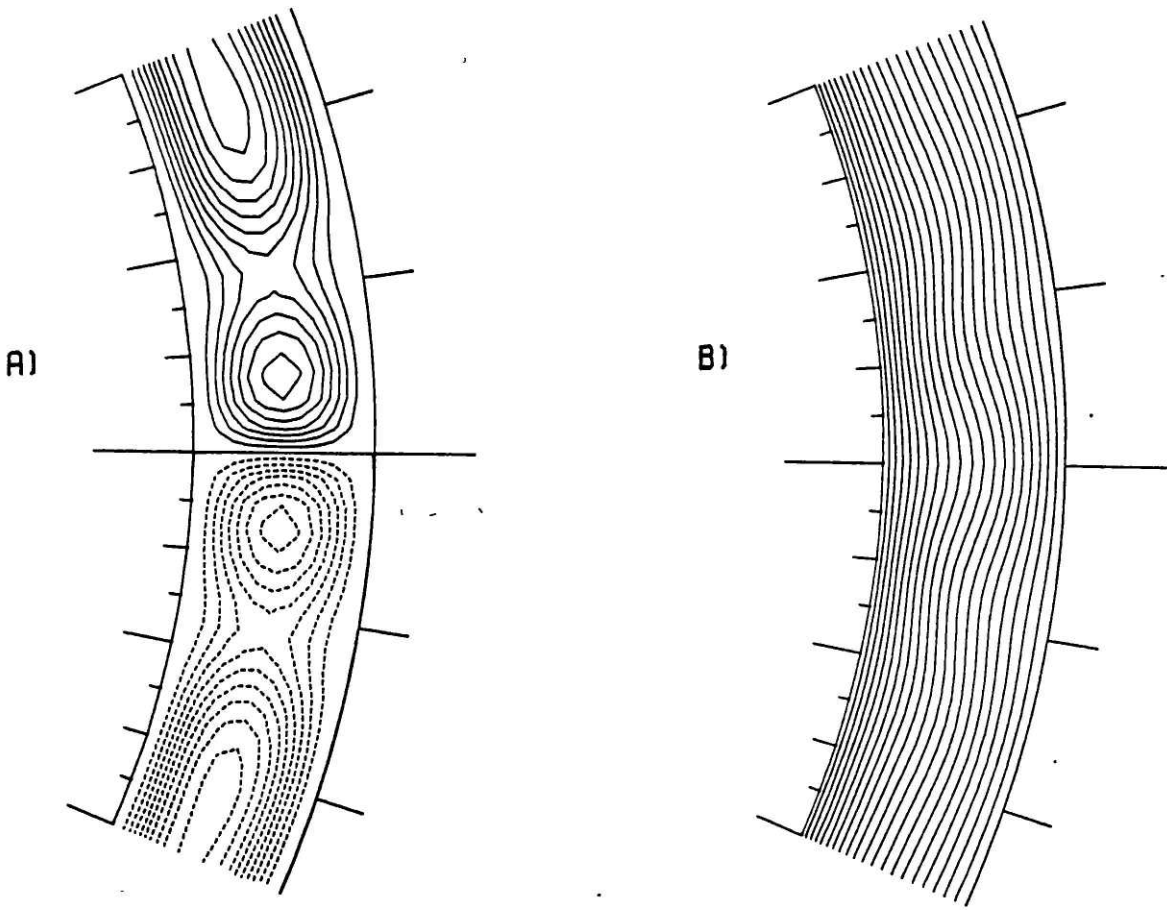


FIGURE 8.3

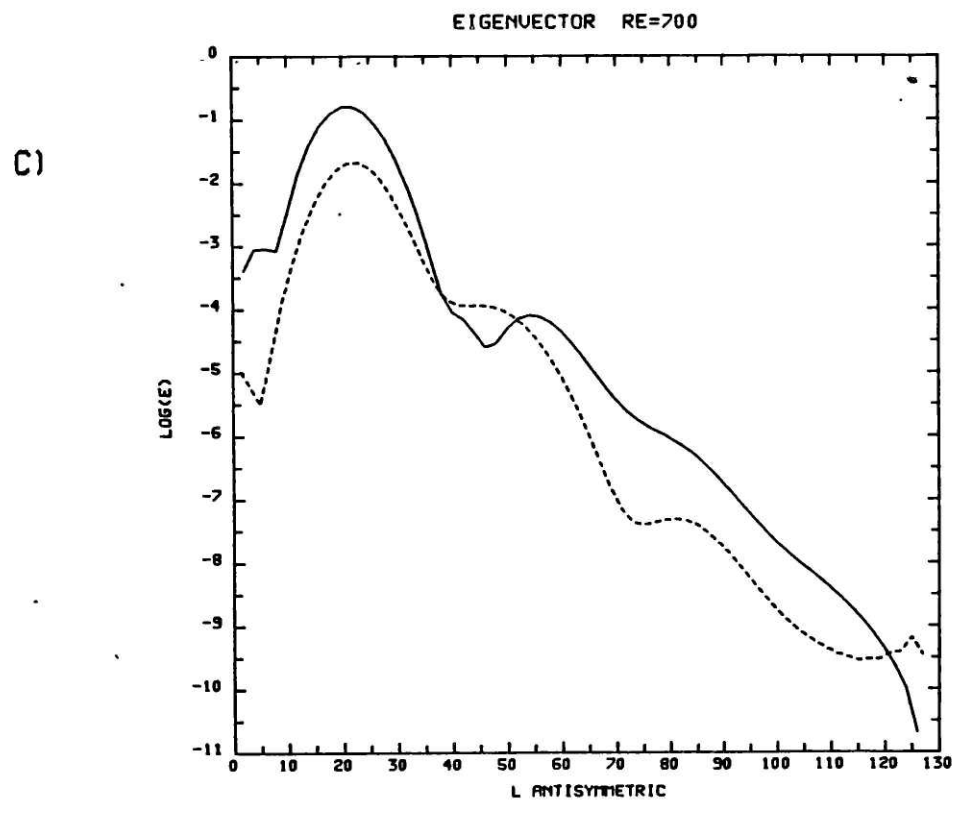
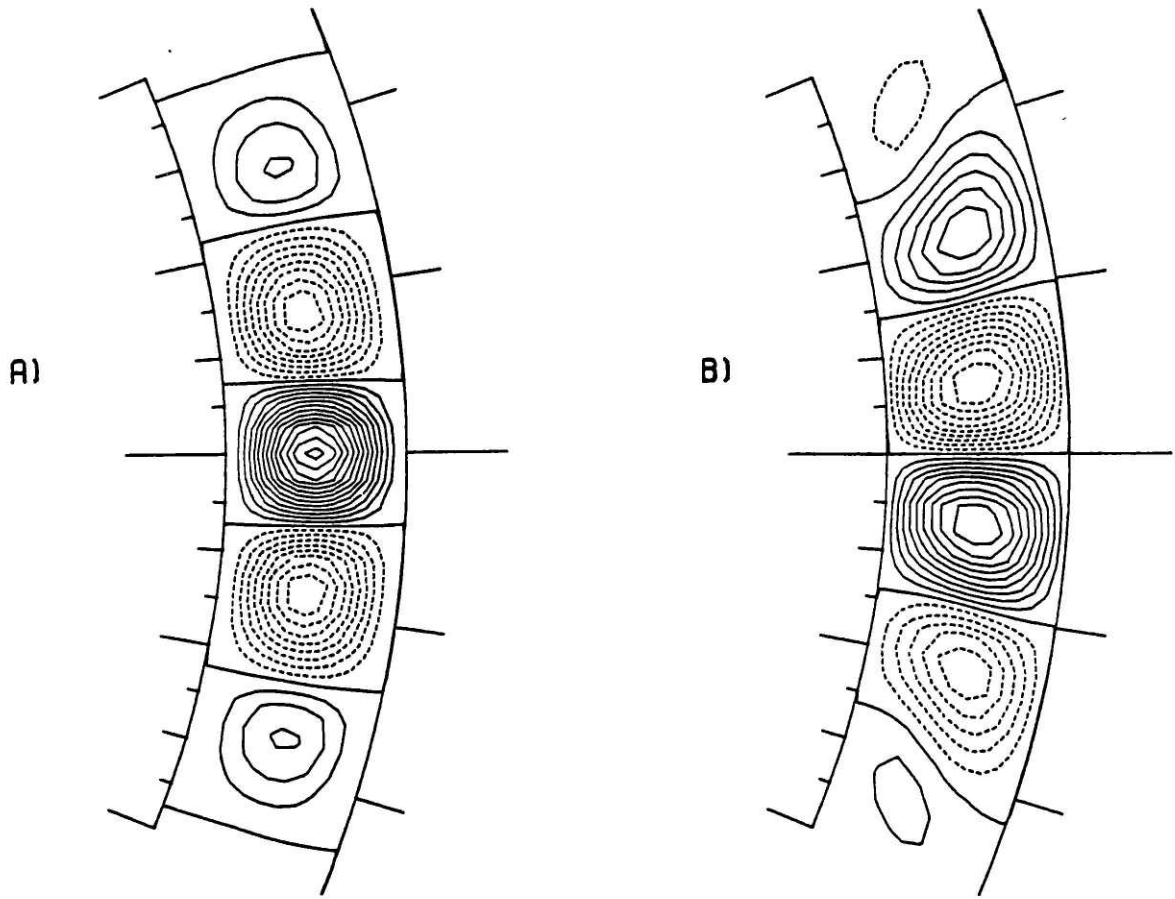


FIGURE 8.4

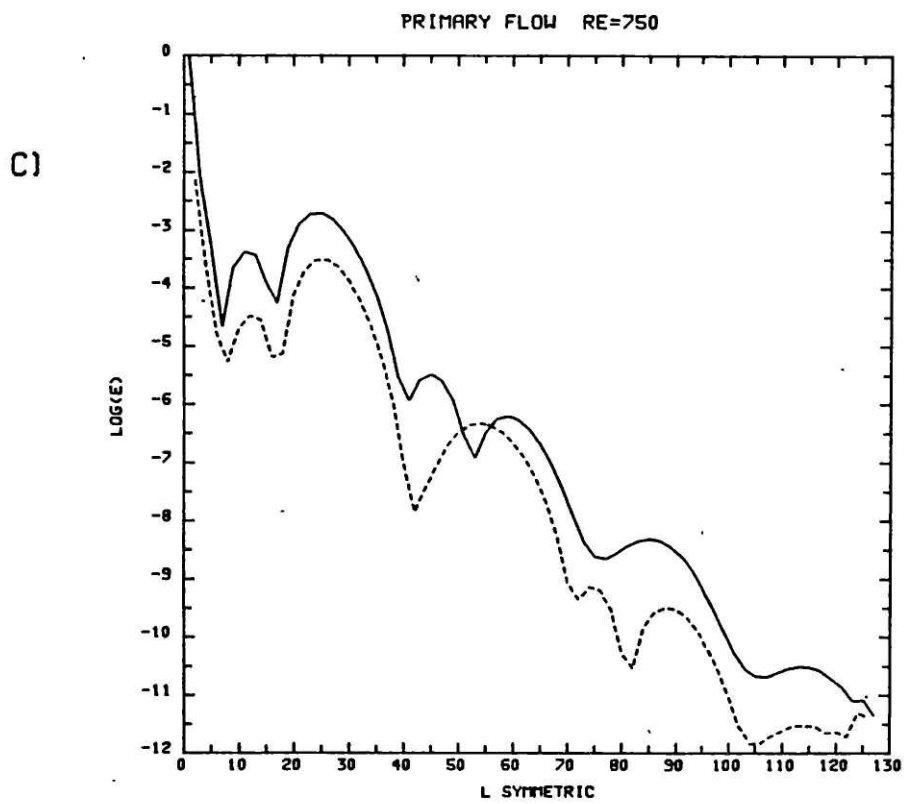
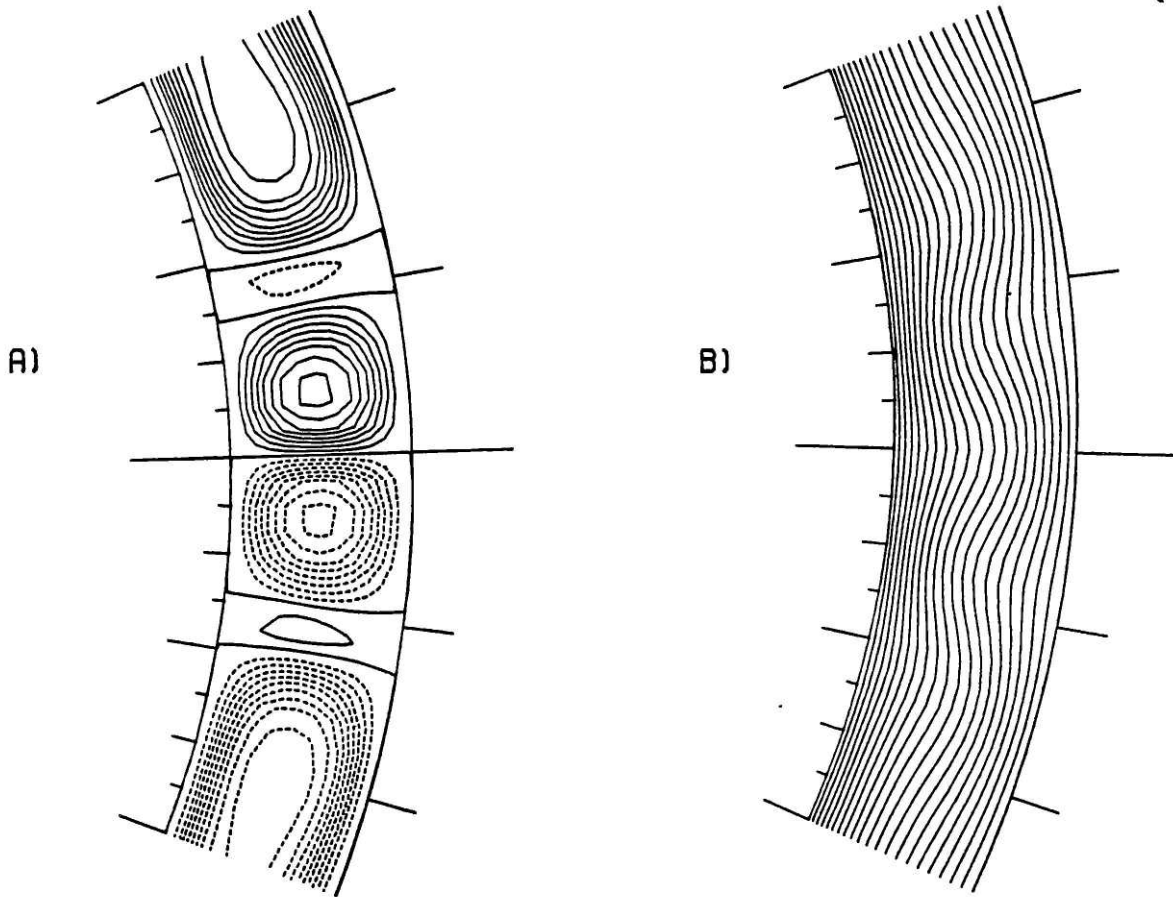
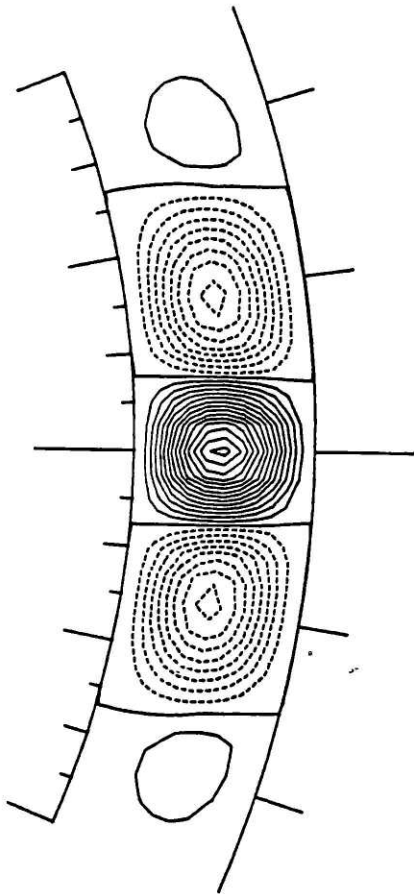
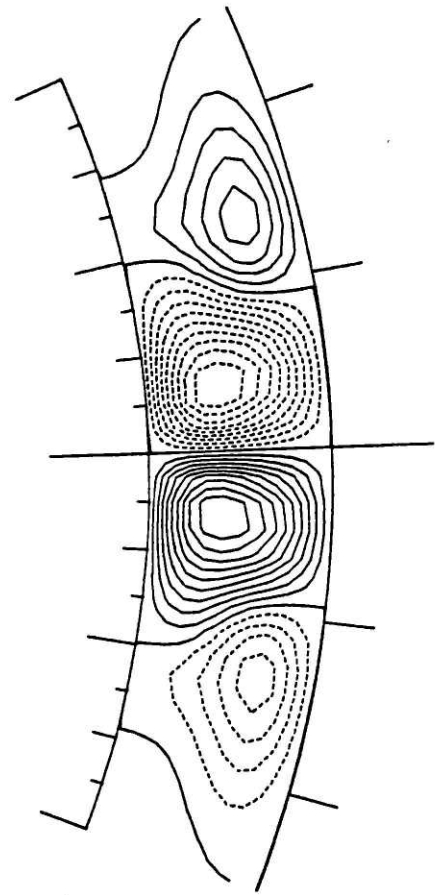


FIGURE 8.5

A)



B)



EIGENVECTOR RE=750

C)

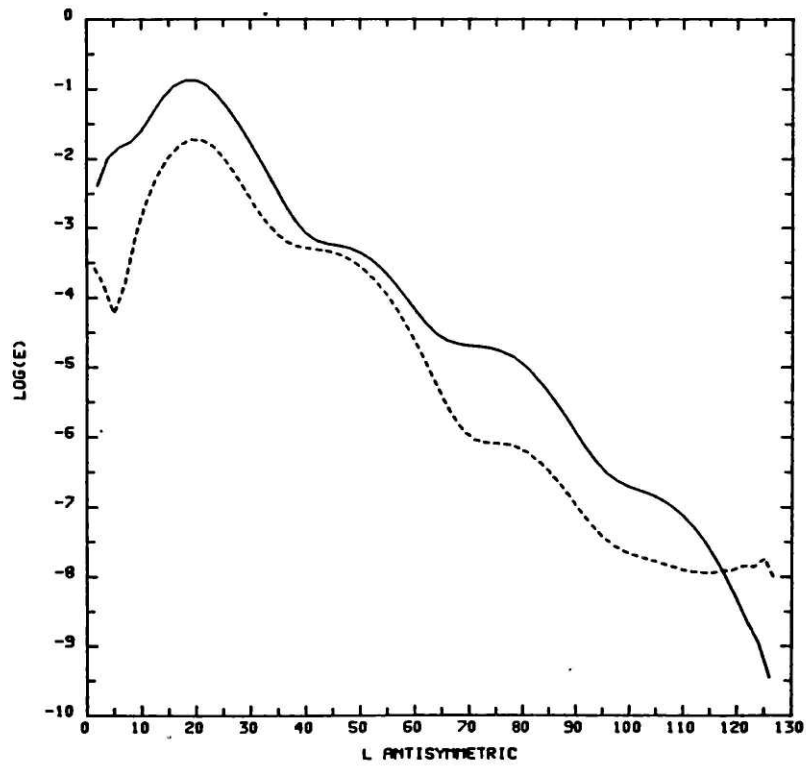


FIGURE 8.6

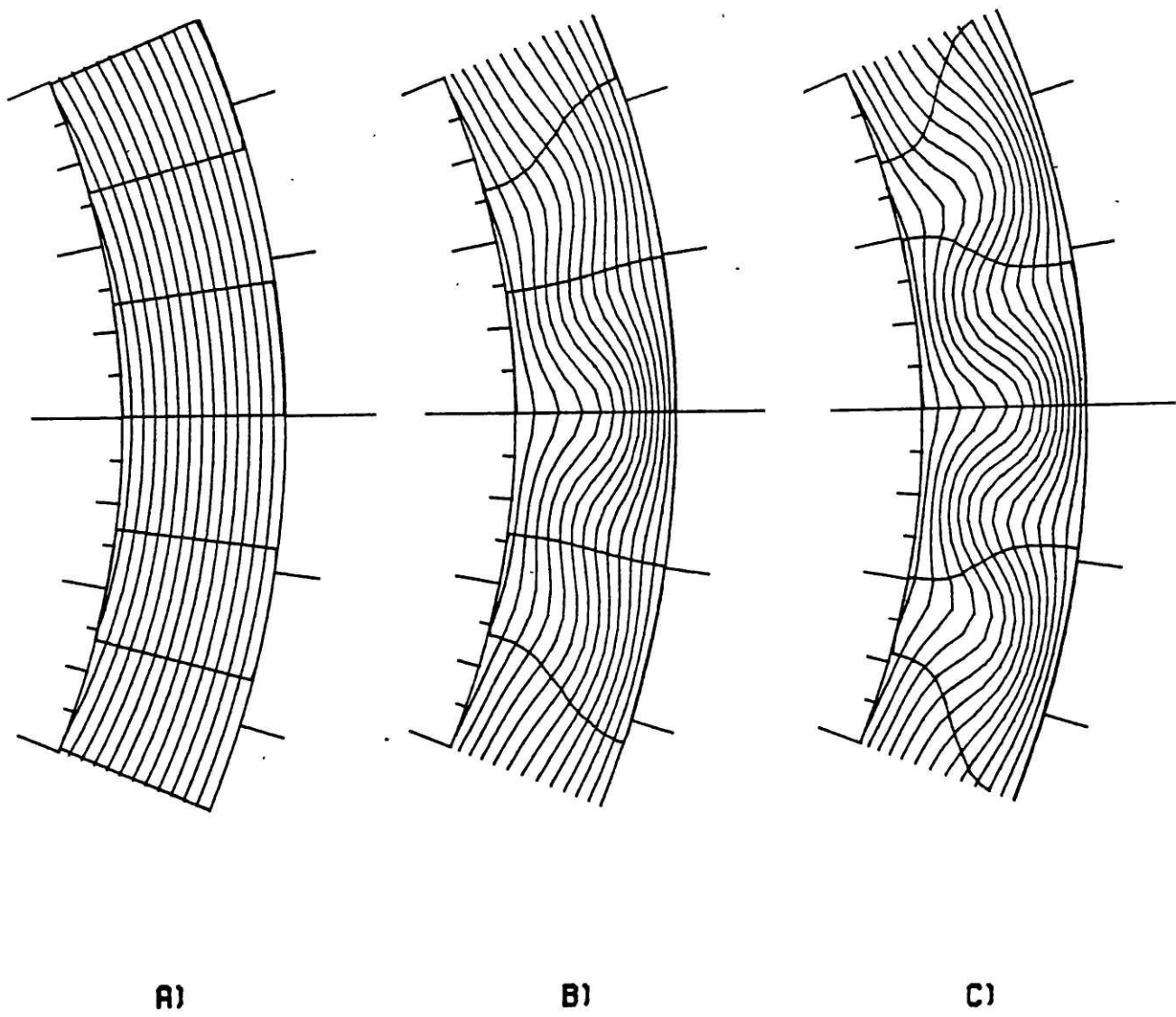


FIGURE 8.7

9. Energy Transfer

9.1 Symmetric and antisymmetric energy

In analyzing the asymmetric transitions, we are faced with the problem, mentioned in chapter 7, of wanting to project infinite dimensional flows onto a one dimensional quantity. The integrated angular momentum or torque are not appropriate for studying symmetry and antisymmetry, since only the symmetric modes contribute to the integrals. The energy, however, is ideal, since it has both a component arising from the symmetric part of the velocity field and a component arising from the antisymmetric part of the velocity field. These two component we call the symmetric energy and the antisymmetric energy. Despite its quadratic nature, the total energy is the sum of the two, since cross terms vanish upon integration.

The utility of decomposing the energy into its symmetric and antisymmetric parts is immediately seen in Figure 9.1 . Here we have shown the symmetric energy, the antisymmetric energy, and the total energy as a function of time during the zero- to one- vortex transition described in section 6.3. The scale for the symmetric and total energy, shown by the long-dashed curve and the solid curve, respectively, is given on the left axis. The antisymmetric energy is much smaller than the symmetric energy. To enable them to be shown on the same graph, a translated scale has been used for the antisymmetric energy, which is given on the

right axis. Since the two scales are translations of one another, changes in the symmetric and antisymmetric energies have the same magnitude in the graph and can be easily compared. Each of the energy curves is normalized by the Stokes flow energy, and the time is given in inner sphere revolutions.

The antisymmetric energy is initially zero, grows to a maximum value of .015, and decreases again to zero. The symmetric energy decreases sharply, then increases. Its final one-vortex state value is 0.999, less than the initial zero-vortex state value of 1.011. The total energy just decreases monotonically from 1.011 to 0.999.

To gain some understanding of this behavior, we embark on an analysis of the interaction between the symmetric and antisymmetric parts of the flow. Separating the Navier-Stokes equations into their symmetric and antisymmetric parts, we get

$$\frac{\partial \mathbf{u}_S}{\partial t} = \mathbf{u}_S \times (\nabla \times \mathbf{u}_S) + \mathbf{u}_A \times (\nabla \times \mathbf{u}_A) + \nu \nabla^2 \mathbf{u}_S - \nabla P_S \quad (9.1)$$

$$\frac{\partial \mathbf{u}_A}{\partial t} = \mathbf{u}_A \times (\nabla \times \mathbf{u}_S) + \mathbf{u}_S \times (\nabla \times \mathbf{u}_A) + \nu \nabla^2 \mathbf{u}_A - \nabla P_A \quad (9.2)$$

where \mathbf{u}_S and \mathbf{u}_A are the symmetric and antisymmetric parts of the flow, respectively, and P_S and P_A the symmetric and antisymmetric components of the pressure head.

Two features are immediately apparent:

- 1) Without the introduction of an antisymmetric perturbation, a symmetric flow remains symmetric for all time, since

the growth of the antisymmetric component is proportional to itself.

2) There can be no steady antisymmetric solution to a problem with symmetric boundary conditions, since the absence of a symmetric part renders the antisymmetric equation linear, and a linear equation with symmetric boundary conditions and forcing must have a symmetric solution. However, steady asymmetric solutions are not disqualified (and have been observed in finite cylinders by Benjamin and others).

Taking the dot products of each of (9.1) and (9.2) with their respective velocities and integrating over the entire volume, we derive

$$\frac{\partial E_S}{\partial t} = - \dot{E}_{TR} - D_S + \dot{E}_{IN} \quad (9.3)$$

$$\frac{\partial E_A}{\partial t} = \dot{E}_{TR} - D_A \quad (9.4)$$

where \dot{E}_{IN} is the (necessarily symmetric) energy input

$$\dot{E}_{IN} \equiv \frac{1}{2} \Omega_1 \tau_1 \quad (9.5)$$

(The factor of $\frac{1}{2}$ arises from the non-dimensionalization (4.1).) D_S is the symmetric dissipation

$$\begin{aligned} D_S &\equiv \dot{E}_{IN} - \frac{1}{Re} \int \mathbf{u}_S \cdot \nabla^2 \mathbf{u}_S \, dV \\ &= \frac{1}{Re} \left(\frac{16\pi}{3} + \int |\nabla \times \mathbf{u}_S|^2 \, dV \right) \end{aligned} \quad (9.6)$$

and D_A is the antisymmetric dissipation

$$D_A \equiv - \frac{1}{Re} \int \mathbf{u}_A \cdot \nabla^2 \mathbf{u}_A \, dV = \frac{1}{Re} \int |\nabla \times \mathbf{u}_A|^2 \, dV \quad (9.7)$$

The energy transfer function, defined by

$$\dot{E}_{TR} \equiv \int \mathbf{u}_A \cdot \mathbf{u}_S \times (\nabla \times \mathbf{u}_A) dV \quad (9.8)$$

measures the transfer of energy from the symmetric to the antisymmetric part of the flow. The integrand in the energy transfer function is the triple product of the antisymmetric velocity, the antisymmetric vorticity, and the symmetric velocity. Note, however, that it is only the integral of the triple product which is significant because (9.5) does not include terms that vanish upon integration over Θ . The local energy transfer function is

$$\mathbf{u}_A \cdot \mathbf{u}_S \times (\nabla \times \mathbf{u}_A) + \mathbf{u}_A \cdot \mathbf{u}_A \times (\nabla \times \mathbf{u}_S) - \nabla \cdot (\mathbf{u}_A P_A) \quad (9.9)$$

The second term vanishes if (9.9) is calculated as a function of Θ , the third vanishes if (9.9) is calculated as a function of L , the wave number in Θ .

Returning to Figure 9.1, we see that the increase in antisymmetric energy at the beginning of the transition mirrors the decrease in symmetric energy and vice versa at the end of the transition. This suggests that energy is transferred from the symmetric to the antisymmetric modes at onset of the transition and from the antisymmetric to the symmetric modes as symmetry is re-established.

If we compute the energy transfer \dot{E}_{TR} , shown in Figure 9.2, we see that the second part of this scenario is not correct. The energy transfer is always positive: energy is never transferred from the antisymmetric part of the flow to the symmetric part.

How then does the antisymmetry decrease? From equation (9.4), we see that \dot{E}_A is the difference between \dot{E}_{TR} and D_A . Throughout the transition, $\dot{E}_{TR} \approx D_A$ (the curves could not be distinguished if both were graphed). \dot{E}_A is therefore much smaller than either, with a maximum value of 0.003 (in units of Stokes energy / revolution time).

$$|\dot{E}_A| \ll \dot{E}_{TR} \approx D_A \quad (9.10)$$

At the beginning of the transition, the transfer is slightly greater than the dissipation and at the end, it is slightly less; The flows u_S and u_A have changed in such a way as to no longer favor energy transfer. This accounts for the slow re-establishment of symmetry, since the antisymmetry decreases on a viscous timescale.

9.2 Energy transfer from a purely azimuthal equilibrium

The significance of the energy transfer function is not limited to the transfer between symmetric and antisymmetric modes. Consider the decomposition of a flow into U , an equilibrium state, and u , a perturbation. The energy E of the perturbation obeys

$$\frac{\partial E}{\partial t} = \dot{E}_{TR} - D \quad (9.11)$$

where

$$E \equiv \int \frac{1}{2} \mathbf{u} \cdot \mathbf{u} \, dV \quad (9.12)$$

$$\dot{E}_{TR} \equiv \int \mathbf{u} \cdot \mathbf{U} \times (\nabla \times \mathbf{u}) \, dV \quad (9.13)$$

$$D \equiv \frac{1}{Re} \int |\nabla \times \mathbf{u}|^2 \, dV \quad (9.14)$$

Suppose that $\mathbf{U} = \mathbf{U}_\phi$ is axisymmetric and purely azimuthal, e.g. the Stokes solution in cylindrical or spherical Couette flow, and let \mathbf{u} be an axisymmetric perturbation. A meridional perturbation \mathbf{u}_m generates a vorticity which is exclusively azimuthal. Then

$$\mathbf{U}_\phi \times (\nabla \times \mathbf{u}_m) = 0 \quad (9.15)$$

so that the triple product in (9.12) is zero. The perturbation must have an azimuthal component \mathbf{u}_ϕ , which generates a meridional vorticity $\nabla \times \mathbf{u}_\phi$ for energy transfer to take place. On the other hand, the azimuthal perturbation, \mathbf{u}_ϕ is parallel to the basic flow \mathbf{U}_ϕ

$$\mathbf{u}_\phi \times \mathbf{U}_\phi = 0 \quad (9.16)$$

and will also yield a zero triple product. We see that both the meridional and azimuthal components are essential for the transfer of energy from the basic flow \mathbf{U}_ϕ to the perturbation \mathbf{u} . This reflects a general property of energy transfer to a perturbation: the perturbation must have a component perpendicular to the basic flow, and a vorticity component perpendicular to both, in order for its energy to grow. Its linear growth rate is proportional to the integral of the triple product.

In spherical Couette flow, this analysis is not exact, since the basic flow \mathbf{U} has a meridional component but in fact, the meridional component \mathbf{U}_m is very small and its contribution to the energy transfer function negligible relative to that of \mathbf{U}_ϕ .

Figure Captions -- Chapter 9

Figure 9.1 Energy as a function of time during the zero- to one- vortex transition. The axis on the left is the scale for the total energy and the energy of the symmetric part of the flow, which are shown by the solid and long-dashed curves, respectively. The axis on the right is the (translated) scale for the energy of the antisymmetric part of the flow, shown by the short-dashed curve. Energies are non-dimensionalized by the Stokes energy.

Figure 9.2 The energy transfer rate from the symmetric to the antisymmetric components of the flow as a function of time during the zero- to one- vortex transition. The transfer function is non-dimensionalized by (Stokes energy / Revolution period).

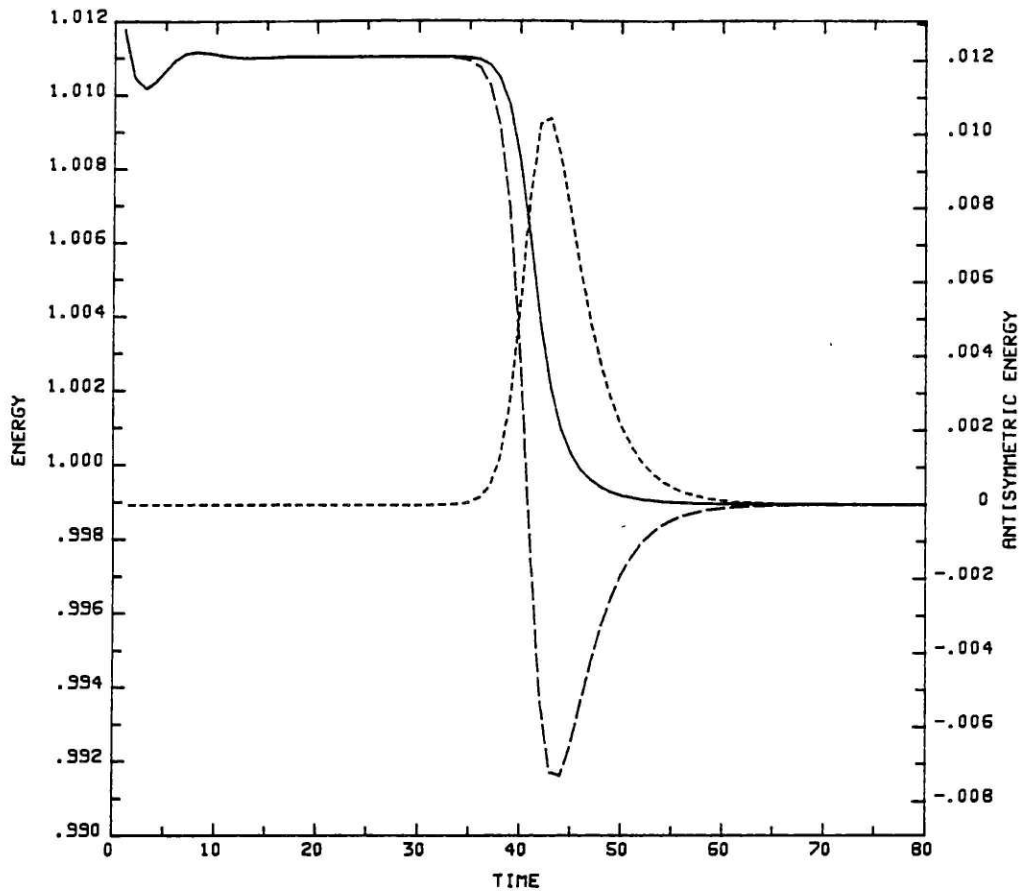


FIGURE 9.1

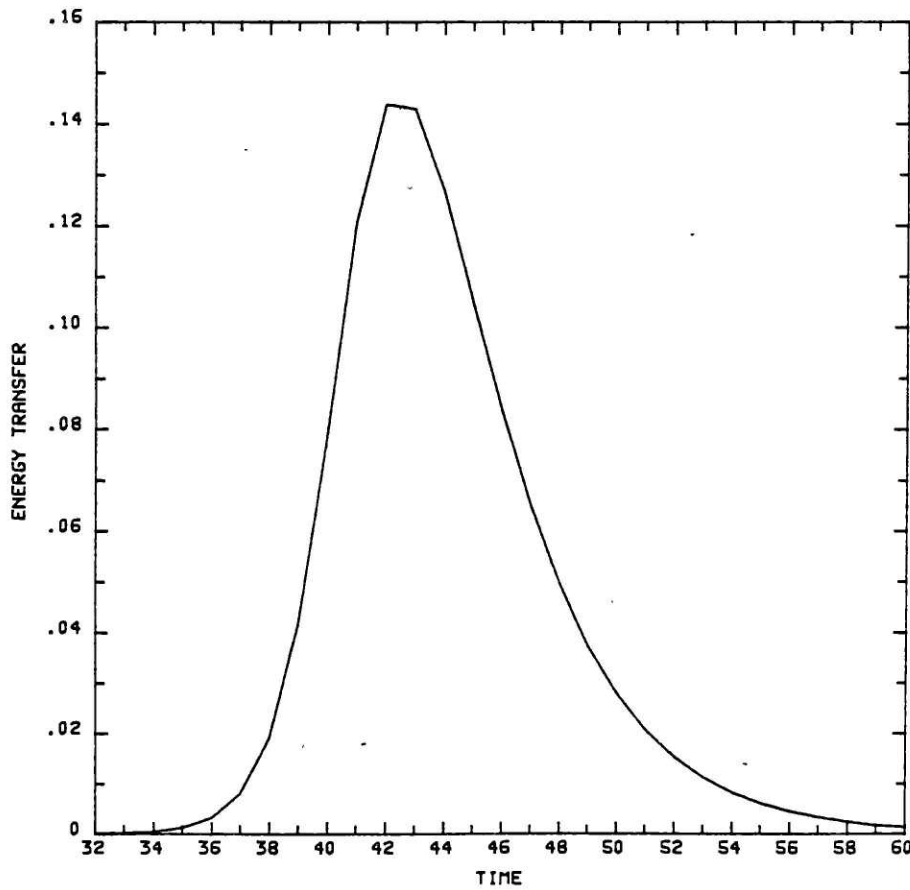


FIGURE 9.2

10. CONCLUSION

In this chapter, we summarize the results of the thesis. At the same time, we raise a number of unanswered questions that follow from our results.

In Part I, we introduced the problem of Taylor vortex formation in spherical Couette flow. We described our spectral, axisymmetric initial value code. Its results were shown to be consistent, in good agreement with experiment, and sufficiently resolved. Using the code, we have calculated the flows presented in Part II. By waiting until convergence, as was done in other initial value studies, we generated the steady states of spherical Couette flow. But, more importantly, we have described the variety of transitions that occur in the range $644 < Re < 800$. Because they had not previously been simulated numerically, the equatorially asymmetric transitions -- the zero- to one- and two- to one- vortex transitions -- are particularly interesting.

There is no doubt that transitions to the one-vortex state are asymmetric. Buhler (private communication) informed us that he had observed the same time evolution experimentally : "in one hemisphere two vortices occur and the deformation in the other hemisphere disappears. Gradually the two vortices move into the equatorial region. This transition is not symmetric with respect to the equator, only the final state".

The question naturally arises, why should the transition be asymmetric? A partial answer is provided by the observation that inflow and outflow boundaries differ in fundamental ways. (This was briefly alluded to in chapter 6.) The experimental results of Mullin (1982) on formation of Taylor vortices in cylinders suggest a transition similar to the one we have found in spheres. Cylinders, too, tend to have an even number of Taylor vortices, with inflow boundaries at the top and bottom (but not always).

Mullin observed visually that transitions from an odd number of pairs of vortices (i.e. 6 vortices) to an even number of pairs (i.e. 8 vortices) took place asymmetrically. Had the transition taken place symmetrically, it would have required the insertion of a pair of vortices at the equator, an outflow boundary. He suggests that it is because vortex pairs are strongly linked at outflow boundaries that these transitions take place asymmetrically.

Marcus's (1983) numerical work on non-axisymmetric cylindrical Couette flow also attests to the difference between inflow and outflow boundaries. The outflow jet is always stronger than the inflow jet and the separation between the vortices much greater at the inflow boundary than at the outflow boundary. Marcus has shown that traveling azimuthal waves result from an instability of the outflow jet.

The pinches are still rather mysterious objects. We

have defined pinches, and determined the Reynolds number at which they first occur, but do not have a detailed understanding of them. It is clear that their reason for existence is the same as that of Taylor vortices: they redistribute angular momentum between radial shells near the equator. In a pinch, however, streamlines near the walls approach the stagnation point (of the meridional flow), then reverse their radial direction and return to the walls. What is the restoring force that causes the fluid elements to reverse their radial direction? That is, what determines that a pinch will form at a given Re rather than a Taylor vortex?

What is the role of pinches in the transition process? In the transitions from the zero-vortex state to either of the one- or two- vortex states, we have seen that pinches act as precursors of Taylor vortices. In dividing from a basic vortex, a pinch leaves stagnant regions near the walls that function like wedges, in which recirculation vortices arise and join. After the formation of recirculation vortices the original pinches become Taylor vortices. Yet, the zero- to one- vortex transition resembles that which occurs in cylindrical Couette flow between infinite cylinders: the Taylor numbers are close, the eigenvectors very similar. There are no pinches in cylindrical Couette flow, suggesting that the role of the pinches cannot be as central as it appears visually in spherical Couette flow.

We turn now to Part III. We have shown the variation of the torque of the steady flow states with Reynolds number, and in so doing, the structure of the solution branches. The steady zero-vortex states evolve continuously into steady two-vortex states as the Reynolds number is increased, while the one-vortex states lie on an unconnected secondary branch. These results agree well with Schrauf's (1983) extensive steady-state survey. Further comparison of his results with those of initial value codes would be desirable. Many of the branches he has discovered are unexplored by experiment or initial value codes -- it is not known what flow history, if any, will produce them. The bifurcation diagram seems to derive, by bifurcation decoupling and continuous distortion of the branches, from a simpler one. It would be interesting to find homotopy parameters that map the diagram into a simpler one -- finally, perhaps, into the simple supercritical bifurcation of idealized cylindrical Couette flow. Schrauf has already made progress in this area by finding bifurcation diagrams for different gap sizes σ .

In chapter 8, we have seen how an interval -- the "window" of the zero- and two- vortex branch (the primary branch) is unstable to an equatorially antisymmetric perturbation. We have calculated this antisymmetric eigenvector and its eigenvalue as a function of Reynolds number, and seen how the eigenvalue decreases and finally becomes negative as the two-vortex state becomes well established. What

remains to be understood is the relation between the primary flows and the eigenvalues and eigenfunctions. The maximum growth rate occurs at $Re = 735$, at which the torque is a minimum, and near $Re = 740$ at which two-vortex states first appear. Why do the maximum growth rate and minimum torque occur at $Re = 735$ rather than $Re = 740$? It seems clear that the formation of the two-vortex state along the primary branch must be responsible for the decrease of the growth rate of the antisymmetric instability. It would be interesting to prove this and to find the mechanism responsible for the stabilization of the primary branch.

Other questions are raised in chapter 9. Do there exist steady asymmetric states? Why does the antisymmetry die out in the transitions to the one-vortex state? We have seen in chapter 9, that the energy transferred from the symmetric part of the flow to the antisymmetric part of the flow decreases as the transition progresses. Clearly, this must be due to a change in the flow, particularly the symmetric part of the flow, as it changes from a zero-vortex state to a one-vortex state. Again, the mechanism for this remains unknown.

In studying the evolution in time of the transition to the one-vortex state, we have utilized the full power of a nonlinear initial value code. With a steady-state solver, though we would know of the existence of the one vortex branch, we would not know if and when (for what values of

Re) transition to it occurred, nor how. With an eigenvalue - eigenvector solver, we would find the instability of the primary branch to an antisymmetric eigenvector, but not the time development of the transition initiated by this instability, nor that its final destination is the one-vortex state. It is the combination of time-dependent calculations with complementary steady-state and linear results that has enabled us to obtain a good understanding of the transitions in spherical Couette flow.

REFERENCES

Astaf'eva, N.M., Vvedenskaya, N.D., and Yavorskaya, I.M. 1978 Numerical study of nonlinear axisymmetric flow of fluid between two concentric rotating spheres. In Cabannes, H., Holt, M., and Rusanov, V. (ed.), Lecture notes in physics 90, Sixth Int'l Conf. on Num. Methods in Fluid Dyn., p. 56-63 Springer, Berlin.

Bartels, F. 1982 Taylor Vortices between two concentric rotating spheres. J. Fluid Mech. 119, 1-25.

Belyaev, Y.N., Monakhov, A.A., Yavorskaya, I.M. 1978 Stability of spherical Couette flow in thick layers when the inner sphere revolves. Fluid Dynamics 2, 162-168.

Benjamin, T.B. 1976 Applications of Leray-Schrauder degree theory to problems of hydrodynamic stability. Math. Proc. Camb. Phil. Soc. 79, 373-392.

Benjamin, T.B. 1978a Bifurcation phenomena in steady flows of a viscous fluid I. Theory. Proc. Roy. Soc. London A 359, 1-26.

Benjamin, T.B. 1978b Bifurcation phenomena in steady flows of a viscous fluid II. Experiments. Proc. Roy. Soc. London A 359, 27-43.

Benjamin, T.B. and Mullin, T. 1981 Anomalous modes in the Taylor experiment Proc. Roy. Soc. London A 377, 221-249.

Benjamin, T.B. and Mullin, T. 1982 Notes on the multiplicity of flows in the Taylor experiment. J. Fluid Mech. 121, 219-230.

Blennerhassett, P.J. and Hall, P. 1979 Centrifugal instabilities of circumferential flows in finite cylinders: linear theory. Proc. Roy. Soc. London A. 365, 191-207.

Bonnet, J.P. and Alziary de Roquefort, T. 1976 Ecoulement entre deux spheres concentriques en rotation. J. de Mecanique 15, 373-397.

Bratukhin, I.K. 1961 On the evaluation of the critical Reynolds number for the flow between two rotating surfaces. J. Appl. Math. Mech. 25, 1286-1299.

Buhler, K. private communication.

Burkhalter, J.E. and Koschmieder, E.L. 1974 Steady supercritical Taylor vortices after sudden starts. Phys. Fluids 17, 1929-1935.

Coles, D. 1965 Transition in circular Couette flow. *J. Fluid Mech.* 21, 385-425.

Dahlquist, G. and Bjorck, A. 1974 *Numerical Methods*. Prentice-Hall, Englewood Cliffs, N.J.

DiPrima, R.C. and Swinney, H.L. 1981 Instabilities and Transition in Flow Between Concentric Rotating Cylinders. In Swinney, H.L. and Gollub, J.P. (ed.), *Hydrodynamic Instabilities and the Transition to Turbulence*, p. 139-180. Springer, Berlin.

Edmonds, A.R. 1960 *Angular Momentum in Quantum Mechanics*. Princeton University Press, Princeton.

Gottlieb, D. and Orszag, S.A. 1977 *Numerical Analysis of Spectral Methods: Theory and Applications*. SIAM Press, Philadelphia.

Haidvogel, D.B. and Zang, T. 1979 Accurate solutions of Poisson's equation by expansion in Chebyshev polynomials. *J. Comp. Phys.* 30, 167-180.

Howarth, L. 1954 Note on the boundary layer on a rotating sphere. *Phil. Mag.* 42, 1308.

Joseph, D.D. 1981 *Hydrodynamic Stability and Bifurcation*. In Swinney, H.L. and Gollub, J.P. (ed.), *Hydrodynamic Instabilities and the Transition to Turbulence*, p. 27-76. Springer, Berlin.

Khlebutin, G.N. 1968 Stability of fluid motion between a rotating and a stationary concentric sphere. *Fluid Dynamics* 3 (6), 31-32.

King, G. private communication.

Kirchgassner, K. and Sorger, P. 1968 *Stability Analysis of Branching Solutions of the Navier-Stokes Equations*.

Kogelman, S. and DiPrima, R.C. 1970 Stability of spatially periodic supercritical flows in hydrodynamics. *Phys. Fluids* 13, 1-11.

Koschmieder, L. private communication.

Krause, E. and Bartels, F. 1980 *Finite-Difference Solutions of the Navier-Stokes Equations for Axially Symmetric Flows in Spherical Gaps*. In Dold, E. and Eckman, B. (ed.), *Approx. methods for Navier-Stokes problems*. Proc. Symp. IUTAM at Paderborn, p. 313-322. Springer, Berlin.

Lanczos, C. 1956 *Applied Analysis*. Prentice-Hall, Englewood Cliffs, N.J.

Marcus, P. 1983 Simulation of Taylor-Couette flow -- Numerical results for wavy-vortex flow with one travelling wave, to be published.

Morse, P.M. and Feshbach, H. 1953 Methods of Theoretical Physics. McGraw-Hill, New York.

Mullin, T. 1982 Mutations of steady cellular flows in the Taylor experiment J. Fluid Mech. 121, 207-218.

Munson, B.R. and Joseph, D.D. 1971a Viscous incompressible flow between concentric rotating spheres. Part 1. Basic flow. J. Fluid Mech. 49, 289-303.

Munson, B.R. and Joseph, D.D. 1971b Viscous incompressible flow between concentric rotating spheres. Part 2. Hydrodynamic stability. J. Fluid Mech. 49, 305-318.

Munson, B.R. and Menguturk, M. 1975 Viscous incompressible flow between concentric rotating spheres. Part 3. Linear stability and Experiments. J. Fluid Mech. 69, 705-719.

Rayleigh, Lord 1916 On the dynamics of revolving fluids. Proc. Roy. Soc. London A 93, 148-154.

Roesner, K.G. 1977 Numerical calculation of hydrodynamic stability problems with time-dependent boundary conditions. In Cabannes, H., Holt, M., and Rusanov, V. (ed.), Lecture notes in physics 90, Sixth Int'l Conf. on Num. Methods in Fluid Dyn., p. 1-25. Springer, Berlin.

Rosenhead, L. 1963 Laminar Boundary Layers. Oxford University Press.

Sattinger, D.H. 1973 Topics in Stability and Bifurcation Theory. Springer, Berlin.

Sawatzki, O. and Zierep, J. 1970 Das Stromfeld im Spalt zwischen zwei konzentrischen Kugelflachen, von denen die innere rotiert. Acta Mechanica 9, 13-35.

Schrauf, G. 1983 Losungen der Navier-Stokes Gleichungen fur stationare Stromungen im Kugelspalt. Ph.D Thesis, Universitat Bonn.

Schrauf, G. private communication.

Serrin, J. 1959 On the stability of viscous fluid motions. Arch. Ration. Mech. Anal. 3, 1.

Snyder, H.A. 1969 Wave-number selection at finite amplitude in rotating Couette flow. J. Fluid Mech. 35, 273-298.

Sorokin, M.P., Khlebutin, G.N., and Shaidurov, G.F. 1966 Study of the motion of a liquid between two rotating spherical surfaces. J. of Applied Mechanics and Technical Physics 7 (6), 83-84.

Sorokin, V.S. 1961 Nonlinear phenomena in closed flows near critical Reynolds numbers. J. Appl. Math. Mech. 25, 366-381.

Soward, A.M. and Jones, C.A. 1983 The linear stability of the flow in the narrow gap between two concentric rotating spheres. Q. Jl. Appl. Math. 36, 19.

Taneda, S. 1979 Visualization of separating Stokes flows. J. Phys. Soc. of Japan 46, 1935-1942.

Taylor, G.I. 1923 Stability of a viscous liquid contained between two rotating cylinders. Phil. Trans. Roy. Soc. London A 223, 289-343.

Walton, I.C. 1978 The linear stability of the flow in a narrow spherical annulus. J. Fluid Mech. 86, 673-693.

Wimmer, M. 1976 Experiments on a viscous fluid flow between concentric rotating spheres. J. Fluid Mech. 78, 317-335.

Wimmer, M. private communication.

Yakushin, V.I. 1969 Instability of fluid motion in a thin spherical layer. Fluid Dynamics 4 (1), 83-84.

Yavorskaya, I.M. 1975 Effect of latitudinal temperature gradient on spherical Couette flow. Fluid Dynamics 2, 200-206.

Yavorskaya, I.M., Astaf'eva, N.M., and Vvedenskaya, N.D. 1978 Stability and nonuniqueness of liquid flow in rotating spherical layers. Sov. Phys. Dokl. 23 (7), 461-463.

Yavorskaya, I.M., Belyaev, Y.N., Monakhov, A.A. 1975 Experimental study of a spherical Couette flow. Sov. Phys. Dokl. 20 (4), 256-258.

Yavorskaya, I.M., Belyaev, Y.N., Monakhov, A.A. 1977 Stability investigation and secondary flows in rotating spherical layers at arbitrary Rossby numbers. Sov. Phys. Dokl. 22 (12), 717-719.

Zierep, J. and Sawatzki, O. 1970 Three dimensional instabilities and vortices between two rotating spheres. In 8th Symp. Naval Hydrodyn., 275-288.

Zierep, J. private communication.